Energy Efficient Electrochemical System for Combined Carbon Dioxide Reduction and HMF Oxidation

Roger Lin
Department of Chemical Engineering
McGill University, Montreal
April 2022

A thesis submitted to McGill University in partial fulfillment of the requirements of the degree of Master of Engineering

Table of Content

List of Figures

List of Abbreviations

AA	Acetic acid
AEM	Anion exchange membrane
CA	Chronoamperometry
CO_2RR	Carbon dioxide reduction reaction
CP	Chronopotentiometry
CV	Cyclic voltammetry
EIS	Electrochemical impedance spectroscopy
DFF	2,5-Diformylfuran
EDX	Energy dispersive X-ray
EtOH	Ethanol
EXAFS	Extended X-ray adsorption fine structure
FA	Formic acid
FDCA	2,5-Furandicarboxylic acid
FE	Faradaic efficiency
FFCA	5-Formyl-2-furancarboxylic acid
FTIR	Fourier-transform infrared
GC	Gas chromatography
HAADF	High-angle annular dark-field
HER	Hydrogen evolution reaction
HMFOR	5-hydroxymethylfurfural oxidation reaction
HPLC	High-performance liquid chromatography
ICP-OES	Inductively coupled plasma – optical emission spectrometry
LSV	Linear sweep voltammetry
MeOH	Methanol
NMR	Nuclear magnetic resonance

OCP	Open circuit potential
OER	Oxygen evolution reaction
PEF	Polyethylene 2,5-furandicarboxylate
PET	Polyethylene terephthalate
PLD	Pulsed laser deposition
PrOH	Propanol
PVD	Physical vapor deposition
SEM	Scanning electron microscopy
TEM	Transmission electron microscopy
XAS	X-ray adsorption spectroscopy
XANES	X-ray near-edge strcuture
XPS	X-ray photoelectron spectroscopy
XRD	X-ray diffraction

Abstract

Electrochemical CO_2 reduction reaction (CO_2RR) is a promising route as carbon utilization technique. One of the major challenges to commercialize this technology is the large applied potential needed due to the oxygen evolution reaction (OER) in the anodic half-cell, which reduces the energy efficiency of the system. To decrease the cell applied potential, 5-hydroxymethylfurfural oxidation reaction (HMFOR) toward 2,5-furandicarboxylic acid (FDCA) is proposed to replace the OER and improve the energy efficiency of the electrolytic system. However, a selective, active and stable catalyst for this reaction is lacking in the literature to be coupled with the CO_2RR at industrially relevant high current density (e.g., ≥ 100 mA/cm^2). In this thesis nickel-phosphorus (Ni-P) catalysts are synthesized and shown to have high Faradaic efficiency (90%) and stability (> 20 h) for the HMFOR. By adopting the active Ni-P as anode catalyst and Sn nanoparticles as cathode catalyst for the CO_2RR in a continuous flow cell reactor, high FDCA yield is achieved simultaneously with selective formate production. Moreover, an energy efficiency improvement of near 10% is realized compared to OER as the anode. This continuous CO_2RR-HMFOR electrocatalysis scheme is shown to be a stable and energy efficient electrochemical system.

French version

La réaction de réduction électrochimique du CO_2 (CO_2RR) est une voie prometteuse en tant que technique d'utilisation du carbone. L'un des principaux défis pour commercialiser cette technologie est le potentiel appliqué élevé nécessaire en raison de la réaction d'évolution de l'oxygène (OER) dans la demi-cellule anodique, ce qui réduit l'efficacité énergétique du système. Pour diminuer le potentiel appliqué à la cellule, la réaction d'oxydation du 5-hydroxyméthylfurfural (HMFOR) vers l'acide 2,5-furandicarboxylique (FDCA) est proposée pour remplacer l'OER et améliorer l'efficacité énergétique du système électrolytique. Cependant, un catalyseur sélectif, actif et stable pour cette réaction fait défaut dans la littérature pour être couplé au CO_2RR à une densité de courant élevée pertinente sur le plan industriel (par exemple, ≥100 mA/cm^2). Dans cette thèse, des catalyseurs au nickel-phosphore (Ni-P) sont synthétisés et montrent une efficacité faradique élevée (90%) et une stabilité (> 20 h) pour le HMFOR. En adoptant le Ni-P actif comme catalyseur d'anode et les nanoparticules de Sn comme catalyseur de cathode pour le CO_2RR dans un réacteur à cellule à flux continu, un rendement élevé en FDCA est atteint simultanément à la production sélective de formiate. De plus, une amélioration de l'efficacité énergétique de près de 10% est réalisée par rapport à l'OER car l'anode. Ce schéma d'électrocatalyse CO_2RR-HMFOR en continue s'avère être un système électrochimique stable et économe en énergie.

Acknowledgement

The author would like to thank the thesis supervisor Dr. Ali Seifitokaldani for his kind guidance and technical advisory on this thesis work.

This work is supported by Fonds de recherche du Québec – Nature et technologies (FRQNT) Master Scholarship, FRQNT New Researchers Fund, NSERC Discovery Grant, and Canada Research Chair.

The synchrotron XAS was done at the Canadian Light Source (CLS) in Saskatchewan, Canada. The author acknowledges Mohsen Shakouri, Qunfeng Xiao, and Alisa Paterson at CLS for their help during the XAS measurements. The author thanks Dr. Xue-Dong Liu at the Facility for Electron Microscopy Research of McGill University for help in microscope operation and data collection.

The author also acknowledges Chemical Engineering department technicians Ranjan Roy and Andrew Golsztajn for their kind help on equipment training and advice on product analysis methodology. The author thanks fellow students Elmira Pajootan, Mahdi Salehi, and Amirhossein Farzi for help on catalyst syntheses, Mahdi Salehi for SEM, XPS and XAS measurements, Dr. Sriraman K Rajagopalan for XRD measurements, Jiaxun Guo, Xiao Wang, Kefang Liu, and Jiashuai Han for feedback on experiment.

1. General Introduction

With increasing atmospheric carbon dioxide concentration, human society is facing the challenge of global warming, which is the precursor to more frequently occurring extreme weathers, rising sea levels, decreasing fresh water resources and worsening ecosystems and habitats for many life forms both on land and in ocean [1].

To alleviate the CO_2 emission problem, a carbon negative/neutral process that is economical and beneficial to the society is much desired and thus has become intensively popular research area in recent years. Numerous approaches have been studied, and efforts have been spent toward implementation in industrial scale. Some state-of-the-art CO_2 utilization methods include electrochemical reduction [1-5], thermal catalysis [6-10], photochemical reduction [11-15], photoelectrochemical reduction [16-20], enzymatic reduction [21-25], and plasma-based conversion [26, 27]. These methods demonstrate the variety of technologies possible for future renewable energy sources and circular economy of material utilization aiming at a carbon-neutral or even carbon-negative objective. The primary requirement for the energy input in these conversions, however, is that it must be a renewable and low carbon footprint energy source. For instance, the energy intensive processes in thermal catalysis such as high temperature must come from renewable heat sources such as biomass or clean electricity; similarly, electrochemical reduction must be supplied with clean electricity, while photoelectrochemical and photochemical methods obviously utilize solar energy directly, and enzymatic conversions of CO_2 take advantage of biological metabolism.

Among these methods, the electrocatalytic reduction of CO_2 is under an unprecedented amount of study because of its additional advantage to convert intermittent or excessive renewable electricity into stored chemical energy and its facile implementation on existing fuel consumption sectors to close the gap between conventional high-carbon economy and a sustainable low-carbon one [28-30]. Recent development in electrocatalytic carbon dioxide reduction reaction (CO_2RR) has shown promising advancement in industrializing valuable chemical production such as formate and carbon monoxide. Much focus takes place in the development of novel electrocatalysts followed by the optimization of the reaction parameters such as the carbon dioxide pressure and flowrate, electrolyte composition and temperature [1, 31-33]. These efforts are mostly aiming at higher Faradaic efficiency (FE) and energy efficiency (EE) toward the desired product, longer stable production period, and lower overpotential.

An overall challenge remains in the overpotential of the applied voltage across the whole cell, including both the cathode and anode. Due to the requirement of a large applied potential on the conventional anodic oxygen evolution reaction (OER), it costs extra energy input into the system and thus reduces the energy efficiency of the electrolyzer. Additionally, the produced oxygen gas has a low market value and remains relatively expensive to produce in an electrolyzer, package and sell as a by-product of the electrolysis. This then results in oxygen generated being a valueless reaction product at the counter electrode that needs to be vented [34].

One particularly interesting idea for alternative anode reaction in a CO_2RR electrolyzer is the electrooxidation of furanic materials, among other organic compounds such as alcohols, glycerol, and sorbitals [35]. They generally exhibit lower overpotential when electrooxidized compared to oxygen evolution reaction (OER), providing an energy saving in addition to useful work done during the various chemical conversions [36-39].

5-hydroxymethylfurfural (HMF, molecule shown in following section) is one of the biomass derivatives that can be valorized into useful platform chemicals such as 2,5-furandicarboxylic acid (FDCA, molecule shown in following section). HMF can be obtained from dehydration of hexoses, such as glucose and fructose, which are readily available from cellulosic biomass [40]. The HMF molecule has a hydroxymethyl group and a formyl group on top of the furan ring, allowing oxidation on both groups to become carboxylic acids. FDCA is an important precursor monomer which can be polymerized to form biomass-derived polyethylene 2,5-furandicarboxylate, or polyethylene furanoate (PEF). The electrochemical HMF oxidation reaction (HMFOR) to FDCA is a highly researched half-cell reaction, having the potential to allow a sustainable route to the circular economy in biorefinery [41]. The HMFOR is therefore a promising candidate to replace the OER in the anode. This combination of the two half-cell reactions can not only help improve the overall energy efficiency of the system, thus saving input energy, but also simultaneously produces useful products in both reaction chambers.

2. Literature Review

2.1. CO_2RR

Carbon dioxide reduction reaction (CO_2RR) was discovered by Teeter and Rysselberghe in 1954 [42]. From the late 60s to the early 80s, CO_2RR was proposed by several research groups toward the production of mainly formate, oxalate and carbon monoxide [43-46]. Since then, extensive research on CO_2RR has been increasing, and different approaches with various reactor

designs have given rise to multiple renewable chemical products within which some bear the potential to be scaled up and commercialized. The mechanism of CO_2RR in aqueous medium has been studied profoundly and two routes were identified: (1) $*CO_2$ (adsorbed molecule) goes through surface hydrogenation, becomes *OCHO, and desorbs as formate ion; (2) $*CO_2$ is transformed to *COOH and either desorbs as carbon monoxide or interacts with other adsorbed species and becomes alcohols, hydrocarbons or organic acids [1]. Figure 1 below shows common CO_2RR products and their applications [47].

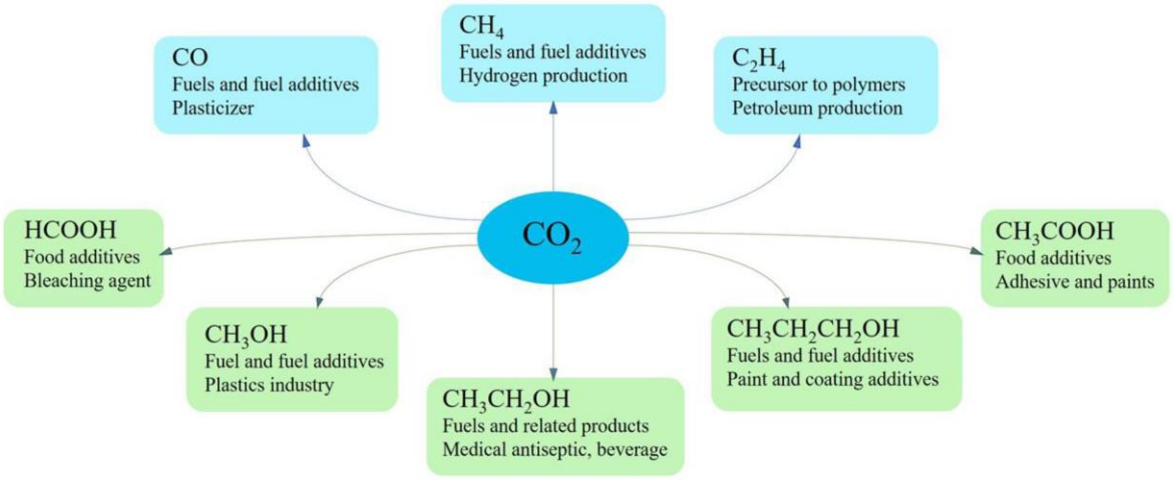

Figure 1 Common CO_2RR products in gas phase (light blue) and in liquid phase (light green), with their applications [47].

2.1.1. Cathode Catalysts

Catalyst plays a critical role in CO_2RR when certain groups of products are being targeted. Typically, catalysts for CO_2RR include metal-based catalysts such as Cu, Au, Ag, Sn, Bi and non-metal elements such as graphene, nanodiamond and carbon nanotube (CNT) etc. The selection of catalyst directly defines the possible reaction pathway and intermediate energy states.

Specifically, catalysts with compositions varying from pure metals [5, 48-52], alloys or multi-metallic materials [53-57], metal organic frameworks [58-60], non-metal carbon-based materials [61-63], and other non-metal materials [64] exist in current research stage. The reaction mechanism has been heavily studied and according to recent mechanistic investigation reports, Ag and Au catalysts are leading to CO formation, Pb, Sn and Bi catalysts yield predominantly formate or formic acid depending on the pH of electrolyte, and only Cu-based catalysts or some non-metal catalysts can produce multicarbon products [1, 65]. Since the objective here is to improve energy

efficiency of CO_2RR, Sn and Cu are used as efficient catalysts for production of formate and C_{2+} products, respectively.

2.1.2. Products

Among the various CO_2RR products reported, the most common ones are carbon monoxide (CO), formic acid/formate (HCOOH or $HCOO^-$), methane (CH_4), methanol (CH_3OH), ethylene (C_2H_4), acetic acid/acetate (CH_3COOH or CH_3COO^-), ethanol (CH_3CH_2OH), and 1-propanol ($CH_3CH_2CH_2OH$). The electron transfer in each of the mentioned products along with the main competing reaction, hydrogen evolution reaction (HER), is summarized in Table 1.

Table 1 Summary of common CO_2RR and HER products in aqueous solution, standard potentials [V vs. RHE] at 1 atm and 25 °C, and the number of electron transferred [66-68].

Product (phase)	**Cathode Reaction**	**E° [V vs. RHE]**	**Z**
CO (g)	$CO_2(g) + 2H_2O(l) + 2e^- = CO(g) + 2OH^-$	– 0.106	2
$HCOO^-$ (aq)	$CO_2(g) + H_2O(l) + 2e^- = CHOO^-(aq) + OH^-$	– 0.250	2
CH_3OH (l)	$CO_2(g) + 5H_2O(l) + 6e^- = CH_3OH(l) + 6OH^-$	0.016	6
CH_4 (g)	$CO_2(g) + 6H_2O(l) + 8e^- = CH_4(g) + 8OH^-$	0.169	8
$C_2O_4^{2-}$ (aq)	$2CO_2(g) + 2e^- = C_2O_4^{2-}(aq)$	0.238	2
CH_3COO^- (aq)	$2CO_2(g) + 5H_2O(l) + 8e^- = CH_3COO^-(aq) + 7OH^-$	0.125	8
C_2H_5OH (l)	$2CO_2(g) + 9H_2O(l) + 12e^- = CH_3CH_2OH(l) + 12OH^-$	0.084	12
C_2H_4 (g)	$2CO_2(g) + 8H_2O(l) + 12e^- = C_2H_4(g) + 12OH^-$	0.064	12
C_3H_7OH (l)	$3CO_2(g) + 13H_2O(l) + 18e^- = CH_3CH_2CH_2OH(l) + 18OH^-$	0.095	18
H_2 (g)	$2H_2O(l) + 2e^- = H_2(g) + 2OH^-$	0.000	2

At low applied voltage, the simplest product of CO_2RR in liquid phase is formate (Equation 1) because of its low requirement of electron transfer (2 electrons per formate ion formed) [1]. The competing reduction reaction in the cathode is hydrogen evolution reaction (HER) shown in Equation 2.

$$CO_2(g) + H_2O(l) + 2e^- \rightarrow HCOO^-(aq) + OH^-(aq) \quad (1)$$

$$2H_2O(l) + 2e^- \rightarrow H_2(g) + 2OH^-(aq) \quad (2)$$

However, one of the all-time obstacles of the electrocatalysis on CO_2RR is the extra requirement of energy when the anodic OER (Equation 3) is to be used to balance the electron and charge transfer in the full cell.

$$4OH^- \rightarrow 2H_2O + O_2 + 4e^- \quad (3)$$

With the OER occurring at the anode, full cell potential of the electrolyzer will include the anodic potential for the OER, which has a comparatively high equilibrium standard potential E° = 1.23 V vs. RHE [69]. Studies have been carried out as efforts in improving OER catalyst performance [70], but because of the considerable equilibrium potential with a magnitude higher than that of the applied cathode potential for CO_2RR, it still results in low full cell energy efficiencies. The anodic overpotential resulting from catalytic oxidation of water molecules is also present. During the electrooxidation of water, it is found to be thermodynamically difficult when converting *OH to *OOH intermediates, thus the activation energy yields elevated "thermodynamic overpotential" [69, 71, 72]. Moreover, for each oxygen gas molecule formed, two water molecules need to be oxidized, rendering the process slow in kinetics nature [73]. This results in high OER overpotential (at least 0.26 V at only 10 mA/cm^2) in the anode half-cell of the electrolyzer, which makes the onset potential of OER about 1.5 V vs. RHE or higher [37, 74, 75]. The result is high applied potential across the electrolyzer for a fixed current, and low energy efficiency across the electrolyzer.

Economically, there are processes for commercial production of oxygen with higher throughput that cost less, rendering O_2 production through OER uncompetitive and not feasible. Oxygen gas produced in the anode would have to be vented in industrial scale CO_2RR. Maintenance-wise, in an aqueous solution, the newly formed, reactive oxygen gas can lead to corrosion and oxidation of metal in the reactor, damaging the integrity of the electrolyzer and causing more maintenance costs throughout the production period.

Therefore, it creates a need for the development of an oxidation with a lower overpotential which can effectively result in a reduce in the applied full cell potential. This challenge evokes the main goal of this investigation aiming to adopt a newly explored oxidation reaction of 5-hydroxymethylfurfural (HMF) to replace the original OER, which has been shown to lower the applied full cell potential by ~200 mV [35, 36] (Figure 2).

2.2. HMFOR

HMF is a biomass-derived furanics chemical that is usually produced from dehydration of pentose or hexose sugars while its oxidation product, 2,5-furandicarboxylic acid (FDCA), is considered an important platform chemical and precursor in many industrial polymer syntheses [76, 77]. The feasibility of this conversion was improved when it was implemented in the field of electrochemistry from earlier aerobic thermal oxidation, while providing some insights on the

mechanism of the reaction [78]. It has been discovered that the oxidation of HMF has two paths as the first step, one through the oxidation of the aldehyde group yielding an intermediate called 5-hydroxymethyl-2-furancarboxylic acid (HMFCA), another through the oxidation of the hydroxyl group via 2,5-diformylfuran (DFF), but both ways lead to the common intermediate 5-formyl-2-furancarboxylic acid (FFCA) final product of FDCA (Figure 3) [78-81].

Based on the previous studies on HMF electrooxidation, the onset potential of HMFOR is found to be lower than the onset of OER in a range from 150 mV to 270 mV when 5 mM or 10 mM of HMF is added depending on the catalyst [36, 38, 82]. It is therefore proposed that HMFOR can be a substitute for the anodic reaction to maximize the energy efficiency and lower the voltage input while creating value-added products such as FDCA. Applying this novel idea into the design of a CO_2RR electrolyzer, some preliminary lab work has inspected the effect of addition of HMF to the anodic half cell while performing carbon dioxide reduction reaction in the cathode. In addition to reducing the overpotential of the electrolyzer, simultaneous production of value-added carbon products at the cathode and FDCA at the anode was realized. Due to this effect on the applied potential, the full cell applied potential was as low as 2V at 10 mA/cm^2. This effectively increases the voltage efficiency of the electrolyzer, although the FDCA selectivity was not too high (> 55%). In order to improve the activity and selectivity on HMFOR, a more robust catalyst design is needed.

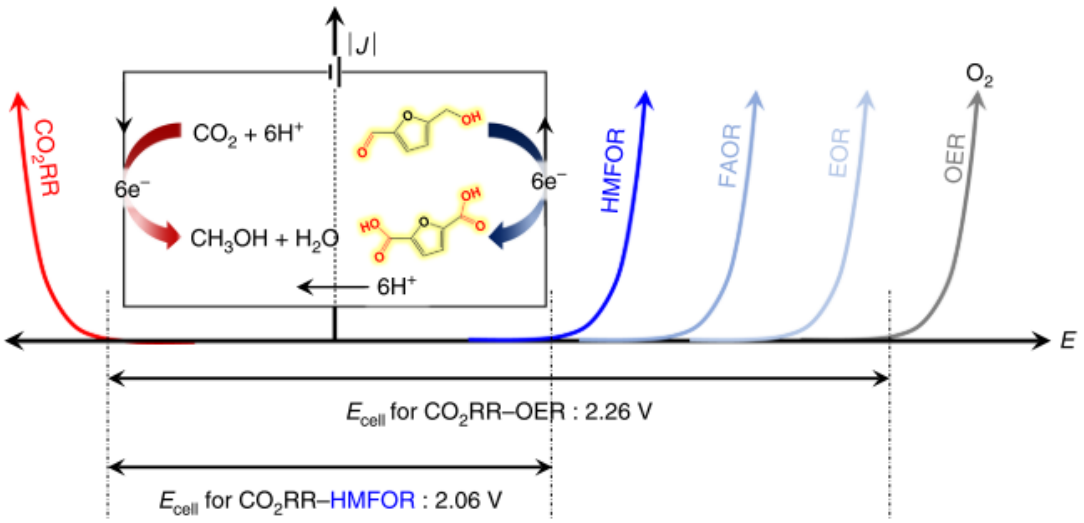

Figure 2 Illustration on theoretical full cell potential for alternatives of anode catalytic reactions. HMFOR: HMF oxidation reaction; FAOR: furfural alcohol oxidation reaction; EOR: ethanol oxidation reaction; OER: oxygen evolution reaction; CO_2RR: CO_2 reduction reaction. Adopted from Na, Seo [35].

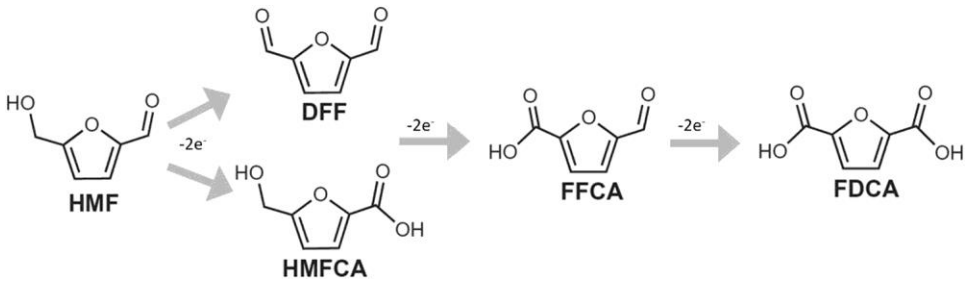

Figure 3 Oxidation pathways of HMF toward FDCA. Adapted from Latsuzbaia, Bisselink [81].

2.2.1. Anode Catalysts

Early works on HMFOR was done via an aerobic oxidation process using precious metals such as Au and Pd, and the reaction conditions are generally harsh (high temperature, high O_2 pressure, toxic chemical agents etc.) [83]. In addition to the expensive materials, noble metal catalysts of Au, Pt and Pd were not particularly selective for the final product FDCA, so the focus was later drawn to more accessible and cheaper transitional metal catalysts including Ni, Co, Fe, and Cu [84-87]. From literature, the development of HMFOR catalyst is mainly focused on Ni-based catalysts due to its excellent oxidative catalyzing ability toward alcohol groups [88]. The catalyst can be oxidized Ni electrode [89], Ni-based bimetallic catalysts [90], or Ni-doped non-metals [36, 91, 92]. Nickel oxide hydroxide (NiOOH) was compared with cobalt oxide hydroxide (CoOOH) and iron oxide hydroxide (FeOOH) by Taitt et al., and it was found that NiOOH has the best catalytic capability followed by CoOOH [93]. Beside Ni, Co is another commonly used catalyst for HMFOR toward FDCA [82, 94, 95]. Recent work has shown that bimetal catalysts have greater catalytic activity for both OER and HMFOR [90, 96]. Specifically, Ni element has beneficial synergistic effect when combined with another transition metal such as Co, allegedly resulting from increased surface area, lowered charge transfer resistance, higher electric conductivity, and more active sites [97-100]. In addition to metallic elements, p-block elements are also found to be a helpful component in the Ni-based catalysts for improvement on charge transfer and catalyst structure thus higher activity [36, 38, 91, 101]. Therefore, Ni-p-block catalyst is a promising direction to investigate new catalysts and reaction mechanism in HMF to FDCA production. A brief summary of the previously studied catalysts is shown in Table 2.

Table 2 A brief summary of catalysts for HMFOR and some of their reaction parameters.

Electrode Materials	HMF [mM]	Electrolyte	Potential [V RHE]	Current density [mA cm^{-2}]	Tafel slope [mV dec^{-1}]	FDCA yield [%]	FDCA FE [%]	Ref.
$NiCo_2O_4$/NF	5	1M KOH	1.53	14.83	135.7	90.8	87.5	*[82]*
Ni_xB/NF	10	1M KOH	1.45	100	N/A	98.5	~100	*[91]*
NiFe LDH	10	1M KOH	1.33	36.9	75	98	98.6	*[90]*
Ni_2P NPA/NF	10	1M KOH	1.423	> 200	N/A	100	98	*[36]*
Ni_3S_2/NF	10	1M KOH	1.423	> 200	N/A	100	98	*[38]*
NiCoFe LDH	5	1M NaOH	1.52	10	68	84.9	~90	*[85]*
hp-Ni	10	1M KOH	1.423	80	N/A	~100	98	*[102]*
Ni_3N@C	10	1M KOH	1.38	50	48.9	98	99	*[103]*
Co-P/CF	50	1M KOH	1.38	20	N/A	~90	~90	*[95]*

3. State of the Problem

For the CO_2RR, several studies have shown promising selectivity and activity for different products such as formate, carbon monoxide, ethylene, etc. [2]. However, techno-economic analysis (TEA) shows that only some of the products so far can be economically feasible when scaled up, namely CO and formic acid [68, 104]. Meanwhile, multi-carbon or C_{2+} products such as ethanol and ethylene with more significant market demand require lower operational costs to be economically viable [1, 105]. The major problem as mentioned in previous subsection lies in the overpotential of the whole electrolyzer when considering anode reaction to be only the OER [35, 73]. Therefore, the action needed for improving the scale-up ability of the CO_2RR toward these renewable fuels is an alternative anodic pair reaction for the electrolyzer. One of the best options for anode reaction has been proposed to be the HMFOR, which can also add value to the anode product (FDCA) instead of O_2 [35]. However, in preliminary HMFOR experiments, challenges remain in terms of low current density compared to the cathode CO_2RR counterpart, thus, a more catalytically active catalyst is needed. In this thesis, we aim to improve the catalytic performance of conventionally utilized Ni-based catalysts through adding *p*-block elements into their structure. This modification is hypothesized to change the electronic structure and charge carrying properties of the catalyst to attain the required activity (i.e., current density) while maintaining the selectivity high. In particular, we synthesized and tested Ni-P catalyst for the HMFOR first and the combined system for CO_2RR-HMFOR in continuous flow cell, with which performance such as the energy efficiency is examined in this project.

4. Objectives

Combining CO_2RR and organic oxidation reactions such as HMFOR in a viable device which realizes CO_2 conversion, biomass upgrading and renewable energy storage, is the ultimate goal of this research thesis. As an alternative anodic electrooxidation, the 5-hydroxymethylfurfural oxidation reaction (HMFOR) is shown to effectively lower the overpotential on anode and perhaps provide higher FE in the cathode reaction. At the same time, value-added HMFOR product 2,5-furandicarboxylic acid (FDCA) is also produced. As this novel approach to an efficient and selective reaction is considered a more practical way to scale up CO_2RR operations, performance metrics on current density, Faradaic efficiency, energy efficiency and stability are all part of the verification on the developing system. This thesis work aims to improve the energy efficiency of the CO_2RR electrolyzer while achieving Faradaic efficiency above 90% for HMFOR products at high current density of 100 mA/cm^2.

The main work in this thesis program is divided into two parts:

1. Stage 1 - HMFOR.

The first stage kicks off with home-made Ni-based catalysts via electrochemical and chemical reduction method. Synthesized catalysts go through a series of physiochemical and electrochemical characterizations to inspect the catalytic activity. Furthermore, other synthesis methods of catalyst are explored, such as PVD and electrodynamic (pulse) treatment. Meanwhile comparisons between synthesized catalysts and HMFOR performance analyses are carried out to aim for high current density and low overpotential.

2. Stage 2 - Combined system.

After the HMFOR achieves reliable results, the catalyst preparation method is adopted to synthesize catalysts for continuous flow-cell reactor, combining CO_2RR and HMFOR in the same electrolyzer. This involves testing of different CO_2RR catalysts, adjustment, and characterization of the full electrolyzer to achieve high current density, Faradaic efficiency, energy efficiency and stability as a viable electrochemical system.

5. Materials and Methodology

Full laboratory procedure is consisted of reactor assembly, catalyst syntheses, electrolyzer assembly, catalyst and system characterization, and product analyses. This general procedure serves to help the project go smoothly and to achieve the stated objectives.

First, two types of reactors are used. Conventional H-type cell, or H-cell, is used for HMFOR catalyst screening and HMFOR half-cell experiment (Figure 4). Flow-cell is used for continuous CO_2RR experiment especially when combined with HMFOR (Figure 5).

Catalysts are synthesized guided by literature and previous work in the lab, with modifications to provide desired functionalities and experiment outcomes. Cathode and anode catalysts are manufactured separately when needed. Methodologies involved in manufacturing catalyst electrodes include electron-beam physical vapor deposition (PVD), chemical reduction followed by drop-casting, electrodeposition, and electroless plating. The main preparation methods for this research are introduced in the Appendices.

Then preliminary testing and electrochemical experiment are conducted using an H-cell electrolyzer. Most experiments are run in flow-cell configuration instead of H-Cell, for better mass transfer of CO_2 [1, 106]. However, when variations of catalyst synthesis method need to be examined quickly, an H-cell may be used for quick scanning and verification.

Next, two types of major characterization techniques will be involved to learn about the catalysts and verify their performance and reaction mechanism. The first type is physiochemical characterization techniques including scanning electron microscopy (SEM), transmission electron microscopy (TEM), X-ray photoelectron spectroscopy (XPS), X-ray adsorption spectroscopy (XAS), and X-ray diffraction (XRD). The second type is investigation on the system electrochemical properties, which include: cyclic voltammetry (CV), linear sweep voltammetry (LSV), electrochemical impedance spectroscopy (EIS), chronoamperometry (CA), and chronopotentiometry (CP). Each one of these is briefly explained in the Appendices.

Last, the CO_2RR and HMFOR products from CA and CP experiments are analyzed with either gas chromatography (GC), high-performance liquid chromatography (HPLC) or nuclear magnetic resonance (NMR) spectroscopy depending on the physical state and properties of the products. These methods are also explained in the Appendices.

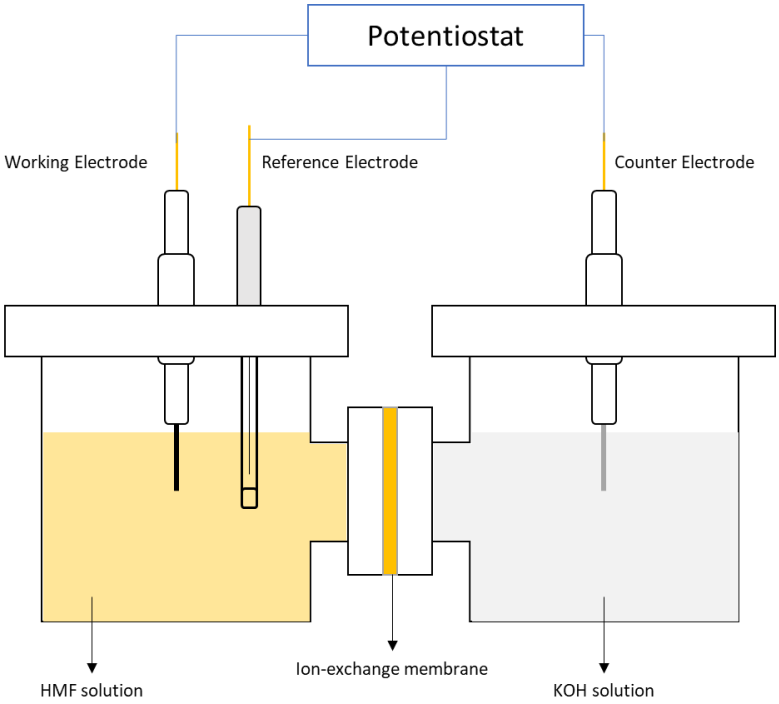

Figure 4 H-cell configuration of HMFOR with 1 M KOH in both half-cells and HMF in anode.

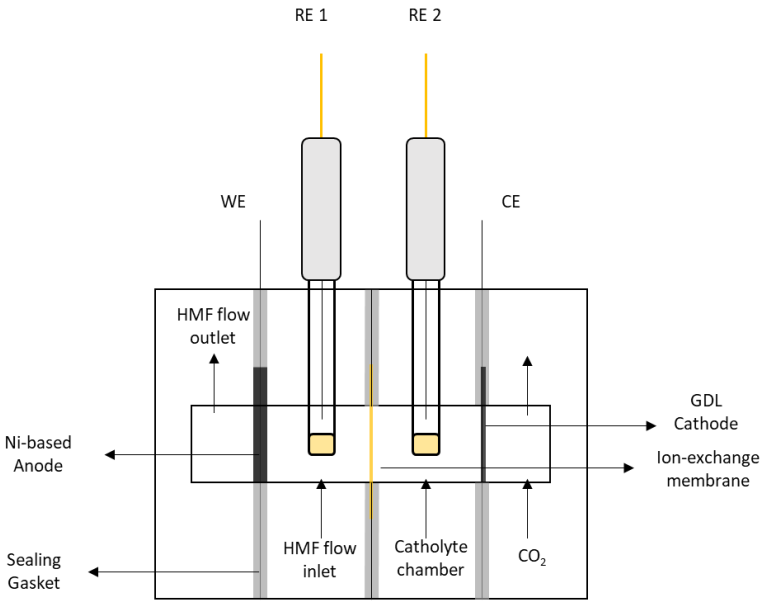

Figure 5 Flow-cell structure with body components.

6. Results and Discussions

6.1. HMFOR

In the first stage of work, HMFOR is studied in H-cell by Ni-P catalyst, which is synthesized by cathodic Ni plating on thin (2nm) Ni-deposited carbon paper substrate (NiP@Ni/C). Detailed synthesis method can be found in the Appendices. The as-synthesized Ni-P catalyst appear to be light silvery, with some green spots, indicating some nickel phosphite deposited on the carbon paper (Figure A5). After CV treatment in 1 M KOH that goes beyond Ni oxidation potential (>1.36 V vs. RHE), the catalyst becomes dark and green spots disappear, suggesting a reconstruction under anodic applied potential. Control catalysts include thin Ni/C itself, thick (200nm) Ni/C, both prepared by PVD, as well as pulse treated NiOOH on nickel foam (NiOOH/NF).

6.1.1. Catalyst Characterizations

SEM in Figure 6 shows that the surface of Ni-P catalyst is covered by a deposited layer compared to the thin Ni/C, while thick Ni/C and NiOOH/NF share similar sheet-like morphology of nickel species. Due to the obvious difference in surface area, the activity analysis is mostly normalized by the electrochemical active surface area (ECSA) in following subsections. ECSA is determined via CV in non-Faradaic region, details can be found in the supporting information.

Energy-dispersive X-ray spectroscopy (EDX) coupled with SEM shows the uniform distribution of Ni, P and O, in Figure 7. A sublayer of Ni-P is found connecting to deeper layer in the carbon substrate. This is also verified by the high-resolution HR-TEM and high-angle annular dark-field imaging (HAADF) in Figure 8. The surface morphology appears to be amorphous, which is also found by other researchers [97, 107-109]. XRD confirms the amorphous nature of the Ni-containing layer on Ni-P catalyst while showing some potential Ni-P oxidation compound (Figure 9), which can be the sublayer P-containing active component.

XPS further confirms the active catalyst surface has Ni^{3+} (857.2 eV) and Ni^{2+} (855.7 eV), indication of the active NiOOH formation under oxidation condition [110]. The bulk of the catalyst also contains phosphorus as expected, as shown in Figure 10. When the surface is oxidized under anodic potential, Ni^{3+} is generated, in the form of NiOOH, same as other Ni-based catalysts [81, 111]. Higher oxidation state on the surface as well as the sublayer of the catalyst is indicated by X-ray adsorption near edge spectra, or XANES Figure 11. The extended X-ray adsorption fine

structure results also reveal a slightly shortened first neighbour bonding when NiP@Ni/C is oxidized. Meanwhile, Ni-Ni, Ni-O and Ni-P bonding can be found in the catalyst.

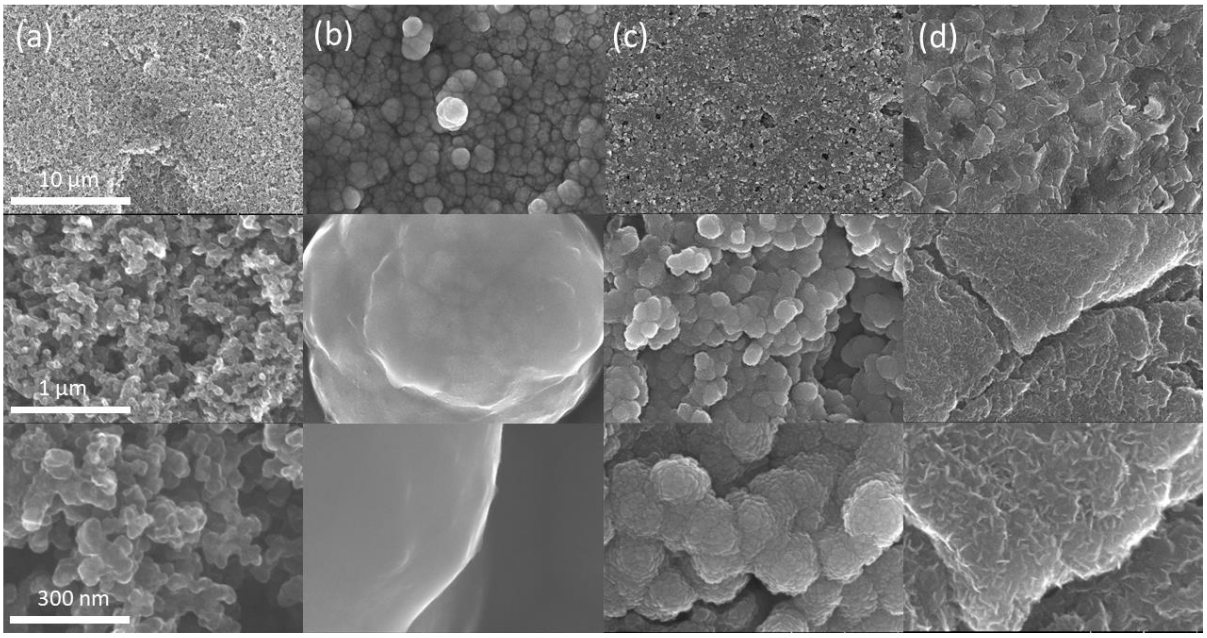

Figure 6 SEM images of thin (a) Ni/C; (b) NiP@Ni/C; (c) thick Ni/C; (d) NiOOH/NF.

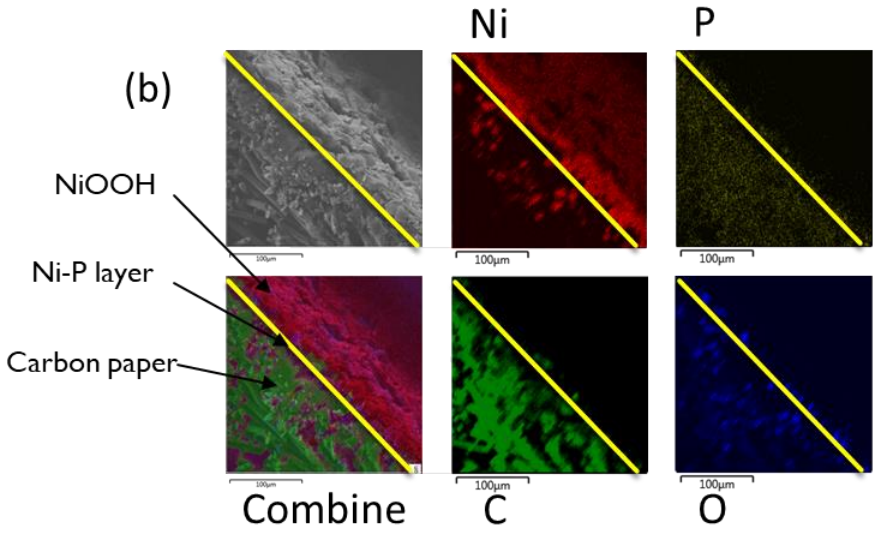

Figure 7 EDX spectra for Ni, P, O and carbon detection on NiP@Ni/C.

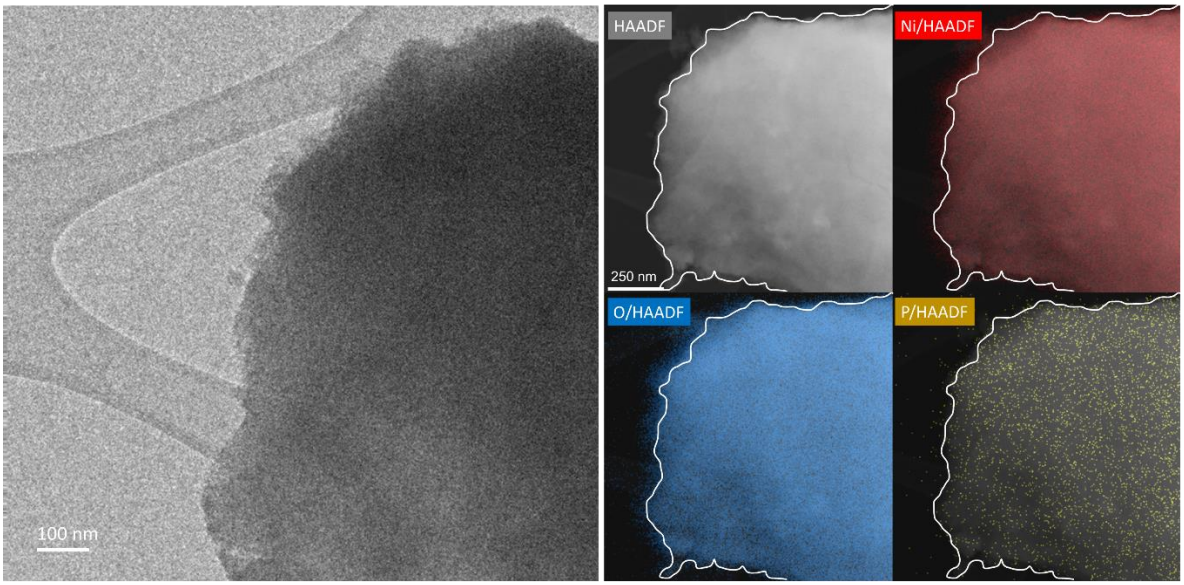

Figure 8 HR-TEM and HAADF show the distribution of elements, namely Ni, P, and O.

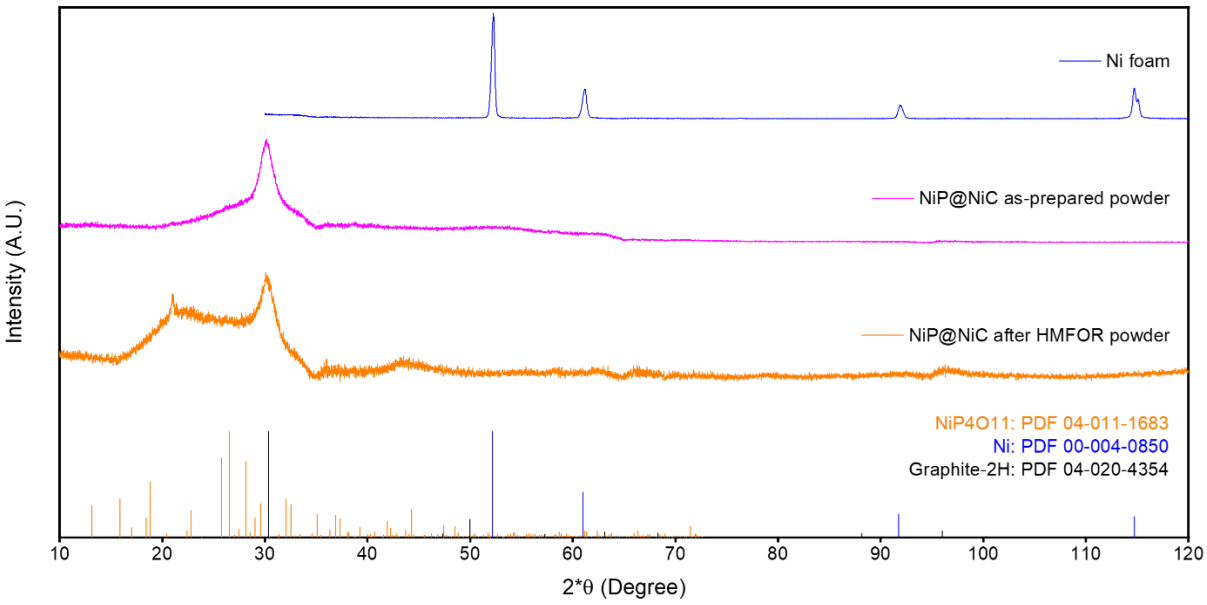

Figure 9 XRD on Ni foam and scratched NiP@Ni/C powder samples before and after HMFOR.

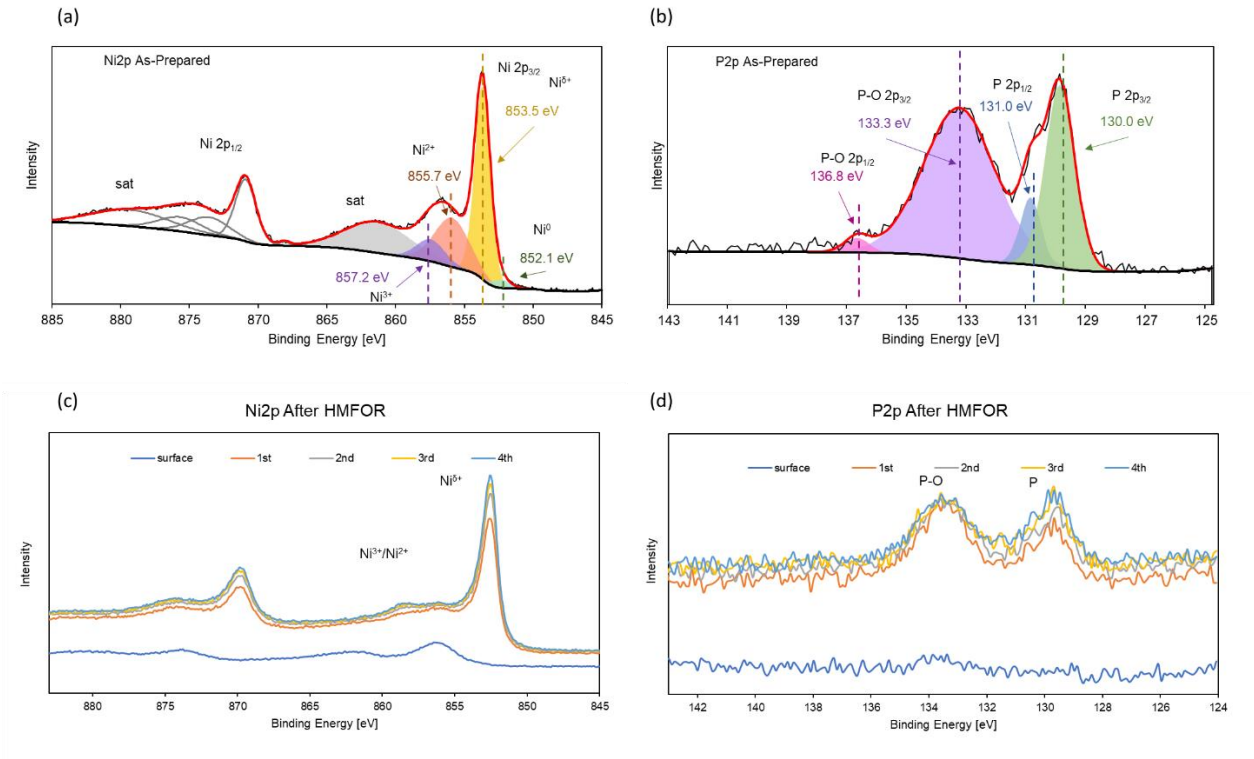

Figure 10 XPS on as-prepared NiP@Ni/C on (a) Ni 2p and (b) P 2p spectra; XPS on post-HMFOR NiP@Ni/C on (a) Ni 2p and (d) P 2p spectra.

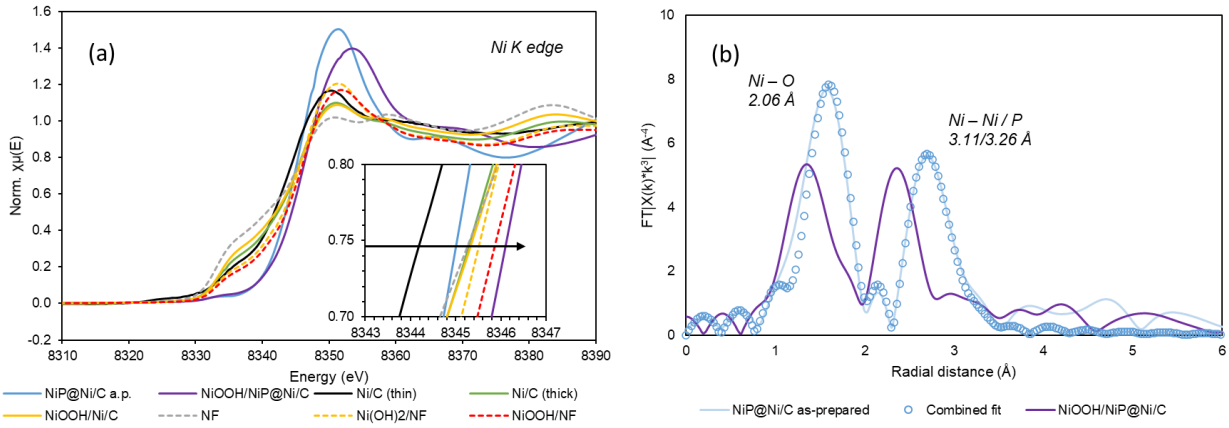

Figure 11 XANES (a) and EXAFS (b) results indicating Ni oxidation and neighbouring atoms.

6.1.2. Active Site Analysis

It is expected that NiOOH is mainly responsible for the oxidation of HMF, due to the activity of Ni^{3+} with hydroxy group containing organic species [112]. A simple scan of CV can verify that the surface active site is indeed Ni^{3+}. In Figure 12, during the forward scan, current density increases rapidly after 1.36 V on NiP@Ni/C, which is attributed to the nickel oxidation

from Ni^{2+} to Ni^{3+} (R1 in Scheme 1), while during the backward scan, the nickel reduction peak is smaller than the case without HMF. This reveals a partial reduction of the NiP catalyst because of spontaneously react with surface adsorbed HMF molecules (R2), resulting in an indirect oxidation even in the case without an applied current or potential (R3) [113]. At higher applied potential, it has also been seen that a direct oxidation without the reduction of Ni^{3+} is possible (R4). Finally, the oxidation of HMF on Ni^{2+} is insignificant, compared to the Ni^{3+} activity and reaction rate, as almost zero current was passed during the CV before Ni^{3+} becomes present.

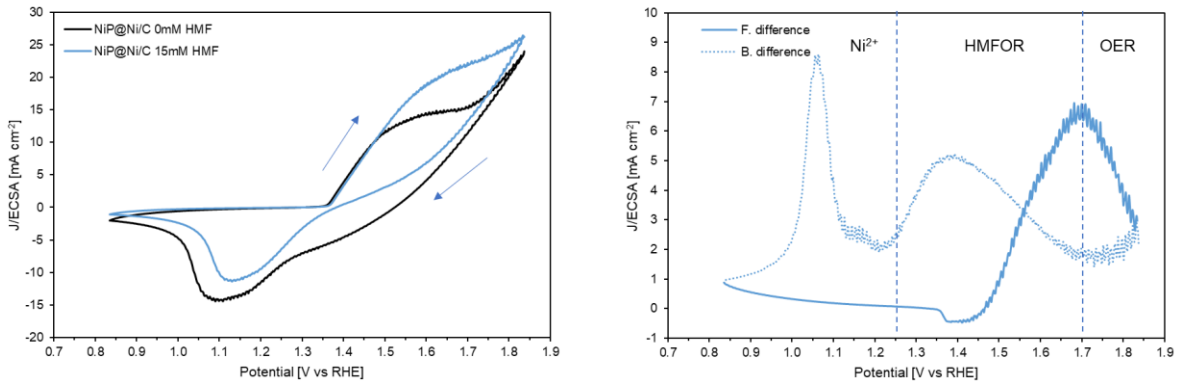

Figure 12 CV of NiP@Ni/C with and without HMF, on the left. A subtraction between the forward and backward scan on the right show the active region for OER, HMFOR and Ni reduction.

$$OH^- + Ni(OH)_2 \xrightarrow{-e^-} NiOOH + H_2O \quad \text{(R1)}$$

$$HMF_{bulk} \longrightarrow HMF_{ads} \quad \text{(R2)}$$

$$HMF_{ads} + NiOOH \xrightarrow{RDS} Ni(OH)_2 + intermediates \quad \text{(R3)}$$

$$HMF_{ads} + OH^- \xrightarrow{-e^-,\ NiOOH} intermediates \quad \text{(R4)}$$

$$HMF_{ads} + OH^- \xrightarrow[minimal]{-e^-,\ Ni(OH)_2} intermediates \quad \text{(R5)}$$

Scheme 1. HMF reaction steps on $Ni(OH)_2$/NiOOH catalyst in aqueous alkaline condition.

6.1.3. Electrochemical Performance

LSV from the OCP to the more anodic OER region (> 1.8 V) of the NiP@Ni/C in 1M KOH with 15 mM HMF is compared to LSV of thick NiC, NiOOH/Ni/C and NiOOH/NF using the ECSA-normalized current in Figure 13. The onset potential of Ni-P catalyst for Ni oxidation and the HMFOR is shown to be smaller than the other catalysts from the LSV tests.

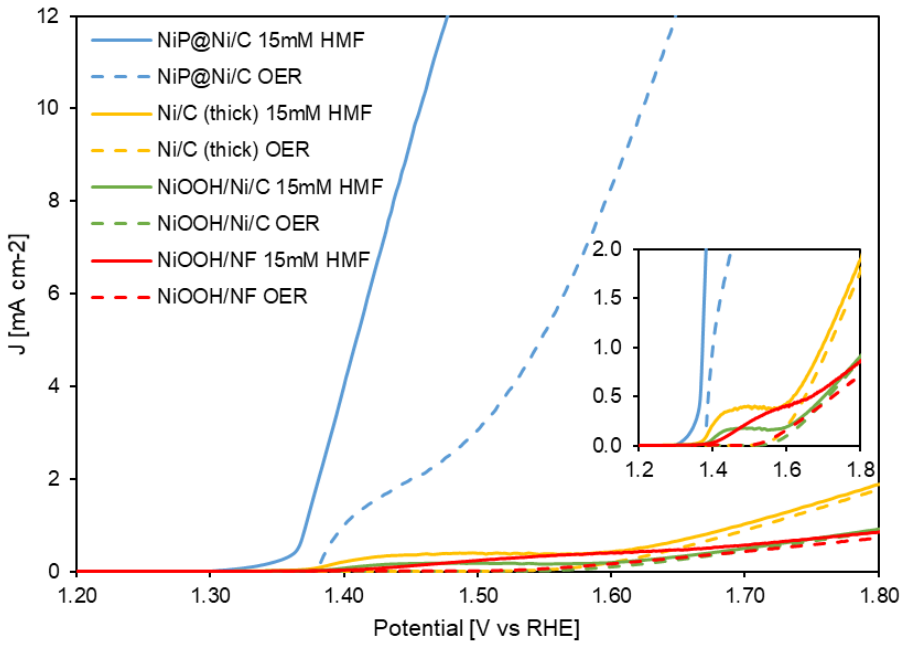

Figure 13 LSV comparison between Ni-P catalyst and other control samples in 1 M KOH. Note: At potentials more anodic than 1.36 V, the Ni surface of the catalysts will be occupied by Ni^{3+} species.

Stepwise chronoamperometry is carried out and polarization curves are plotted to compare the quasi-steady state current at each applied potential near the onset of Ni oxidation as shown in Figure 14a, which confirms the same observation from LSV that the Ni-P catalyst has lower onset potential for the HMFOR. Tafel slopes extracted from the polarization curves confirm the higher activity for the HMFOR (33.4 mV dec^{-1}) compared to the OER (67.2 mV dec^{-1}) by Ni-P catalyst in Figure 14b. It also shows that the other catalysts have similar Tafel slopes for the HMFOR and the OER, with lower exchange current density compared to Ni-P. This indicates that Ni-P has better selectivity for the HMFOR under competition against the OER and requires less applied potential to reach the same specific reaction activity.

Chronoamperometry test over the course of 30 minutes is conducted at 1.48V with 15 mM HMF to investigate the selectivity of the HMFOR. The results show that the Ni-P catalyst has the highest Faradaic efficiency of 90% towards FDCA (Figure 14c). The other catalysts without phosphorus content in the catalyst have more intermediates (HMFCA and FFCA) in comparison. The thin Ni/C catalyst with Ni nanoparticles does not generate a good amount of FDCA (< 37%) in 30 minutes, which is due to the low current density and lack of continuous charge transport to the active sites. On the contrary, given that the HMF to FDCA conversion is a six-electron transfer process, the high Faradaic efficiency towards the final product achieved by Ni-P catalyst with its

high specific activity, demonstrates highly active surface and high specific charge transfer rate from the catalyst to the adsorbed HMF and intermediate molecules. Full conversion chronoamperometry test with 5 mM HMF at the same applied potential for Ni-P is performed (Figure 14d), and the electrolyte is processed by high performance liquid chromatography (HPLC) for product analysis (Figure A25). The results reveal the consistent high selectivity (>90%) towards FDCA over the whole conversion process, whereas the intermediates remain in the electrolyte are kept low. In fact, at short time experiments, Ni-P catalyst already achieved immediate high FE (above 80% in 5 minutes) towards FDCA. This indicates that Ni-P catalyst enables stable charge transfer to the adsorbed intermediates quickly enough so most of them become oxidized to the final FDCA before desorption from the catalyst surface. The gradually decreasing total carbon balance is due to the degradation of HMF in alkaline environment into humin type products and possibly a small amount of CO_2 [114].

From experiment, the performance of NiP@Ni/C is superior to the other Ni catalysts, in both FDCA selectivity and specific activity, demonstrated by Faradaic efficiency and normalized current density, respectively, as plotted in Figure 14e. There is also evidence of faster kinetics on apparent charge transfer shown by the EIS. By fitting the EIS Nyquist plot, the charge transfer resistance of the HMFOR on NiP@Ni/C is 13.0 Ω at 1.38V (Figure 14f), which is the lowest among the other catalysts. The other two samples that have nickel deposited on carbon paper (Ni/C or NiOOH/Ni/C) demonstrate much higher charge transfer resistances of the HMFOR (45.4 Ω and 51.7 Ω). Since the active sites are nickel oxyhydroxide and their morphology is similar, the difference in electrochemical impedance is attributed to the lack of an oxidized Ni sublayer that supports the oxidation of HMF on the surface.

Stability tests repeated in one hour interval for 10 cycles (Figure 14g) show that the Ni-P catalyst can consistently perform HMFOR with high FE towards FDCA (> 90%). In each cycle, the initial anodic current density is evidence of Ni species oxidation in the electrode, whereas the later smooth current indicates a continuous oxidation of HMF molecules. The decrease of current density is due to the decrease of HMF concentration in the H-cell. Longer time range test also shows repeatable initial current density and the trend over the course of 20 hours.

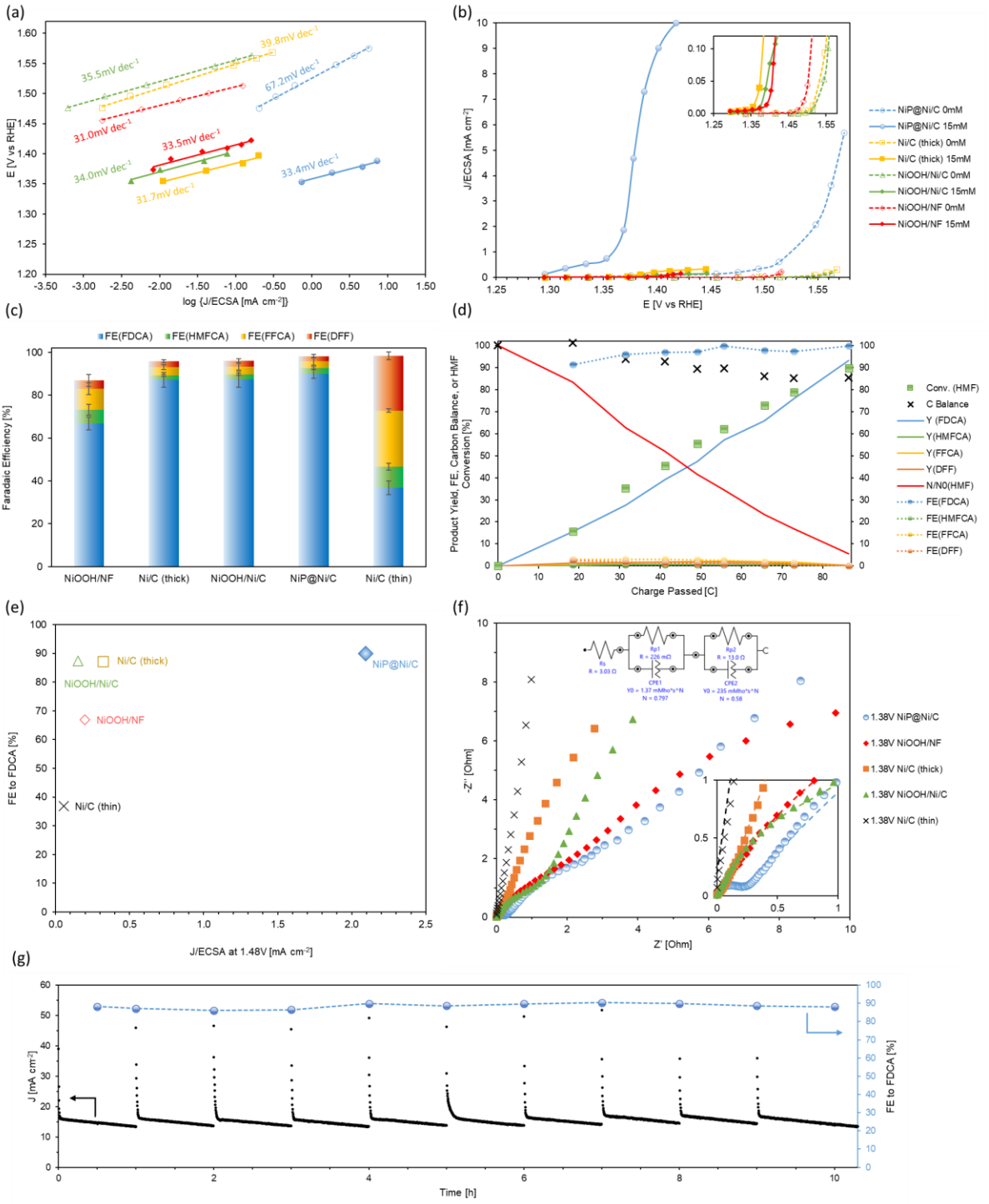

Figure 14 Electrochemical performance of catalysts a) polarization curves in 1 M KOH with and without HMF (iR-corrected); b) Tafel plot in 1 M KOH with and without HMF (iR-corrected); c) Faradaic efficiency of HMFOR at 1.48 V RHE for 30 minutes; d) product yield, faradaic efficiency, and HMF conversion on NiP@NiC during constant potential conversion; e) comparison among catalysts on applied potential and ECSA-normalized current density; f) electrochemical impedance spectroscopy (EIS) in 1 M KOH with 15 mM HMF; g) chronoamperometry stability test in 1 M KOH with 15 mM HMF.

6.1.4. Charge Storing Capability

To investigate further the charge transfer phenomenon on NiP@Ni/C and other control catalysts, spontaneous HMF conversion test under open circuit condition is performed. The anode is first charged at 1.42 V vs RHE in 1M KOH for 10 minutes which is above the oxidation potential for Ni^{2+} but before the OER appears. This renders the surface of catalyst Ni^{3+} enriched, then 5 mM of HMF is added to the anolyte where Ni^{3+}spontaneously discharge into the electrolyte leading to HMF conversion while the drop in the OCP is monitored for 1500 seconds. A trend is shown in Figure 15a on phosphorus-free samples, where thicker Ni layer leads to lower specific charge (50 nm and 200 nm NiOOH/Ni/C with 1.3 C/mg and 0.3 C/mg respectively, NiOOH/NF with only 0.01 C/mg), while Ni-P derived catalysts demonstrate higher values (> 1.7 C/mg). Without addition of HMF, a stable OCP around 1.3 V is reached at equilibrium for all Ni-based catalysts tested above. This supports the hypothesis that only some surface Ni layers get oxidized under Ni^{2+} oxidation potential instead of the whole bulk electrode when there are no other elements or types of bonds present within the bulk. The composition analysis on the catalyst by inductively coupled plasma optical emission spectroscopy (ICP-OES) is used to obtain the phosphorus and nickel amount.

During the OCP test on Ni^{3+} surface with HMF, the potential reading on the anode for the oxidized Ni-P catalyst is maintained at 1.30 V, indicating a sustained high oxidation state for surface Ni species. On the contrary, for other catalysts, despite the support material (carbon paper or nickel foam) and thickness of Ni layer, the OCP quickly drops to around 0.90 V which is the Ni^{2+} equilibrium potential, meaning that the surface layer of Ni^{3+} is not maintained for long. Consequently, the electrolyte sampled at the end of 1500 s of the OCP test, shows the most FDCA selectivity (76%) on the oxidized NiP@Ni/C while for the other catalysts, the amount of HMF conversion to FDCA is greatly limited by the amount of charge being transferred (Figure 15b). At stable OCP, the NiOOH/NF only reaches ~50% charge efficiency but Ni-P passes up to 84% of the stored charge towards FDCA formation. Therefore, the good conductivity of Ni-P catalyst and its charge storing ability enable the continuous facile conversion of alcohol and aldehyde groups on the HMF molecules. This resembles the core-shell effect on some transition metal catalysts with enhanced electrochemical performance that were previously studied [115-117].

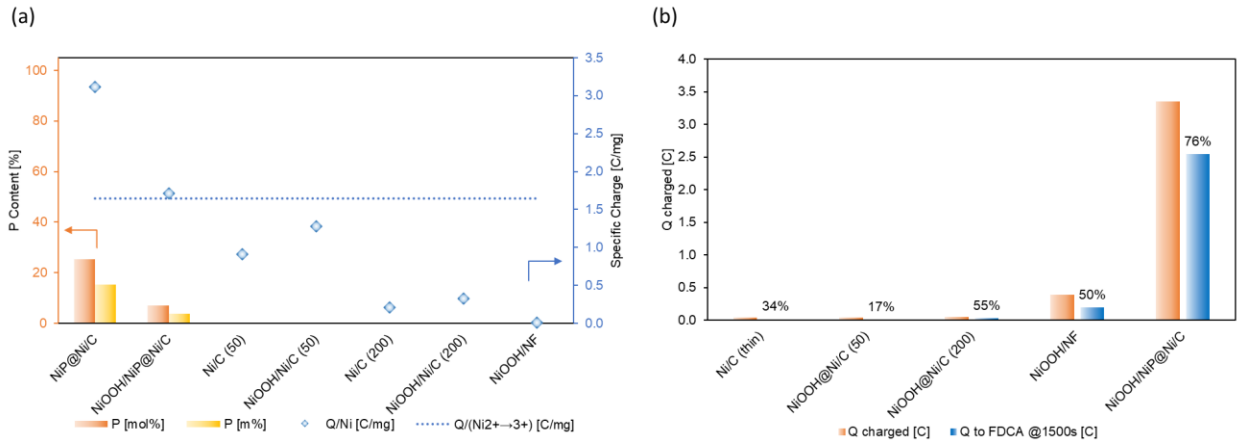

Figure 15 a) Specific charge taken by Ni/C or NiP-derived catalysts with different phosphorous content; b) Charge attained by catalysts during charging stage and charge responsible for FDCA production during discharging stage in OCP test.

In short, we found that Ni-P catalyst is highly active for the HMFOR towards FDCA formation with an excellent oxidation charge storing capacity at low applied potential of 1.42V vs reversible hydrogen electrode (RHE), which is spontaneously reactive with HMF to form the final product FDCA at open circuit condition. The ECSA-normalized current density is superior to other Ni-based catalysts including thin (1-2 nm) and thick (200 nm) Ni-deposited carbon paper (NiC), surface oxidized Ni-deposited carbon paper (NiOOH/Ni/C), and surface oxidized nickel foam (NiOOH/NF). NiP@Ni/C also has the highest Faradaic efficiency compared to the other catalysts, which reaches above 99% at the end of the conversion.

6.2. Combined System

The stage 2 of the thesis work begins with synthesis of NiP on 3D porous carbon felt with 2 nm Ni deposition by Nexdep, denoted as NiP@Ni/CF. This ensures larger number of active sites available for reaction in the anode half-cell. The as-synthesized NiP@Ni/CF (Figure A6) is prepared by the same method as in preparation of NiP@Ni/C with carbon paper, except that the number of LSV scans is 30~50.

To ensure better mass transfer of CO_2 on the cathode, flow-cell reactor is used (Figure 5). On the cathode, a CO_2 gas chamber allows continuous reactant supply, which is essential to the conversion at high current density [106]. An extra chamber is added on the anode to ensure anolyte goes through the porous carbon felt catalyst.

Combined CP tests are done with drop-casted Sn/C and PVD Cu/C, Ag/C catalysts (Figure A2). From preliminary experiments and stage 1 results, it is expected that the CO_2RR performance remains mostly unchanged in product FE, while the anode applied potential drops in the presence of HMF due to the replacement of OER by HMFOR. With Sn/C as the cathode catalyst, as shown in Figure 16, formate (~75%) is the major product in the liquid phase and CO (~9%) is the product in the gas phase. Moreover, Cu/C produces mainly ethanol (~11%) in the liquid phase, and ethylene (~31%) and CO (16~26%) in the gas phase. Taking 1-propanol (3.3%) and acetic acid (1%) into account, it results in at least 45% FE toward C_{2+} products. Finally, Ag/C achieves ~91% of CO production as a robust catalyst. The HMFOR in the anode is consistent with 73~77% FE toward FDCA in the flow-cell, regardless of the cathode reaction (HER on Pt, CO_2RR on Sn/C, Cu/C or Ag/C), as shown in Figure 17. In the NiP//Sn/C combined system, while the cathodic applied potential is around -2.1 V vs. Ag/AgCl at a current density of 100 mA/cm^2, the anodic applied potential decreases from 1.04 V to 0.84 V vs. Ag/AgCl when 15 mM of HMF is added to the anolyte. Similarly, in the NiP//Cu/C system, the cathodic applied potential remains unchanged at -2.0 V vs. Ag/AgCl but the anodic counterpart again encounters a drop of 200 mV when HMFOR replaces OER (Figure 18). As a result of this lowered anodic applied potential, the system energy efficiency is improved 8~9% when HMF is added to the anode in the NiP//Sn/C, NiP//Cu/C, and NiP//Ag/C combined systems, respectively (Table 3). Equations for calculation of FE and EE are shown in Appendices. Experimental results from the combined system have shown that the objective of high selectivity at high current density with improved system energy efficiency is achieved by replacing conventional OER with HMFOR as the anode reaction. This proposed technique in combination with literature results generally gives a predicted improvement in energy efficiency of 8-27% (Table A1).

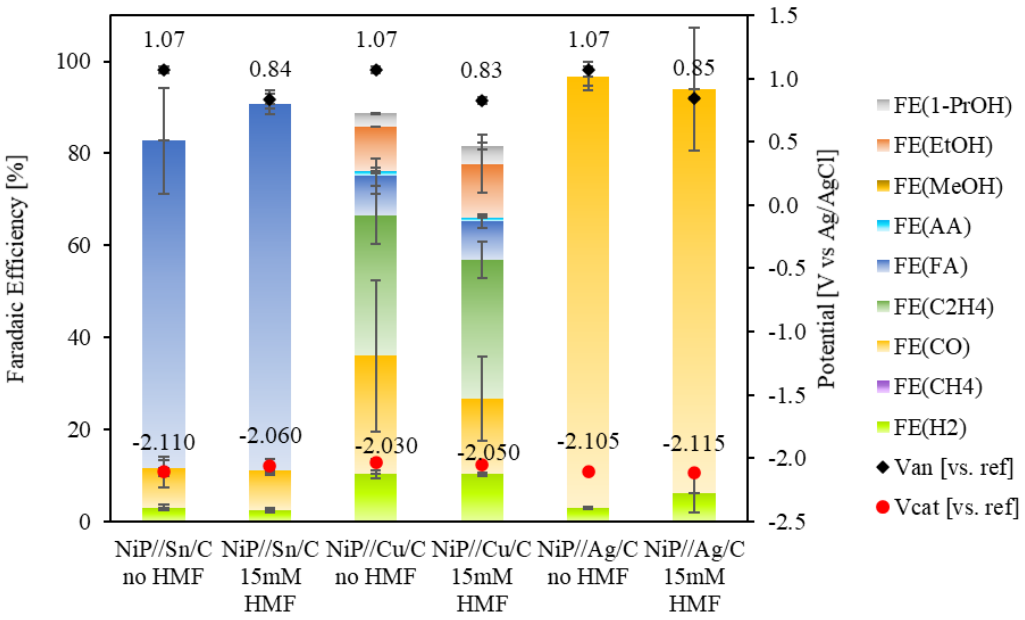

Figure 16 FE summary and half-cell applied potentials of combined CP test at 100 mA/cm^2 with Sn/C or Cu/C as cathode catalyst and NiP@Ni/CF as anode catalyst.

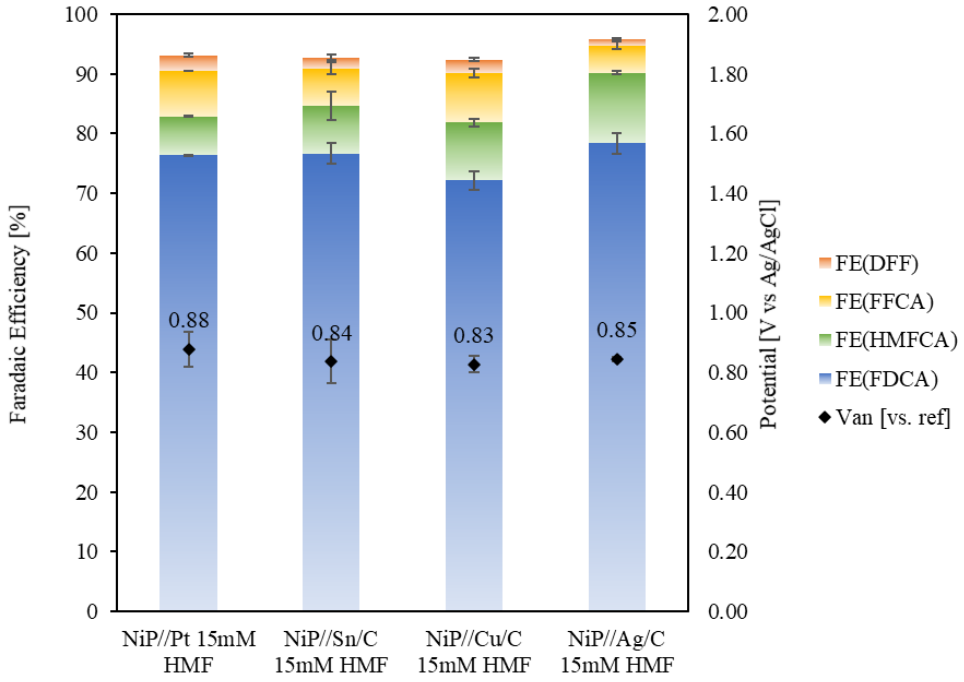

Figure 17 HMFOR FE summary and anode applied potentials of CP tests at 100 mA/cm^2 with NiP@Ni/CF as anode catalyst.

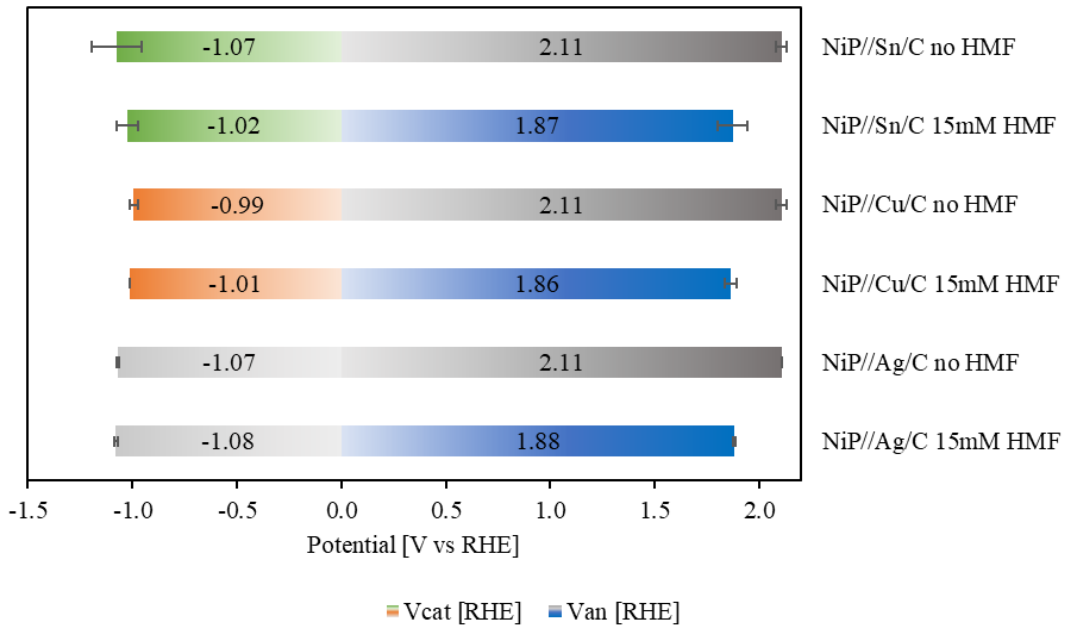

Figure 18 Cathodic and anodic half-cell applied potentials in combined systems with and without HMF added in the anolyte.

Table 3 System energy efficiencies and savings improved by combination of HMFOR with observed cathode FE and potential. Variables followed by the prime symbol indicate the proposed combined system with Ni-P catalyst for HMFOR, same for all following tables. Equations for calculation of FE and EE are shown in Appendices.

Product	Catalyst	Vcat RHE	Van' RHE	EE (%)	EE' (%)	Improv. %
Formate	Sn/C	-1.05	1.87	35.1	38.0	8.22
Formate	Cu/C	-1.00	1.86	4.0	4.3	8.74
Acetate	Cu/C	-1.00	1.86	0.4	0.4	8.74
CO	Cu/C	-1.00	1.86	9.0	9.8	8.74
Ethylene	Cu/C	-1.00	1.86	11.6	12.6	8.74
Ethanol	Cu/C	-1.00	1.86	4.1	4.4	8.74
1-Propanol	Cu/C	-1.00	1.86	1.2	1.3	8.74
CO	Ag/C	-1.07	1.88	38.2	41.2	7.80

6.3. Discussions and Recommendations

In discovering the charge storing effect from the Ni-P catalyst, the HMFOR metrics including ECSA-normalized current density, FE, and overpotential are improved and show beneficial characteristics when electrical energy is intermittent. The novel work done to show the charge and discharge of the Ni-P materials in the electrode gives insight on catalyst design and bulk material analysis for future study.

The successful synthesis and application of the Ni-P catalyst for HMFOR into the combined system with CO_2RR are promising results for improving the electrochemical setup in the future work. The core of the expectation with alternative half-cells replacing OER is to lower the cell applied potential and maintain high performance on both reactions. With the applied current of 100 mA/cm^2, a universal improvement in the system energy efficiency is found using different CO_2RR catalysts. The energy efficiency regarding each product shown in Table 3 is indicative of more room for improvement.

Following the experimental results, theoretical calculations are carried out to emphasize the significance in system optimization for future work. The base case is the currently observed CO_2RR-OER system. It can be seen that in Table 4, if cathode is much improved so that the cathode potential is the same as the standard potential and the faradaic efficiency for the CO_2RR products is 100%, then the new system efficiency combined with the proposed Ni-P catalyst for HMFOR will be mid 60% to 70%, having a 11~14% increase. This means that if the cathode is ideal, the improvement by pairing with HMFOR is relatively similar to the case in non-ideal cathode with respect to each product. However, if anode reaction is ideal for HMFOR (at Ni^{2+} oxidation onset potential, 1.36 V vs. RHE), as shown in Table 5, the relative improvement on the system with the current cathode performance is more than 30%. This indicates the relative importance of anode reaction design. It should be noted that the FE on the cathode side directly and equally affects the cathode and the cell energy efficiencies, so it does not affect the relative improvement. FE is undoubtedly the first field to work on based on its direct effect on the energy efficiency, while finding a suitable anode reaction that significantly lowers extra energy spent on the anode is the next step.

Table 4 System energy efficiencies improved by combination of HMFOR with unity cathode FE at standard potential for each product.

Product	Catalyst	Vcat RHE	Van' RHE	EE (%)	EE' (%)	Improv. %
Formate	Sn/C	-0.25	1.87	62.7	69.8	11.32
Formate	Cu/C	-0.25	1.86	62.7	70.1	11.85
Acetate	Cu/C	0.125	1.86	55.7	63.7	14.41
CO	Cu/C	-0.106	1.86	60.3	68.0	12.72
Ethylene	Cu/C	0.064	1.86	57.0	64.9	13.92
Ethanol	Cu/C	0.084	1.86	56.6	64.5	14.08
1-Propanol	Cu/C	0.095	1.86	56.3	64.3	14.16
CO	Ag/C	-0.106	1.88	60.3	67.3	11.58

Table 5 System energy efficiencies improved by combination of ideal anode reaction with observed cathode FE and potential.

Product	Catalyst	Vcat RHE	Van' RHE	EE (%)	EE' (%)	Improv. %
Formate	Sn/C	-1.05	1.36	35.1	46.1	31.12
Formate	Cu/C	-1.00	1.36	4.0	5.3	31.78
Acetate	Cu/C	-1.00	1.36	0.4	0.5	31.78
CO	Cu/C	-1.00	1.36	9.0	11.9	31.78
Ethylene	Cu/C	-1.00	1.36	11.6	15.3	31.78
Ethanol	Cu/C	-1.00	1.36	4.1	5.3	31.78
1-Propanol	Cu/C	-1.00	1.36	1.2	1.6	31.78
CO	Ag/C	-1.07	1.36	38.2	50.0	30.86

The previous EE analysis has shown improvement to CO_2RR energy efficiency. To illustrate the recommendation for future work, a more stringent parameter is introduced. Similar to the voltage efficiency, dividing the voltage difference between CO_2RR and OER at 100 mA/cm^2 by the improved cell voltage demonstrates a voltage saving (η_V) of the new setup. The applied voltage for conventional CO_2RR-OER is the base case and is used as the nominator for the voltage factor term, whereas the improved applied voltage is in the denominator. Then this result is multiplied by the FE of both cathode and anode reactions to get the full cell energy saving factor η_{cell}. A near-unity result indicates no significant energy saving for the full cell, while a larger

number refers to a considerable saving from the energetic perspective. If the FE of one side is too low, η_{cell} will end up as a relatively small number, indicating a low benefit for simultaneous production. The numeric value of this energy saving factor η_{cell} and the relative improvement are summarized in Table 6. Although these tests all show a relatively small improvement, the formate production by Sn/C and the CO production by Ag/C have the highest η_{cell}, given their robust cathodic FE. Cu/C on the contrary suffers from the low FE for multiple products. When combining with the Ni-P, even with >90% HMFOR FE, the results are still below 1 for all the tests. Beside the cathode FE, the rather small improvement from all the combined tests from the experiment indicates that further advancement at the anodic half-cell is needed. It should be noticed that the conventional OER has by default 100% FE, so the only way in increasing the energy saving via the anode is to further lower the applied anode potential. Since HMFOR is active after Ni^{3+} is present (1.36 V vs. RHE), the theoretical maximum η_{cell} for CO_2RR-HMFOR system via Ni-based catalysts will be 1.5~1.6, which is close to the theoretical ideal η_{cell} (1.6~1.8) for CO_2RR-OER system (Van = 1.23 V vs. RHE), shown in Table 7. This leads to the understanding that developing a better catalyst for HMFOR at lower applied potential is the key to increasing the energy saving for the coupled CO_2RR-HMFOR system. Although the energetic analysis outcome is not completely satisfying, one should also consider the economic benefits of HMFOR. According to our most recent study of techno-economic analysis on HMFOR, it is economically advantageous to produce FDCA at a mild current density (30~40 mA/cm^2) with low applied potential (<1.7 V) and a similar FE (90%) [118]. Alternatively, designing another efficient biowaste anode half-cell which enables the same current density at even lower potential could also improve the full cell energy saving.

Table 6 System energy saving factors comparison between CO_2RR-OER and CO_2RR-HMFOR with observed cathode FE and potential.

Product	**Catalyst**	**Vcat RHE**	**Vcat FE**	**Van RHE**	**Van' RHE**	**Van' FE**	**ηv'**	**ηcell'**	**Improv. %**
Formate	Sn/C	-1.05	75	2.11	1.87	93	1.08	0.75	0.33
Formate	Cu/C	-1.00	8.4	2.11	1.86	92	1.09	0.08	0.43
Acetate	Cu/C	-1.00	1	2.11	1.86	92	1.09	0.01	0.43
CO	Cu/C	-1.00	21	2.11	1.86	92	1.09	0.21	0.43

Ethylene	Cu/C	-1.00	31	2.11	1.86	92	1.09	0.31	0.43
Ethanol	Cu/C	-1.00	11	2.11	1.86	92	1.09	0.11	0.43
1-Propanol	Cu/C	-1.00	3.3	2.11	1.86	92	1.09	0.03	0.43
CO	Ag/C	-1.07	91	2.11	1.88	96	1.08	0.94	3.31

Table 7 System energy saving factors comparison between ideal CO_2RR-OER and ideal CO_2RR-HMFOR with unity cathode FE at standard potential.

Product	**Catalyst**	**Vcat RHE**	**Vcat FE**	**Van RHE**	**Van' RHE**	**Van' FE**	**ηcell**	**ηcell'**	**Improv. %**
Formate	Sn/C	-0.25	100	1.23	1.36	100	1.59	1.47	0.33
Formate	Cu/C	-0.25	100	1.23	1.36	100	1.59	1.47	0.43
Acetate	Cu/C	0.125	100	1.23	1.36	100	1.80	1.61	0.43
CO	Cu/C	-0.106	100	1.23	1.36	100	1.66	1.51	0.43
Ethylene	Cu/C	0.064	100	1.23	1.36	100	1.75	1.58	0.43
Ethanol	Cu/C	0.084	100	1.23	1.36	100	1.77	1.59	0.43
1-Propanol	Cu/C	0.095	100	1.23	1.36	100	1.78	1.59	0.43
CO	Ag/C	-0.106	100	1.23	1.36	100	1.66	1.51	3.31

7. Conclusions

CO_2 reduction reaction, or CO_2RR, is a promising candidate to realize a carbon utilization processing via clean energy source such as renewable electricity. The main challenge in this process being the high applied potential at high current density is tackled by replacing the conventional oxygen evolution reaction with an efficient and less energy demanding HMF oxidation reaction. The first stage in this thesis work includes development of efficient home-made catalysts. Ni-based P-doped catalyst with carbon substrate is synthesized and tested, with high Faradaic efficiency toward FDCA (90%) and stability (> 20 h) achieved at low applied potential (1.48 V RHE). Specifically, sublayer catalytic activity in the form of charge storing capacity is studied and considered to be a novel approach to catalytic material synthesis. In the second stage of the work, Ni-P catalyst is synthesized with 3D carbon substrate, allowing the effective combination with CO_2RR while keeping the HMFOR FE above 95% at high current density of 100 mA/cm^2 and low anode applied potential (1.83 V RHE). Most importantly, by pairing with Sn nanoparticles in the cathode, 75% FE toward formic acid is achieved; on the other hand, by combining with Cu and Ag catalysts, 45% FE toward C_{2+} products and 91% FE for CO production are achieved with up to 9% increase in energy efficiency and 3% growth in a more critical full cell energy saving. In summary, improvement in electrochemical conversion of CO_2 to useful chemicals and renewable fuels is realized with innovative approach replacing OER with HMFOR. Future recommendations will be to improve CO_2RR selectivity and finding other useful anode reactions for coupling.

References

1. Kibria, M.G., et al., *Electrochemical CO2 Reduction into Chemical Feedstocks: From Mechanistic Electrocatalysis Models to System Design.* Adv Mater, 2019. **31**(31): p. e1807166.
2. Zhang, F., H. Zhang, and Z. Liu, *Recent advances in electrochemical reduction of CO2.* Current Opinion in Green and Sustainable Chemistry, 2019. **16**: p. 77-84.
3. Rosen, B.A., et al., *Ionic Liquid–Mediated Selective Conversion of CO₂ to CO at Low Overpotentials.* Science, 2011. **334**(6056): p. 643-644.
4. García de Arquer, F.P., et al., *CO2 electrolysis to multicarbon products at activities greater than 1 A cm−2.* Science, 2020. **367**(6478): p. 661-666.
5. Ma, S., et al., *Carbon Foam Decorated with Silver Nanoparticles for Electrochemical CO2 Conversion.* Energy Technology, 2017. **5**(6): p. 861-863.
6. Sivanesan, D., et al., *Hydrogenation of CO2 to formate using a tripodal-based nickel catalyst under basic conditions.* Catalysis Communications, 2019. **120**: p. 66-71.
7. Muraza, O. and A. Galadima, *A review on coke management during dry reforming of methane.* International Journal of Energy Research, 2015. **39**(9): p. 1196-1216.
8. Galadima, A. and O. Muraza, *Catalytic thermal conversion of CO2 into fuels: Perspective and challenges.* Renewable and Sustainable Energy Reviews, 2019. **115**: p. 109333.
9. Ma, J., et al., *Hydrogenation of CO2 to formic acid on the single atom catalysis Cu/C2N: A first principles study.* Applied Surface Science, 2019. **488**: p. 1-9.
10. Cai, M., et al., *Methanation of carbon dioxide on Ni/ZrO2-Al2O3 catalysts: Effects of ZrO2 promoter and preparation method of novel ZrO2-Al2O3 carrier.* Journal of Natural Gas Chemistry, 2011. **20**(3): p. 318-324.
11. Rao, H., et al., *Visible-Light-Driven Conversion of CO2 to CH4 with an Organic Sensitizer and an Iron Porphyrin Catalyst.* Journal of the American Chemical Society, 2018. **140**(51): p. 17830-17834.
12. Lang, P., et al., *Sensitized Photochemical CO2 Reduction by Hetero-Pacman Compounds Linking a ReI Tricarbonyl with a Porphyrin Unit.* Chemistry – A European Journal, 2019. **25**(17): p. 4509-4519.
13. Kuramochi, Y., Y. Fujisawa, and A. Satake, *Photocatalytic CO2 Reduction Mediated by Electron Transfer via the Excited Triplet State of Zn(II) Porphyrin.* Journal of the American Chemical Society, 2020. **142**(2): p. 705-709.
14. Kuramochi, Y., O. Ishitani, and H. Ishida, *Reaction mechanisms of catalytic photochemical CO2 reduction using Re(I) and Ru(II) complexes.* Coordination Chemistry Reviews, 2018. **373**: p. 333-356.
15. Kumar, B., et al., *Photochemical and Photoelectrochemical Reduction of CO2.* Annual Review of Physical Chemistry, 2012. **63**(1): p. 541-569.
16. Szaniawska, E., et al., *Reduction of carbon dioxide at copper(I) oxide photocathode activated and stabilized by over-coating with oligoaniline.* Electrochimica Acta, 2018. **265**: p. 400-410.
17. Perini, J.A.L., et al., *Ag/polydopamine-modified Ti/TiO2 nanotube arrays: A platform for enhanced CO2 photoelectroreduction to methanol.* Journal of CO2 Utilization, 2019. **34**: p. 596-605.

18. Kumaravel, V., J. Bartlett, and S.C. Pillai, *Photoelectrochemical Conversion of Carbon Dioxide (CO2) into Fuels and Value-Added Products.* ACS Energy Letters, 2020: p. 486-519.
19. Kamata, R., et al., *Photoelectrochemical CO2 Reduction Using a Ru(II)–Re(I) Supramolecular Photocatalyst Connected to a Vinyl Polymer on a NiO Electrode.* ACS Applied Materials & Interfaces, 2019. **11**(6): p. 5632-5641.
20. Bachmeier, A., et al., *How Light-Harvesting Semiconductors Can Alter the Bias of Reversible Electrocatalysts in Favor of H2 Production and CO2 Reduction.* Journal of the American Chemical Society, 2013. **135**(40): p. 15026-15032.
21. Yang, Z.-Y., et al., *Carbon dioxide reduction to methane and coupling with acetylene to form propylene catalyzed by remodeled nitrogenase.* Proceedings of the National Academy of Sciences, 2012. **109**(48): p. 19644-19648.
22. Xu, S.-w., et al., *Efficient Conversion of CO2 to Methanol Catalyzed by Three Dehydrogenases Co-encapsulated in an Alginate−Silica (ALG−SiO2) Hybrid Gel.* Industrial & Engineering Chemistry Research, 2006. **45**(13): p. 4567-4573.
23. Shin, W., et al., *Highly Selective Electrocatalytic Conversion of CO2 to CO at −0.57 V (NHE) by Carbon Monoxide Dehydrogenase from Moorella thermoacetica.* Journal of the American Chemical Society, 2003. **125**(48): p. 14688-14689.
24. Shi, J., et al., *Enzymatic conversion of carbon dioxide.* Chemical Society Reviews, 2015. **44**(17): p. 5981-6000.
25. Barin, R., et al., *Enzymatic CO2 reduction to formate by formate dehydrogenase from Candida boidinii coupling with direct electrochemical regeneration of NADH.* Journal of CO2 Utilization, 2018. **28**: p. 117-125.
26. Wang, W., et al., *Modeling Plasma-based CO2 and CH4 Conversion in Mixtures with N2, O2, and H2O: The Bigger Plasma Chemistry Picture.* The Journal of Physical Chemistry C, 2018. **122**(16): p. 8704-8723.
27. Wang, L., et al., *Atmospheric Pressure and Room Temperature Synthesis of Methanol through Plasma-Catalytic Hydrogenation of CO2.* ACS Catalysis, 2018. **8**(1): p. 90-100.
28. Barnhart, C.J., et al., *The energetic implications of curtailing versus storing solar- and wind-generated electricity.* Energy & Environmental Science, 2013. **6**(10): p. 2804-2810.
29. Whipple, D.T. and P.J.A. Kenis, *Prospects of CO2 Utilization via Direct Heterogeneous Electrochemical Reduction.* The Journal of Physical Chemistry Letters, 2010. **1**(24): p. 3451-3458.
30. Pearson, P.J.G. and T.J. Foxon, *A low carbon industrial revolution? Insights and challenges from past technological and economic transformations.* Energy Policy, 2012. **50**: p. 117-127.
31. Gabardo, C.M., et al., *Combined high alkalinity and pressurization enable efficient CO2 electroreduction to CO.* Energy & Environmental Science, 2018. **11**(9): p. 2531-2539.
32. Arán-Ais, R.M., D. Gao, and B. Roldan Cuenya, *Structure- and Electrolyte-Sensitivity in CO2 Electroreduction.* Accounts of Chemical Research, 2018. **51**(11): p. 2906-2917.
33. Ahn, S.T., I. Abu-Baker, and G.T.R. Palmore, *Electroreduction of CO2 on polycrystalline copper: Effect of temperature on product selectivity.* Catalysis Today, 2017. **288**: p. 24-29.
34. Weekes, D.M., et al., *Electrolytic CO2 Reduction in a Flow Cell.* Accounts of Chemical Research, 2018. **51**(4): p. 910-918.
35. Na, J., et al., *General technoeconomic analysis for electrochemical coproduction coupling carbon dioxide reduction with organic oxidation.* Nat Commun, 2019. **10**(1): p. 5193.

36. You, B., et al., *Simultaneous H2 Generation and Biomass Upgrading in Water by an Efficient Noble-Metal-Free Bifunctional Electrocatalyst.* Angewandte Chemie International Edition, 2016. **55**(34): p. 9913-9917.
37. Oliveira, V.L., et al., *Kinetic Investigations of Glycerol Oxidation Reaction on Ni/C.* Electrocatalysis, 2015. **6**(5): p. 447-454.
38. You, B., et al., *A General Strategy for Decoupled Hydrogen Production from Water Splitting by Integrating Oxidative Biomass Valorization.* Journal of the American Chemical Society, 2016. **138**(41): p. 13639-13646.
39. Oliveira, V.L., et al., *Studies of the reaction products resulted from glycerol electrooxidation on Ni-based materials in alkaline medium.* Electrochimica Acta, 2014. **117**: p. 255-262.
40. Simoska, O., et al., *Advances in Electrochemical Modification Strategies of 5-Hydroxymethylfurfural.* ChemSusChem, 2021. **14**(7): p. 1674-1686.
41. Giannakoudakis, D.A., et al., *Nanoengineered Electrodes for Biomass-Derived 5-Hydroxymethylfurfural Electrocatalytic Oxidation to 2,5-Furandicarboxylic Acid.* ACS Sustainable Chemistry & Engineering, 2021. **9**(5): p. 1970-1993.
42. Teeter, T.E. and P.V. Rysselberghe, *Reduction of Carbon Dioxide on Mercury Cathodes.* The Journal of Chemical Physics, 1954. **22**(4): p. 759-760.
43. Haynes, L.V. and D.T. Sawyer, *Electrochemistry of carbon dioxide in dimethyl sulfoxide at gold and mercury electrodes.* Analytical Chemistry, 1967. **39**(3): p. 332-338.
44. Kaiser, U. and E. Heitz, *Zum Mechanismus der elektrochemischen Dimerisierung von CO2 zu Oxalsäure.* Berichte der Bunsengesellschaft für physikalische Chemie, 1973. **77**(10‐11): p. 818-823.
45. Amatore, C. and J.M. Saveant, *Mechanism and kinetic characteristics of the electrochemical reduction of carbon dioxide in media of low proton availability.* Journal of the American Chemical Society, 1981. **103**(17): p. 5021-5023.
46. Hori, Y. and S. Suzuki, *Electrolytic Reduction of Carbon Dioxide at Mercury Electrode in Aqueous Solution.* Bulletin of the Chemical Society of Japan, 1982. **55**(3): p. 660-665.
47. Lin, R., et al., *Electrochemical Reactors for CO2 Conversion.* Catalysts, 2020. **10**(5).
48. Zhao, S., R. Jin, and R. Jin, *Opportunities and Challenges in CO2 Reduction by Gold- and Silver-Based Electrocatalysts: From Bulk Metals to Nanoparticles and Atomically Precise Nanoclusters.* ACS Energy Letters, 2018. **3**(2): p. 452-462.
49. Chen, Y., et al., *Identifying Active Sites for CO2 Reduction on Dealloyed Gold Surfaces by Combining Machine Learning with Multiscale Simulations.* J Am Chem Soc, 2019. **141**(29): p. 11651-11657.
50. Jeanty, P., et al., *Upscaling and continuous operation of electrochemical CO2 to CO conversion in aqueous solutions on silver gas diffusion electrodes.* Journal of CO2 Utilization, 2018. **24**: p. 454-462.
51. Lee, C.W., et al., *Selective Electrochemical Production of Formate from Carbon Dioxide with Bismuth-Based Catalysts in an Aqueous Electrolyte.* ACS Catalysis, 2018. **8**(2): p. 931-937.
52. Su, P., et al., *Ultrathin Bismuth Nanosheets as a Highly Efficient CO2 Reduction Electrocatalyst.* ChemSusChem, 2018. **11**(5): p. 848-853.
53. Jia, L., et al., *Copper-Bismuth Bimetallic Microspheres for Selective Electrocatalytic Reduction of CO2 to Formate.* Chinese Journal of Chemistry, 2019. **37**(5): p. 497-500.

54. Choi, S.Y., et al., *Electrochemical Reduction of Carbon Dioxide to Formate on Tin–Lead Alloys.* ACS Sustainable Chemistry & Engineering, 2016. **4**(3): p. 1311-1318.
55. Zheng, X., et al., *Theory-guided Sn/Cu alloying for efficient CO2 electroreduction at low overpotentials.* Nature Catalysis, 2019. **2**(1): p. 55-61.
56. Sun, K., et al., *Ultrahigh Mass Activity for Carbon Dioxide Reduction Enabled by Gold-Iron Core-Shell Nanoparticles.* J Am Chem Soc, 2017. **139**(44): p. 15608-15611.
57. Genovese, C., et al., *Electrocatalytic conversion of CO2 on carbon nanotube-based electrodes for producing solar fuels.* Journal of Catalysis, 2013. **308**: p. 237-249.
58. Ampelli, C., et al., *CO2 capture and reduction to liquid fuels in a novel electrochemical setup by using metal-doped conjugated microporous polymers.* Journal of Applied Electrochemistry, 2015. **45**(7): p. 701-713.
59. Wang, R., et al., *Maximizing Ag Utilization in High-Rate CO2 Electrochemical Reduction with a Coordination Polymer-Mediated Gas Diffusion Electrode.* ACS Energy Letters, 2019. **4**(8): p. 2024-2031.
60. Albo, J., et al., *Copper-Based Metal–Organic Porous Materials for CO2 Electrocatalytic Reduction to Alcohols.* ChemSusChem, 2017. **10**(6): p. 1100-1109.
61. Duan, X., et al., *Metal-Free Carbon Materials for CO2 Electrochemical Reduction.* Advanced Materials, 2017. **29**(41): p. 1701784.
62. Wu, J., et al., *A metal-free electrocatalyst for carbon dioxide reduction to multi-carbon hydrocarbons and oxygenates.* Nature Communications, 2016. **7**(1): p. 13869.
63. Liu, Y., et al., *Selective Electrochemical Reduction of Carbon Dioxide to Ethanol on a Boron- and Nitrogen-Co-doped Nanodiamond.* Angewandte Chemie International Edition, 2017. **56**(49): p. 15607-15611.
64. Liu, Y., et al., *Efficient Electrochemical Reduction of Carbon Dioxide to Acetate on Nitrogen-Doped Nanodiamond.* Journal of the American Chemical Society, 2015. **137**(36): p. 11631-11636.
65. Zhang, W., et al., *Progress and Perspective of Electrocatalytic CO2 Reduction for Renewable Carbonaceous Fuels and Chemicals.* Advanced Science, 2018. **5**(1): p. 1700275.
66. Qiao, J., et al., *A review of catalysts for the electroreduction of carbon dioxide to produce low-carbon fuels.* Chemical Society Reviews, 2014. **43**(2): p. 631-675.
67. Zhu, Q., et al., *Carbon dioxide electroreduction to C2 products over copper-cuprous oxide derived from electrosynthesized copper complex.* Nat Commun, 2019. **10**(1): p. 3851.
68. Jouny, M., W. Luc, and F. Jiao, *General Techno-Economic Analysis of CO2 Electrolysis Systems.* Industrial & Engineering Chemistry Research, 2018. **57**(6): p. 2165-2177.
69. Man, I.C., et al., *Universality in Oxygen Evolution Electrocatalysis on Oxide Surfaces.* ChemCatChem, 2011. **3**(7): p. 1159-1165.
70. Ma, S., et al., *Efficient Electrochemical Flow System with Improved Anode for the Conversion of CO2to CO.* Journal of The Electrochemical Society, 2014. **161**(10): p. F1124-F1131.
71. McCrory, C.C.L., et al., *Benchmarking Heterogeneous Electrocatalysts for the Oxygen Evolution Reaction.* Journal of the American Chemical Society, 2013. **135**(45): p. 16977-16987.
72. McCrory, C.C.L., et al., *Benchmarking Hydrogen Evolving Reaction and Oxygen Evolving Reaction Electrocatalysts for Solar Water Splitting Devices.* Journal of the American Chemical Society, 2015. **137**(13): p. 4347-4357.

73. Lhermitte, C.R. and K. Sivula, *Alternative Oxidation Reactions for Solar-Driven Fuel Production.* ACS Catalysis, 2019. **9**(3): p. 2007-2017.
74. Liang, H., et al., *Hydrothermal Continuous Flow Synthesis and Exfoliation of NiCo Layered Double Hydroxide Nanosheets for Enhanced Oxygen Evolution Catalysis.* Nano Letters, 2015. **15**(2): p. 1421-1427.
75. Yuan, W., et al., *Interfacial Engineering of Cobalt Nitrides and Mesoporous Nitrogen-Doped Carbon: Toward Efficient Overall Water-Splitting Activity with Enhanced Charge-Transfer Efficiency.* ACS Energy Letters, 2020. **5**(3): p. 692-700.
76. Bozell, J.J. and G.R. Petersen, *Technology development for the production of biobased products from biorefinery carbohydrates—the US Department of Energy's "Top 10" revisited.* Green Chemistry, 2010. **12**(4): p. 539-554.
77. van Putten, R.J., et al., *Hydroxymethylfurfural, a versatile platform chemical made from renewable resources.* Chem Rev, 2013. **113**(3): p. 1499-597.
78. Cha, H.G. and K.S. Choi, *Combined biomass valorization and hydrogen production in a photoelectrochemical cell.* Nat Chem, 2015. **7**(4): p. 328-33.
79. Li, K. and Y. Sun, *Electrocatalytic Upgrading of Biomass-Derived Intermediate Compounds to Value-Added Products.* Chemistry, 2018. **24**(69): p. 18258-18270.
80. Verdeguer, P., N. Merat, and A. Gaset, *Oxydation catalytique du HMF en acide 2,5-furane dicarboxylique.* Journal of Molecular Catalysis, 1993. **85**(3): p. 327-344.
81. Latsuzbaia, R., et al., *Continuous electrochemical oxidation of biomass derived 5-(hydroxymethyl)furfural into 2,5-furandicarboxylic acid.* Journal of Applied Electrochemistry, 2018. **48**(6): p. 611-626.
82. Kang, M.J., et al., *Electrocatalysis of 5-hydroxymethylfurfural at cobalt based spinel catalysts with filamentous nanoarchitecture in alkaline media.* Applied Catalysis B: Environmental, 2019. **242**: p. 85-91.
83. Liao, Y.-T., et al., *Engineering a homogeneous alloy-oxide interface derived from metal-organic frameworks for selective oxidation of 5-hydroxymethylfurfural to 2, 5-furandicarboxylic acid.* Applied Catalysis B-Environmental, 2020. **270**.
84. Nam, D.-H., B.J. Taitt, and K.-S. Choi, *Copper-Based Catalytic Anodes To Produce 2,5-Furandicarboxylic Acid, a Biomass-Derived Alternative to Terephthalic Acid.* ACS Catalysis, 2018. **8**(2): p. 1197-1206.
85. Zhang, M., et al., *Trimetallic NiCoFe-Layered Double Hydroxides Nanosheets Efficient for Oxygen Evolution and Highly Selective Oxidation of Biomass-Derived 5-Hydroxymethylfurfural.* ACS Catalysis, 2020. **10**(9): p. 5179-5189.
86. Deng, X., et al., *Constructing multifunctional 'Nanoplatelet-on-Nanoarray' electrocatalyst with unprecedented activity towards novel selective organic oxidation reactions to boost hydrogen production.* Applied Catalysis B-Environmental, 2020. **278**.
87. Song, Y., et al., *Ultrathin layered double hydroxides nanosheets array towards efficient electrooxidation of 5-hydroxymethylfurfural coupled with hydrogen generation.* Applied Catalysis B: Environmental, 2021. **299**.
88. Grill, J.M., J.W. Ogle, and S.A. Miller, *An Efficient and Practical System for the Catalytic Oxidation of Alcohols, Aldehydes, and α,β-Unsaturated Carboxylic Acids.* The Journal of Organic Chemistry, 2006. **71**(25): p. 9291-9296.
89. Grabowski, G., J. Lewkowski, and R. Skowroński, *The electrochemical oxidation of 5-hydroxymethylfurfural with the nickel oxide/hydroxide electrode.* Electrochimica Acta, 1991. **36**(13): p. 1995.

90. Liu, W.-J., et al., *Electrochemical Oxidation of 5-Hydroxymethylfurfural with NiFe Layered Double Hydroxide (LDH) Nanosheet Catalysts.* ACS Catalysis, 2018. **8**(6): p. 5533-5541.
91. Barwe, S., et al., *Electrocatalytic Oxidation of 5-(Hydroxymethyl)furfural Using High-Surface-Area Nickel Boride.* Angewandte Chemie International Edition, 2018. **57**(35): p. 11460-11464.
92. Jiang, N., et al., *Electrocatalysis of Furfural Oxidation Coupled with H2 Evolution via Nickel-Based Electrocatalysts in Water.* ChemNanoMat, 2017. **3**(7): p. 491-495.
93. Taitt, B.J., D.-H. Nam, and K.-S. Choi, *A Comparative Study of Nickel, Cobalt, and Iron Oxyhydroxide Anodes for the Electrochemical Oxidation of 5-Hydroxymethylfurfural to 2,5-Furandicarboxylic Acid.* ACS Catalysis, 2018. **9**(1): p. 660-670.
94. Gao, T., et al., *Co3O4 NPs decorated Mn-Co-O solid solution as highly selective catalyst for aerobic base-free oxidation of 5-HMF to 2,5-FDCA in water.* Catalysis Today, 2019.
95. Jiang, N., et al., *Integrating Electrocatalytic 5-Hydroxymethylfurfural Oxidation and Hydrogen Production via Co–P-Derived Electrocatalysts.* ACS Energy Letters, 2016. **1**(2): p. 386-390.
96. Louie, M.W. and A.T. Bell, *An investigation of thin-film Ni-Fe oxide catalysts for the electrochemical evolution of oxygen.* J Am Chem Soc, 2013. **135**(33): p. 12329-37.
97. Yang, Y., et al., *Efficient Electrocatalytic Oxygen Evolution on Amorphous Nickel–Cobalt Binary Oxide Nanoporous Layers.* ACS Nano, 2014. **8**(9): p. 9518-9523.
98. Li, Y., P. Hasin, and Y. Wu, *Ni(x)Co(3-x)O(4) nanowire arrays for electrocatalytic oxygen evolution.* Adv Mater, 2010. **22**(17): p. 1926-9.
99. Bayatsarmadi, B., et al., *Highly active nickel–cobalt/nanocarbon thin films as efficient water splitting electrodes.* Nanoscale, 2016. **8**(43): p. 18507-18515.
100. Jiang, J., et al., *Nickel–cobalt layered double hydroxide nanosheets as high-performance electrocatalyst for oxygen evolution reaction.* Journal of Power Sources, 2015. **278**: p. 445-451.
101. You, B., et al., *Hierarchically Porous Urchin-Like Ni2P Superstructures Supported on Nickel Foam as Efficient Bifunctional Electrocatalysts for Overall Water Splitting.* ACS Catalysis, 2016. **6**(2): p. 714-721.
102. You, B., et al., *Efficient H2 Evolution Coupled with Oxidative Refining of Alcohols via A Hierarchically Porous Nickel Bifunctional Electrocatalyst.* ACS Catalysis, 2017. **7**(7): p. 4564-4570.
103. Zhang, N., et al., *Electrochemical Oxidation of 5-Hydroxymethylfurfural on Nickel Nitride/Carbon Nanosheets: Reaction Pathway Determined by In Situ Sum Frequency Generation Vibrational Spectroscopy.* Angewandte Chemie International Edition, 2019. **58**(44): p. 15895-15903.
104. Verma, S., et al., *A Gross-Margin Model for Defining Technoeconomic Benchmarks in the Electroreduction of CO2.* ChemSusChem, 2016. **9**(15): p. 1972-9.
105. Orella, M.J., et al., *A General Technoeconomic Model for Evaluating Emerging Electrolytic Processes.* Energy Technology, 2019. **n/a**(n/a): p. 1900994.
106. Burdyny, T. and W.A. Smith, *CO2 reduction on gas-diffusion electrodes and why catalytic performance must be assessed at commercially-relevant conditions.* Energy & Environmental Science, 2019. **12**(5): p. 1442-1453.
107. Cai, W., et al., *Amorphous Multimetal Alloy Oxygen Evolving Catalysts.* ACS Materials Letters, 2020. **2**(6): p. 624-632.

108. Du, F., et al., *Electrodeposited amorphous cobalt phosphosulfide on Ni foams for highly efficient overall water splitting.* Journal of Power Sources, 2019. **431**: p. 182-188.
109. Li, H., et al., *XPS studies on surface electronic characteristics of Ni–B and Ni–P amorphous alloy and its correlation to their catalytic properties.* Applied Surface Science, 1999. **152**(1): p. 25-34.
110. Wang, K., et al., *Efficient and stable Ni–Co–Fe–P nanosheet arrays on Ni foam for alkaline and neutral hydrogen evolution.* International Journal of Hydrogen Energy, 2020. **45**(4): p. 2504-2512.
111. Heidary, N. and N. Kornienko, *Electrochemical biomass valorization on gold-metal oxide nanoscale heterojunctions enables investigation of both catalyst and reaction dynamics with operando surface-enhanced Raman spectroscopy.* Chemical Science, 2020. **11**(7): p. 1798-1806.
112. Song, X., et al., *Improved Performance of Nickel Boride by Phosphorus Doping as an Efficient Electrocatalyst for the Oxidation of 5-Hydroxymethylfurfural to 2,5-Furandicarboxylic Acid.* Industrial & Engineering Chemistry Research, 2020. **59**(39): p. 17348-17356.
113. Bender, M.T., et al., *Unraveling Two Pathways for Electrochemical Alcohol and Aldehyde Oxidation on NiOOH.* J Am Chem Soc, 2020. **142**(51): p. 21538-21547.
114. Weidner, J., et al., *Cobalt-metalloid alloys for electrochemical oxidation of 5-hydroxymethylfurfural as an alternative anode reaction in lieu of oxygen evolution during water splitting.* Beilstein J Org Chem, 2018. **14**: p. 1436-1445.
115. Stern, L.-A., et al., *Ni2P as a Janus catalyst for water splitting: the oxygen evolution activity of Ni2P nanoparticles.* Energy & Environmental Science, 2015. **8**(8): p. 2347-2351.
116. Liu, X., et al., *Hierarchical NiCo2O4@NiCo2O4 core/shell nanoflake arrays as high-performance supercapacitor materials.* ACS Appl Mater Interfaces, 2013. **5**(17): p. 8790-5.
117. Gao, L., et al., *NiSe@NiOx core-shell nanowires as a non-precious electrocatalyst for upgrading 5-hydroxymethylfurfural into 2,5-furandicarboxylic acid.* Applied Catalysis B-Environmental, 2020. **261**.
118. Patel, P., et al., *Technoeconomic and Life-Cycle Assessment for Electrocatalytic Production of Furandicarboxylic Acid.* ACS Sustainable Chemistry & Engineering, 2022.
119. *Stutts, K. (1983). Preparation of nickel-oxide hydroxide electrode. US4462875A.*
120. Liu, Y., et al., *Active Oxygen Species Promoted Catalytic Oxidation of 5-Hydroxymethyl-2-furfural on Facet-Specific Pt Nanocrystals.* ACS Catalysis, 2019. **9**(9): p. 8306-8315.
121. Qiao, J., Y. Liu, and J. Zhang, *Electrochemical reduction of carbon dioxide : fundamentals and technologies*. Electrochemical energy storage and conversion. 2016, Boca Raton: CRC Press, Taylor & Francis Group.
122. Bard, A.J. and L.R. Faulkner, *Electrochemical Methods: Fundamentals and Applications*, ed. D. Harris. 2000: Wiley.

List of Supporting Figures

1. Appendices

1.1. Electrolyzer Architecture

Common types of electrolyzer are undivided cell, H-cell, flow-cell and microfluidic cell. In this thesis work, the two types of electrolyzer used are H-cell and flow-cell. In the first stage of experiment, H-cell (Figure 4) is used to examine activity of the anode HMFOR catalyst. In the second stage, due to mass transfer limitation of dissolved CO_2 in the electrolyte, flow-cell (Figure 5) is used instead. Both types of cells have a membrane that divides the cathode and anode chambers.

1.1.1. H-Cell Architecture

H-cells are commonly used to carry out electrocatalytic experiment because of its facile assembling and easy operation. Two half-cells are connected with a polymer electrolyte membrane in between for selective ion conduction. A Fumasep® FAA-3-PK-75 is used as the anion exchange membrane (AEM), which can pass only negatively charged OH^- ions and water molecule to balance the charge transportation required by both electrodes in alkaline conditions. 1 M KOH solution prepared from pallets (85%, Sigma Aldrich) as the electrolyte is filled in both cathode and anode chambers, where HMF (99%, Sigma Aldrich) is present in anode during HMFOR tests. The working electrode (anode) is a strip of catalyst-deposited carbon paper, such as the Ni-deposited Freudenberg® described in the previous subsection. The reference electrode is also present in the anode chamber, and it contains Ag/AgCl in 3 M KCl solution (Sigma Aldrich). H-cell tests only focus on the anodic half-cell, so the cathode is just prefilled with the KOH electrolyte and only HER takes place on a Pt foil as the counter electrode. The architecture of an H-cell is shown in Figure 4 in the main text. When OER is studied without biomass upgrading, the anode chamber is filled with only KOH electrolyte without HMF.

1.1.2. Flow-Cell Architecture

For the combined experiments, a four-chamber flow-cell is used to carry out the electrochemical reaction. Each chamber has a cross-section area of 1 cm^2 and is sealed by rubber gaskets. The architecture of the flow cell is indicated in Figure 5 in the main text. This structure of the flow-cell allows the implementation of a gas diffusion electrode on the cathode half-cell, where gaseous carbon dioxide is directly in contact with the electrode hydrophobic back side and can quickly diffuse to the catalytic front side facing the liquid-filled center chamber. In CO_2RR

experiments, high purity CO_2 (99.995%, Linde) is purged through the gas chamber at about 40~60 mL/min. In the anode half-cell, the anolyte is forced to pass through the porous anode catalyst. For both half-cells, 1 M KOH electrolyte is used, where HMF is added in the anolyte. The liquid is circulated at about 23 mL/min between the flow-cell reactor and a reservoir for both half-cells, using soft tubing and peristatic pumps (Cole-Parmer). An illustration of the experiment setup can be seen in Figure A1.

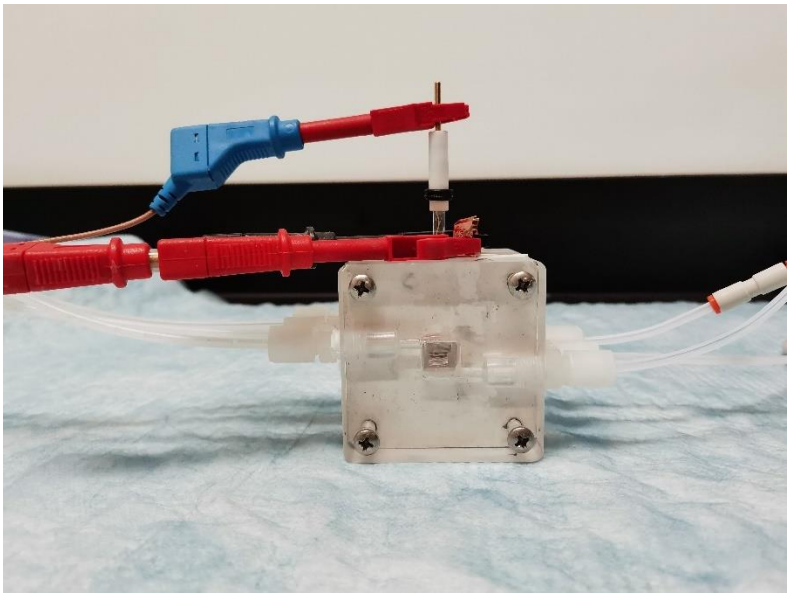

Figure A1 Flow cell setup with continuous inlet of CO_2 and recycle flows of electrolyte.

To correct the standard potential reading for different reaction conditions, the conversion between an Ag/AgCl electrode to the reversible hydrogen electrode (RHE) is shown below.

$$E_{RHE} = E_{Ag/AgCl} + 0.210 + 0.059 \times pH \quad \text{(S1)}$$

Beside the standard electrode correction, ohmic loss of the system is also needed. This requires the knowledge on the system impedance, which is obtained from the electrochemical impedance spectroscopy (EIS) measurement, discussed in later subsection.

1.2. Catalyst Syntheses

1.2.1. Cathode Catalysts

Catalysts for the CO_2RR include 200nm thick layer of copper or silver deposited on Freudenberg® carbon paper by electron-beam evaporator, which is realized through physical vapor deposition (PVD) method. The background atmosphere is set to be lower than 9×10^{-6} torr and the deposition rate is set to 1Å/s. The Cu-deposited carbon paper (Cu/C) has a brown copper tone

residing on the microporous carbon layer, and the Ag/C has a white colour on the deposited side, ensuring a good conductivity for electrocatalysis. The back side of the carbon paper is non-treated, where the hydrophobicity remains intact on the microporous fibre, which is ideal for being a gas diffusion electrode in CO_2RR application.

Another cathode catalyst for CO_2RR is drop-casted Sn nanoparticles. This begins with mixing 50 mg Sn nanoparticles, 200 μL Nafion® solution and 10 mL ethanol as a catalyst ink. Then the ink is sonicated and loaded in a micropipette. The drop-casting is patiently done with the micropipette moving with a "Z" pattern onto the YLS® carbon paper. The loading of Sn nanoparticle is ~1.25 mg/cm^2. After drop-casting is done, the catalyst sample is air-dried before being assembled as the cathode in the electrolyzer.

For non-CO_2RR experiments, the cathode catalyst is just a Pt foil, which facilitates the HER as an auxiliary half-cell reaction.

Figure A2 CO_2RR catalysts: Sn/C, drop casted Sn nanoparticles on carbon paper (left); 200 nm Cu/C, PVD deposited copper on carbon paper (middle); 200 nm Ag/C, PVD deposited silver on carbon paper (right).

1.2.2. Anode Catalysts

In preliminary work, the anode catalyst was synthesized based on a patent on production of NiOOH electrode [119]. A nickel foam (Alibaba) of 2×2 cm was submerged in 2 M NaOH (Sigma Aldrich) solution, then a galvanostatic cycling was applied where an anodic current of 0.4 A was passed for 15 seconds and a cathodic current of -0.4 A for 5 seconds. This was repeated for 30 cycles then followed by a final step polarization where an anodic current of 0.4 A was applied for 300 seconds. After the treatment, a uniform black coating (NiOOH) on the nickel foam was formed, with supposedly a thickness of more than 100 monolayers. This NiOOH electrode serves as a benchmark for the HMFOR experiments.

Another control sample is PVD Ni deposited on carbon paper (Ni/C, 2nm and 200nm), where the thin one is also served as the substrate itself for NiP@Ni/C.

During stage 1, a hybrid of electrodeposition and electroless plating method is used to synthesize Ni-P catalyst. Materials for this method include DI water, $Ni(NO_3)_2 \cdot 6H_2O$, $NaH_2PO_2 \cdot H_2O$, and carbon papers. This procedure has the following steps for Ni-P catalyst preparation on a carbon paper as the anode.

1. Ni/C is prepared using an electron-beam evaporator to have 2nm of Ni deposit on Freudenberg® carbon paper.
2. A 100 mL aqueous plating bath is prepared with 0.1 M $Ni(NO_3)_2 \cdot 6H_2O$ and 0.5 M $NaH_2PO_2 \cdot H_2O$.
3. The Ni/C substrate is cleaned using ethanol, 1 N HCl and RO water, air dry and the back side is taped before it is clamped by an electrode holder.
4. The Ni/C electrode is submerged into the plating solution and connected to the potentiostat as the working electrode while a piece of Pt foil is connected as the counter electrode and Ag/AgCl is connected as the reference electrode (Figure A3).
5. A typical potentiodynamic deposition program is used, where 15 cycles of LSV from -0.3 V to -1.0 V vs. Ag/AgCl are applied (Figure A4).

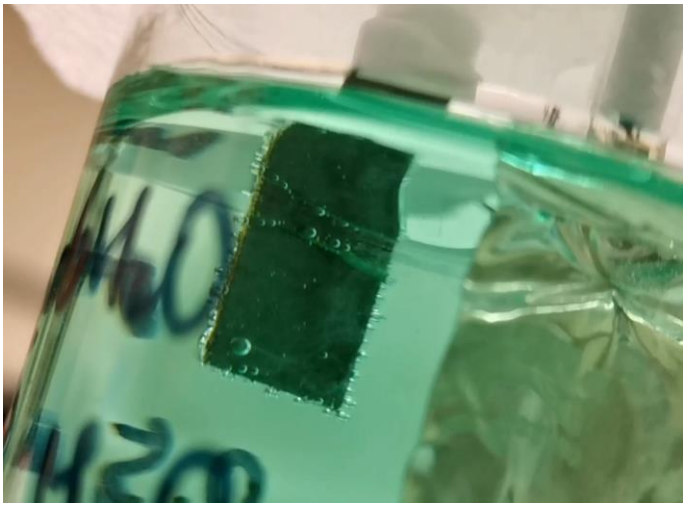

Figure A3 NiP@Ni/C during the LSV-induced electroless plating synthesis.

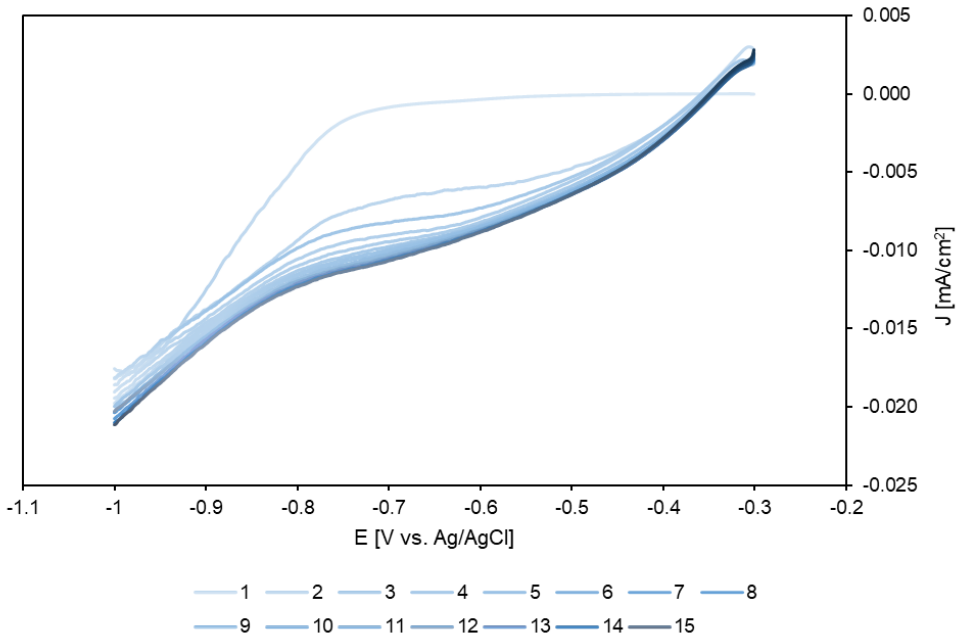

Figure A4 A typical potentiodynamic electrodeposition via LSV scans.

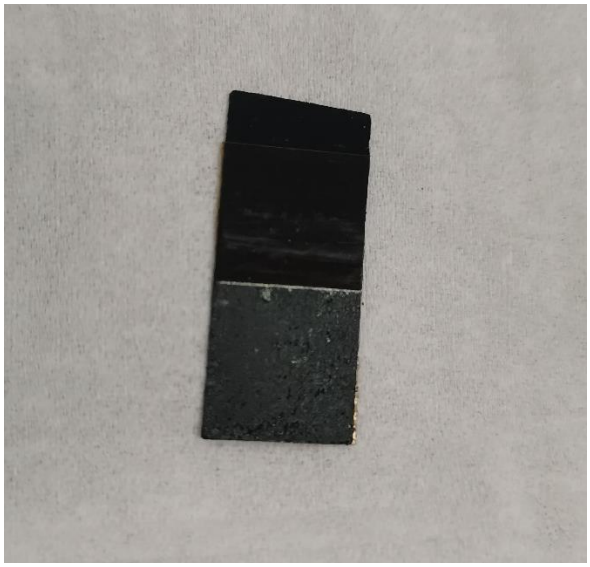

Figure A5 NiP@Ni/C synthesized by electrochemically promoted nickel-phosphorus plating.

In stage 2, the anode catalysts include NiP@Ni/CF, which is Ni-P catalyst deposited by 30 LSV on carbon felt (Alfa Aesar, 99.0%), CoP@Ni/CF, via the same method but prepared with $Co(NO_3)_2 \cdot 6H_2O$ instead of Ni salt, as well as NiCoP@Ni/CF, using the various mixture ratios of Ni and Co nitrate salts.

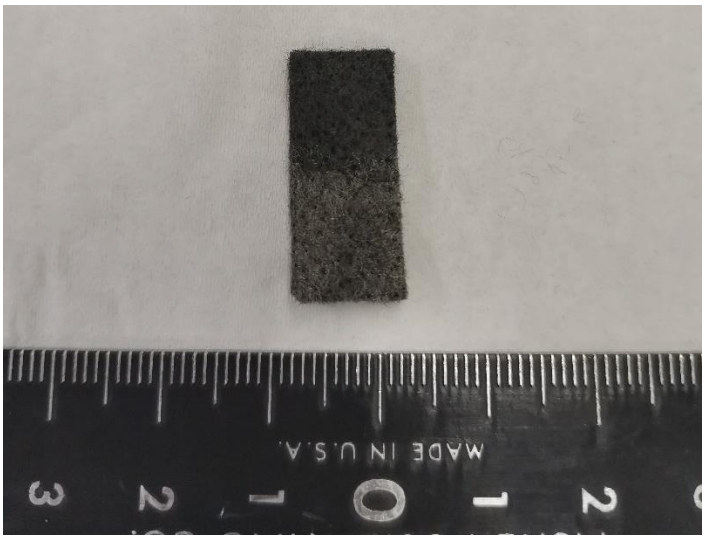

Figure A6 NiP@Ni/CF synthesized by electrochemically promoted nickel-phosphorus plating.

According to literature and preliminary experiment, the oxidation of nickel in alkaline conditions from Ni to Ni^{2+} occurs at -0.2V (vs Ag/AgCl), the oxidation of nickel from Ni^{2+} to Ni^{3+} occurs at about +0.35V, and OER occurs after +0.6V. From literature, the oxidation peak of Co^{2+} to Co^{3+} is around +0.1V [93].

Main investigation focuses on characterizations of such catalysts, where both physiochemical characterization and electrochemical measurements are conducted on these catalysts. Detailed descriptions are written in later subsections.

1.3. Physiochemical Characterization

Various physical and/or physiochemical characterizations on catalyst materials are conducted. In this thesis work, two types of electron microscopy, scanning electron microscopy (SEM) and transmission electron microscopy (TEM), and several X-ray characterization methods including X-ray photoelectron spectroscopy (XPS), X-ray adsorption spectroscopy (XAS) and X-ray diffraction (XRD) are used.

1.3.1. Scanning Electron Microscopy

Scanning electron microscopy, or SEM, is an imaging technique which utilizes a beam of electrons to scan the sample. This technique can reveal the catalyst's surface topography and composition. In the field of electrocatalysis, it is commonly used for catalyst samples characterization because of its robustness and accuracy in catalyst surface visualization. This can verify whether the catalyst prepared is consistent with the design morphology. As an example, SEM images on NiOOH/NF show the macroscopic porous nature and the microscopic rough

surface morphology of the nickel foam derived catalyst in Figure A7. Another set of SEM images on NiP@Ni/C show macroscopic flat nature and microscopic smoother surface morphology in Figure A8.

Sample requirement: electrically conductive on the surface, small to fit specimen stage, can withstand high vacuum and electron beam. Detection limitations: resolution > 1 nm.

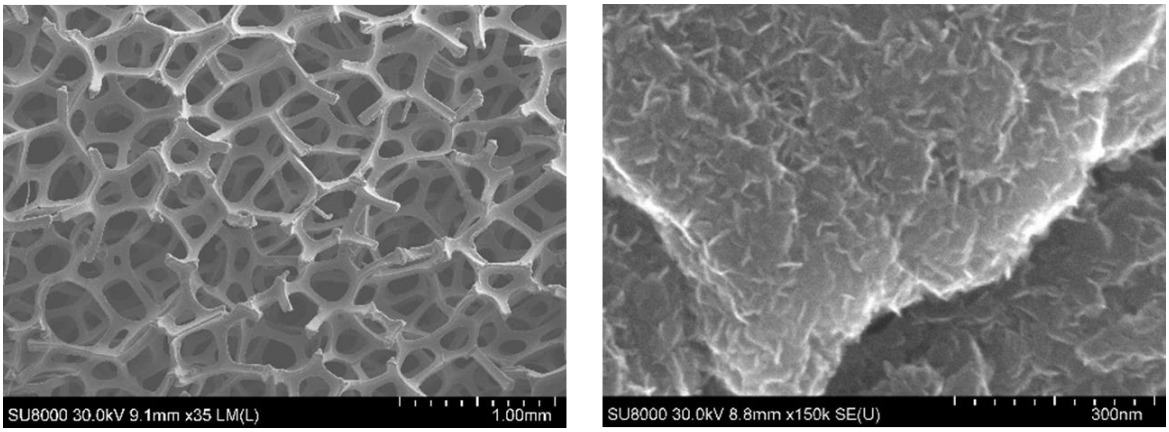

Figure A7 Low and high magnification SEM images of NiOOH/NF catalyst.

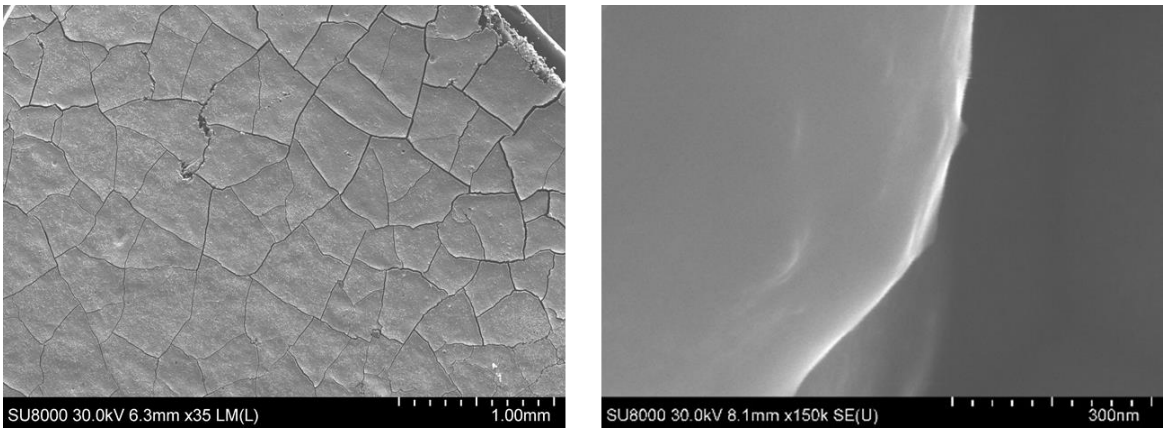

Figure A8 Low and high magnification SEM images of NiP@Ni/C catalyst.

1.3.2. Transmission Electron Microscopy

Transmission electron microscopy, or TEM, is another common type of visualization tool for catalysts. It works by the principals of an electron beam transmitting through the ultrathin layer of sample while the image is collected underneath. Therefore, the specimen is usually less than 100 nm in thickness. It is used to determine the crystal structure and orientation of the catalyst sample. This method can be modified into a scanning transmission electron microscopy (STEM)

to have high-angle annular dark-field imaging (HAADF) or energy-dispersive X-ray spectroscopy (EDX) for more detailed imaging and chemical component analyses. Figure A9 shows TEM and EDX images of Ni-P catalyst with different elemental maps [120].

Sample requirement: thinner than 100 nm or suspension. Detection limitations: resolution without a corrector > 0.2 nm.

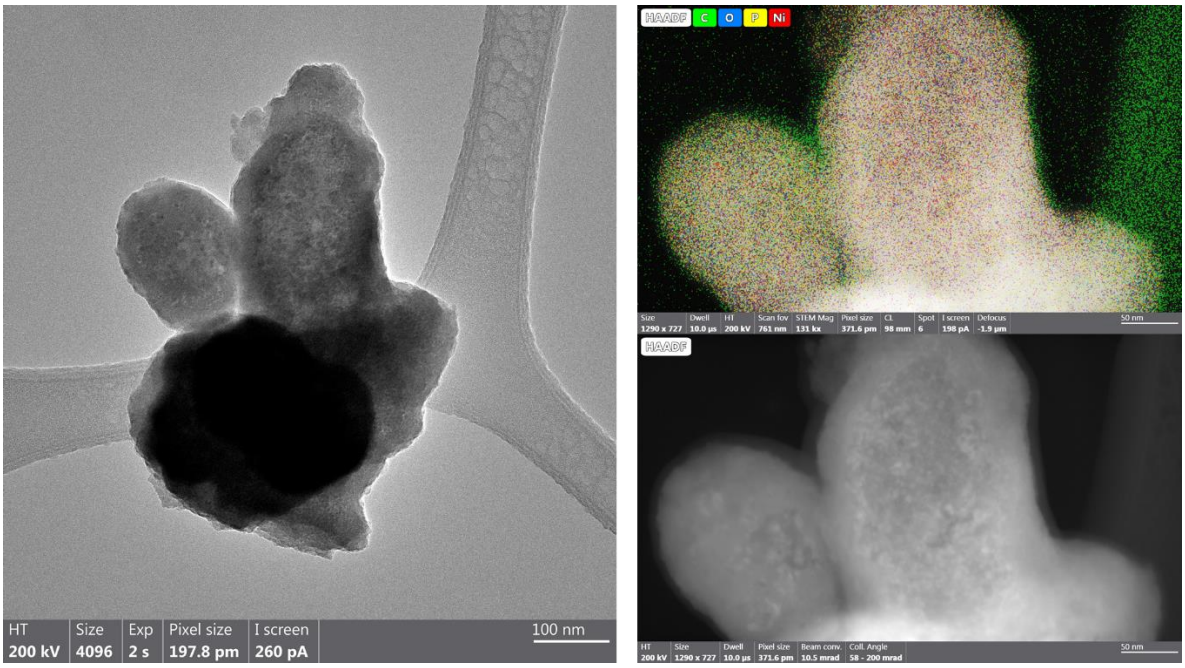

Figure A9 TEM, HAADF and EDX images of NiP@Ni/C catalyst.

1.3.3. X-Ray Photoelectron Spectroscopy

X-ray photoelectron spectroscopy, or XPS, is a quantitative spectroscopic technique for detecting the chemical composition and electronic states of elements within 20 nm of the sample. In the field of electrocatalysis, it is used to analyse the chemistry of the catalyst surface, including the search for active species, change in nanoparticle structure and insights on electronic configuration. Figure A10 illustrates an example of XPS results for Ni-P catalyst.

Sample requirement: include materials such as inorganic compounds, metals, semiconductors, polymers, composites, oils and coatings etc., can withstand high vacuum. Detection limitations: elements with atomic number > 2, measure composition in parts per thousand range.

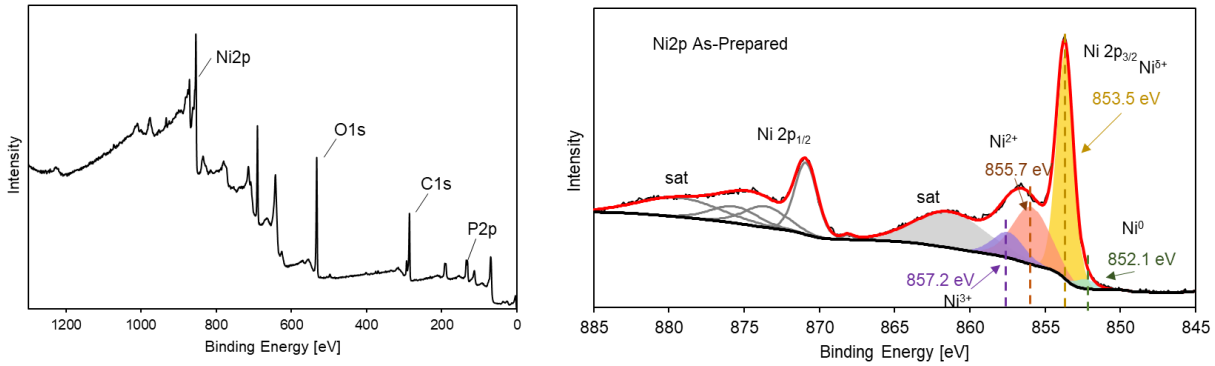

Figure A10 XPS survey (left) and high resolution XPS (right) at Ni k-edge for oxidation state analysis.

1.3.4. X-Ray Adsorption Spectroscopy

X-ray adsorption spectroscopy (XAS) is another technique to analyze chemical composition as well as electronic structure and oxidation state. The adsorption regions are categorized as pre-edge, rising edge and extended regions. Analyses on these regions give information on elemental component, oxidation state and neighboring atoms. Below in Figure A11, it shows the typical X-ray adsorption near-edge structure (XANES), and the extended X-ray adsorption fine structure (EXAFS) on Ni foam.

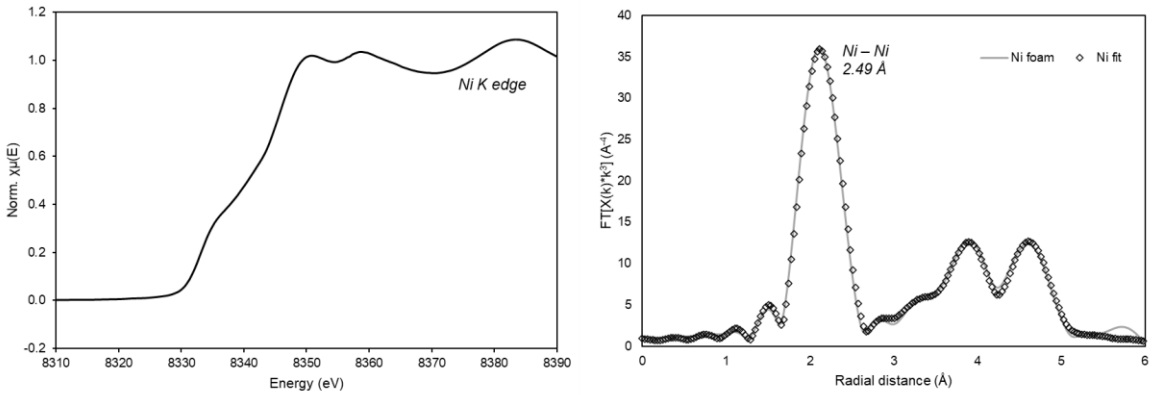

Figure A11 Normalized XANES spectra (left) and fitted EXAFS (right) at Ni k-edge.

1.3.5. X-Ray Diffraction

X-ray diffraction, or XRD, is a scientific method for determining atomic or molecular crystal structure. It utilizes a beam of incident x-ray to detect the diffraction angle and intensity caused by the crystal structures in the sample. Powder x-ray diffraction (PXRD) is common for

randomly arranged crystals rather than a single crystal. Figure A12 shows an example of the XRD patterns for Ni foam.

Sample requirement: generally uniform, crystal structure. Detection limitations: harder for macromolecules, can be fuzzy if crystals too small or not uniform.

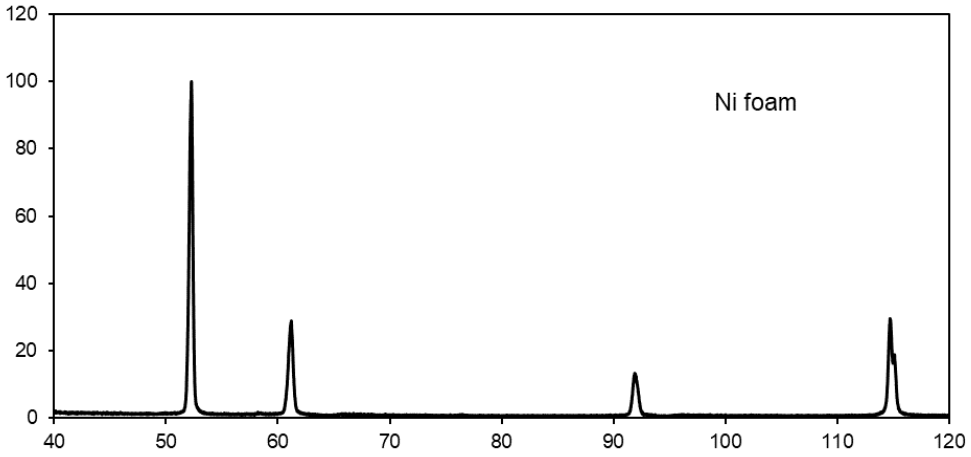

Figure A12 XRD patterns for Ni foam.

1.4. System Electrochemical Characterization

System electrochemical characterization first includes voltammetry, specifically cyclic voltammetry (CV) and linear sweep voltammetry (LSV), which indicate the catalyst activity and electrochemical nature. Then electrochemical impedance measurement (EIS) is carried out to obtain the system resistance and charge transfer resistance. Meanwhile, constant potential or constant current chrono methods (CA and CP) are used to analyze product selectivity and system stability.

1.4.1. Cyclic Voltammetry

The first electrochemical characterization of both CO_2RR and HMFOR is the cyclic voltammetry (CV) in the possible range of the applied potential in each half cell accordingly using 1 M KOH or other electrolytes. PGSTAT204 from Metrohm© Autolab is used as a potentiostat and datalogger. A CV is a cyclic potential-sweeping method that serves to examine multiple important performance metrics and electrocatalytic reaction parameters, including the catalyst activity, current-to-voltage relation, system onset potentials, catalyst surface area, possible mass transfer limitation and some degree of system stability. The result of such measurement is called a cyclic voltammogram, with current or current density as vertical axis and voltage as horizontal axis. A sample of CV for CO_2RR is shown in Figure A13 [121].

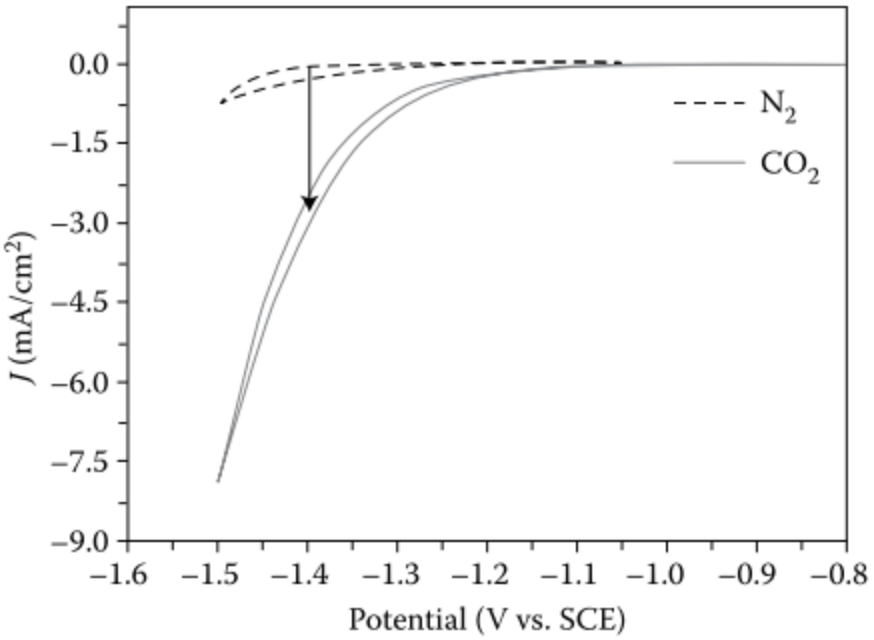

Figure A13 CV of a Cu_3Pt catalyst run in N_2 gas- and CO_2 gas-saturated 0.5 M $KHCO_3$ at a scan rate of 10 mV/s. Adopted from Qiao, Liu [121].

In preliminary work, CVs at a scan rate of 5 mV/s were carried out on the cathode side (Cu/C) with and without the addition of HMF to the anode (NiOOH/NF) chamber (Figure A14). Similarly, a CV at a scan rate of 10 mV/s was carried out on the anode first in a full range without HMF, then with a narrowed range only concerning the OER after all nickel species being oxidized to Ni^{3+} on the catalyst. After this, two more CVs at a slower rate (5 mV/s) were done in the same fashion with 10 mM HMF addition and one without (Figure A15). The oxidation and reduction peaks at 0.34 V and 0.25 V respectively are related to Ni^{2+} oxidation and Ni^{3+} reduction. In the presence of HMF, the oxidation peak is enhanced due to the oxidation of adsorbed HMF molecules; whereas the reduction peak is slightly smaller as a result of the surface reduction of Ni^{3+} active sites after spontaneously oxidizing adsorbed HMF.

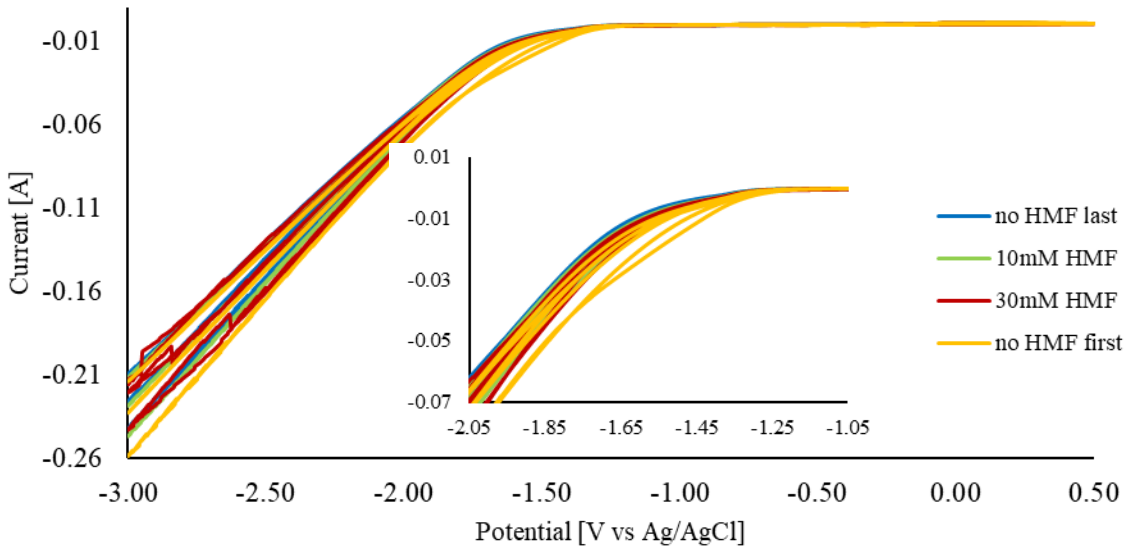

Figure A14 Cathode CV at a scan rate of 5 mV/s on Cu/C in 1 M KOH with no HMF (yellow, blue), 10 mM HMF (green) and 30 mM HMF (maroon). Inset: zoomed in CV showing difference between the first loop (yellow) and the rest.

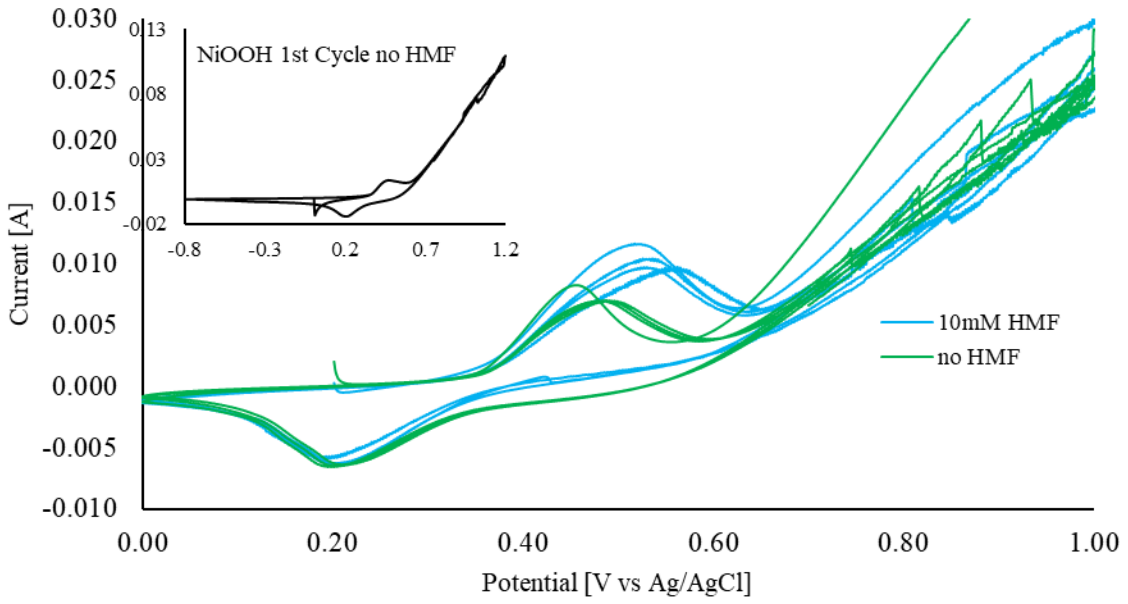

Figure A15 Anode CV at a scan rate of 5 mV/s on NiOOH in 1 M KOH with no HMF (green) and 10 mM HMF (blue). Inset: zoomed in first cycle of NiOOH CV without HMF at a scan rate of 10 mV/s.

1.4.2. Linear Sweep Voltammetry

After analyzing the CVs and selecting a reasonable current, the next measurement of the system is a linear sweep voltammetry, or LSV. Similar to CV, an LSV is also a potential-sweeping

technique for catalyst and system performance analyses. The major parameters that can be found by LSV are the actual current density of individual reactions and onset potential of such reactions.

The initial condition of an LSV is crucial and should be maintained the same when repeated for the same sample in different testing conditions. Normally, just by picking a starting potential before the reaction of interest will yield a clean LSV peak indicating the current density in relation to the applied potential. However, there might be side reactions or surface redox reactions that add artifacts to the resulting current density. With a short procedure that includes a preparatory scan toward potentials in higher magnitude, carefully picking a starting point will ensure minimal reverse current is present in the actual LSV before the peak to be study. In the example of HMFOR, the onset potential of HMFOR is too close to the oxidation of the element nickel in the catalyst, both occurring slightly above 0.35 V vs. Ag/AgCl in 1 M KOH. After this treatment of a preparatory scan, there was only a very small portion of nickel being reduced back to Ni^{2+}. Therefore, the LSVs shown in Figure A16 are results of HMFOR and/or OER with a small influence of Ni oxidation. To completely eliminate the artifact from Ni oxidation and reveal the true current density of HMFOR and OER, a simple subtraction of the HMF-absent samples from the HMF-present ones yields Figure A17.

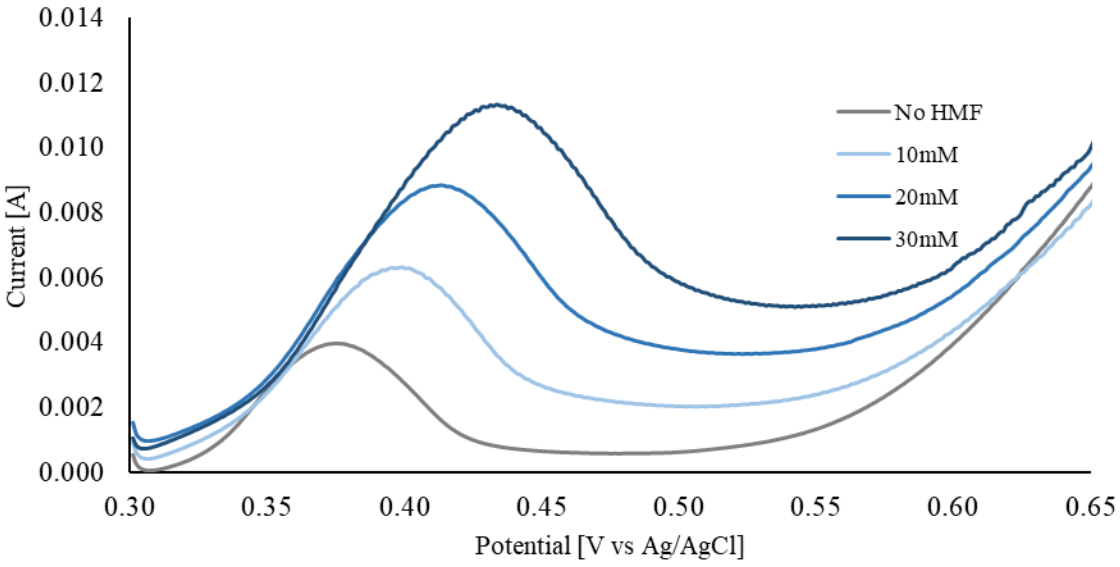

Figure A16 Anode linear sweep voltammetry at a scan rate of 5 mV/s on NiOOH in 1 M KOH with no HMF (grey), 10 mM HMF (pale blue) and 20 mM HMF (light blue), and 30 mM HMF (dark blue).

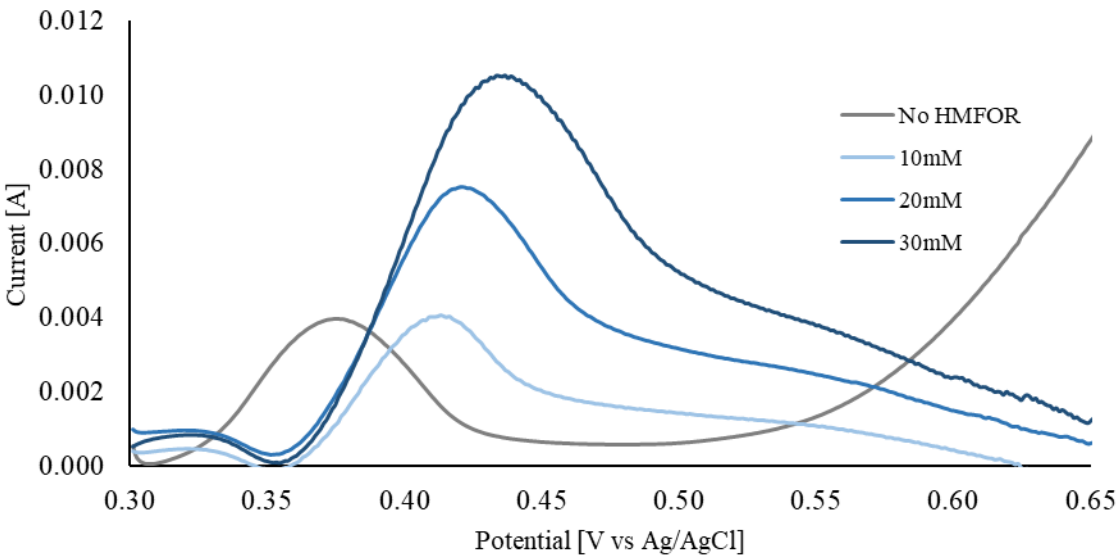

Figure A17 LSV partial current of HMFOR in comparison to Ni oxidation and OER in 1 M KOH.

For catalyst activity on an individual reaction, Tafel parameters can be obtained by drawing a Tafel plot (example shown in Figure A18), where the slope and y-intercept of the curve are directly related to the exchange current and transfer coefficient. This is because the charge transfer or activation overpotential is related to exchange current and transfer coefficient in the Tafel equation:

$$\eta_{act} = a + blog(i) = -2.303\frac{RT}{\alpha F}log(i_0) + 2.303\frac{RT}{\alpha F}log\ (i) \qquad \text{(S2)}$$

Therefore, when plotting overpotential versus current in logarithmic scale, the transfer coefficient α can be calculated from the slope and the exchange current i_0, which is the current that takes place in equilibrium, can be obtained from the y-intercept. It is worth noting that at "dynamic" equilibrium, although the net reaction rate (i.e. current) is zero, the backward and forward reaction rate is not zero and has the value of equivalent to the exchange current.

In the case of multiple electron transfer or complex reaction pathways, the Tafel slope can be used to indicate the intrinsic activity of the catalyst in the overall reaction.

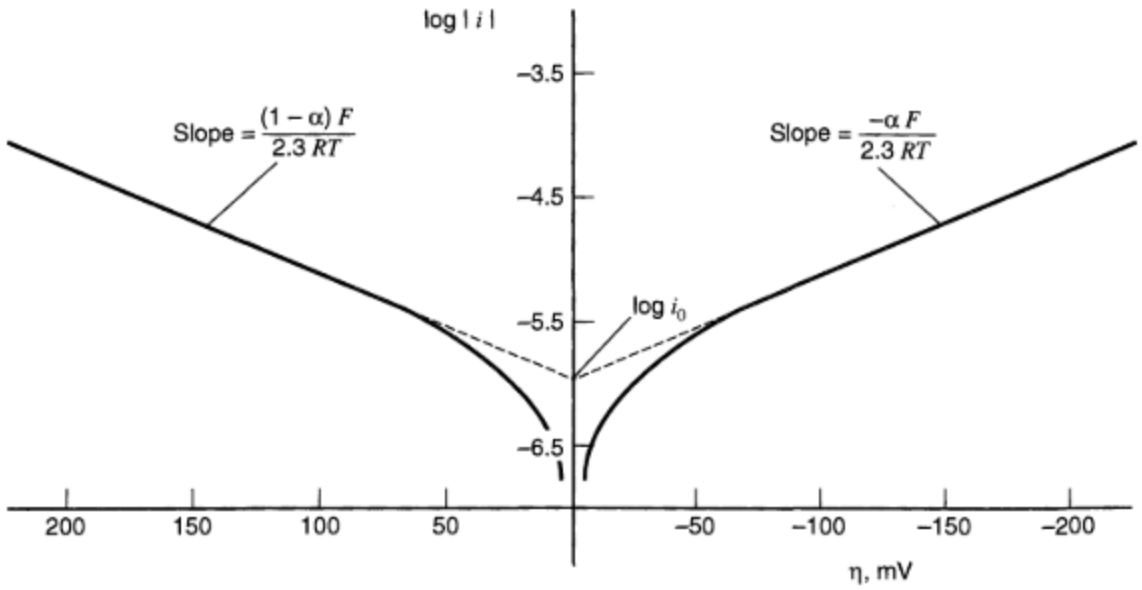

Figure A18 An example of Tafel plot where the slope and y-intercept reveal the Tafel parameters. Adopted from Bard and Faulkner [122].

1.4.3. Electrochemical Impedance Spectroscopy

The electrical resistance of an electrochemical system is found by electrochemical impedance spectroscopy (EIS). This is essentially a frequency response analysis technique, which applies a set range of frequencies either potentiostatically (voltage) or galvanostatically (current). The electrochemical system can be an analogue to the resistor-capacitor circuit, where ion migration in the electrolyte is equivalent to a resistor, and the double layer on the electrode surface is equivalent to a capacitor. This then results in a RC circuit that gives a delayed response when a sinusoidal input of electrical signal is applied. Since the frequency is scanning from a large value to a smaller one (typically from 1 MHz to 1 Hz), the system will be more impacted (higher phase angle) toward the lower frequencies as they become closer to the natural frequency of the RC circuit.

Therefore, the system resistance is taken at the beginning of the EIS measurement, when the Bode plot (Figure A19) has the minimum phase angle or when the Nyquist plot (Figure A20) has the smallest imaginary -Z" value. On the other hand, when measuring charge transfer resistance of a reaction, the diameter of the semi-circle in the Nyquist plot is taken for calculation.

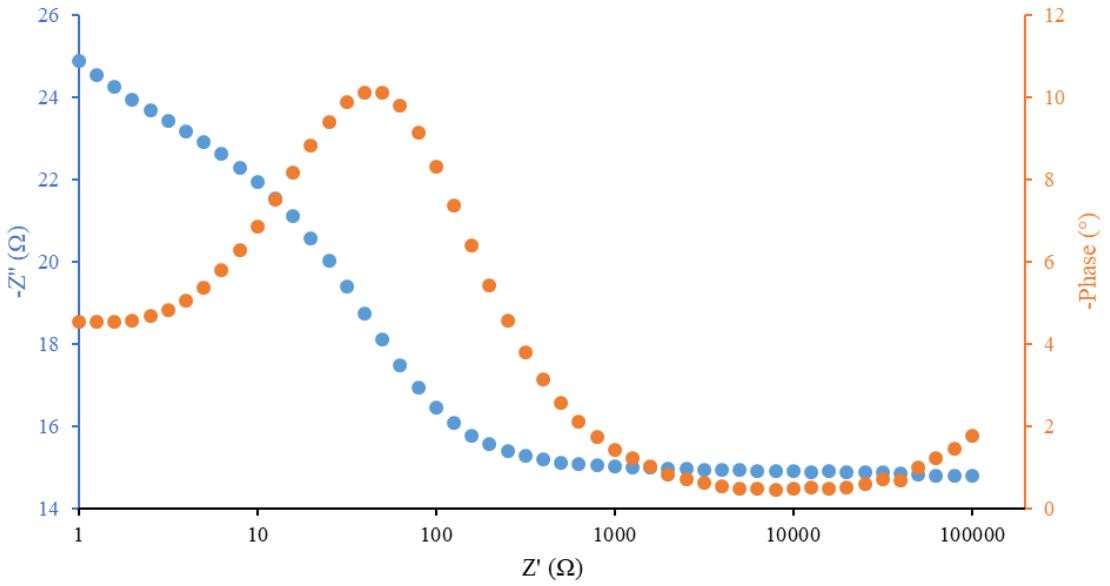

Figure A19 Bode plot in an EIS measurement, with complex impedance Z (blue) and phase angle (orange) recorded with respect to input frequency.

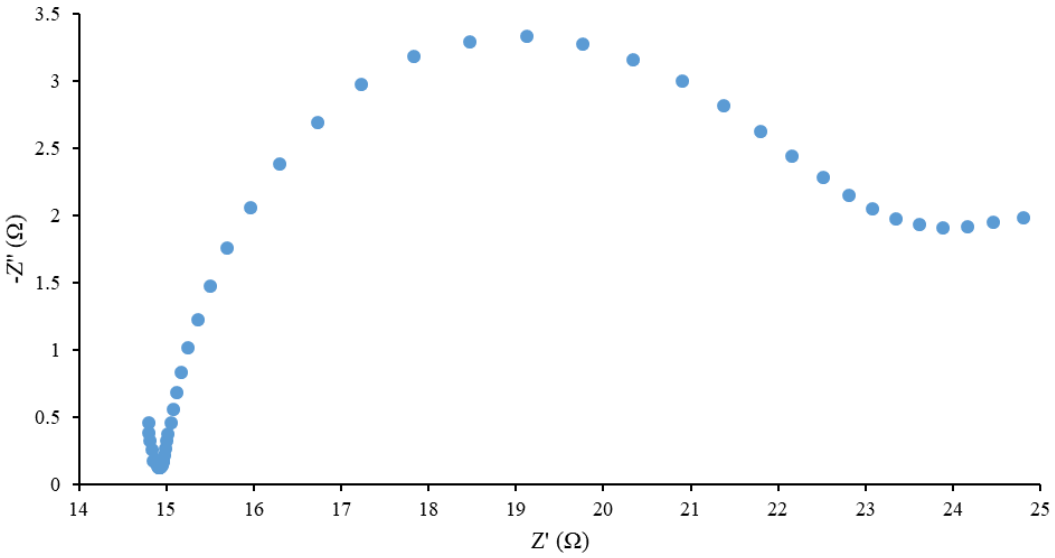

Figure A20 Nyquist plot in an EIS measurement with imaginary component (-Z") and real component (Z') of impedance plotted as y- and x-axis.

Once the system resistance is obtained, the Ohmic loss can be calculated:

$$\eta_{ohm} = R_{sys} I_{applied} \quad \text{(S3)}$$

The theoretical equilibrium potential of a reaction can be calculated using the applied potential, activation overpotential, and ohmic loss, if there is no significant mass transfer limit.

$$E_{eq} = V_{applied} - \eta_{act} - \eta_{ohm} \quad \text{(S4)}$$

Since there is a theoretical standard potential from thermodynamics for each product in a reaction, using it to calculate for the equilibrium potential and comparing it with the previously calculated potential can account for any other overpotentials. Nernst equation gives the following calculation for the equilibrium potential:

$$E_{eq} = E^0 - \frac{RT}{nF}\sum_i \nu_i ln a_i \quad \text{(S5)}$$

where E^0 is the standard potential R is the universal gas constant, T is temperature, n is number of moles of electron transferred per mole of product formed, ν is the stoichiometry coefficient, a is the fugacity of the species.

1.4.4. Chronoamperometry

One of the chrono methods is the chronoamperometry, or CA experiment. This is done by fixing an applied potential across either a half cell (3 electrode setup) or across the entire electrolyzer (2 electrode setup) and monitor the result current in the electrolyzer. Over time, the behaviour of the current reveals the reaction kinetics and catalyst stability.

Preliminary work on CO_2RR has shown that the PVD Cu/C catalyst is driving the reduction reaction with a decent current density (-100 ~ -200 mA/cm^2), which means that the kinetics of the reaction was considerable. Within 30 minutes of test time, the current was mostly steady, giving a feasible catalyst candidate. Since the voltage is fixed in a CA, the average current or current density can be obtained and used to further calculate FE of each product detected.

1.4.5. Chronopotentiometry

Another experimental method is fixing the current rather than the potential. For the flow-cell, a current density is selected to conduct the chronopotentiometry experiments, aiming to monitor the anode voltage (Van), cathode voltage (Vcat) and the full cell voltage (Vcell). The behaviour of voltages allows for interpretation of reaction activation as well as system stability.

In preliminary work for combined system experiments (Cu/C as cathode and NiOOH/NF as anode), 5 mA/cm^2 and 10 mA/cm^2 current densities were selected and different amount of HMF was added to the anode electrolyte. Figure A21 shows the results of full cell CP at 5 mA with and without the addition of HMF in the anode. The voltage shown is the cathode potential with respect to the anode, thus y-axis is the full cell potential in the plots. Vcell was found to vary due to anode overpotential altered by the added HMF. Similar results are also observed when a current of 10 mA was applied to the electrolyzer (Figure A22). This change in Vcell is summarized in Figure

A23 where a trend of the applied full cell voltage is seen to be around the same from no HMF added to 5 mM HMF added and then decrease at higher concentrations for 10 mA/cm^2 current density. This means that Van can be reduced at higher concentrations of HMF in the electrolyte which lowers Vcell.

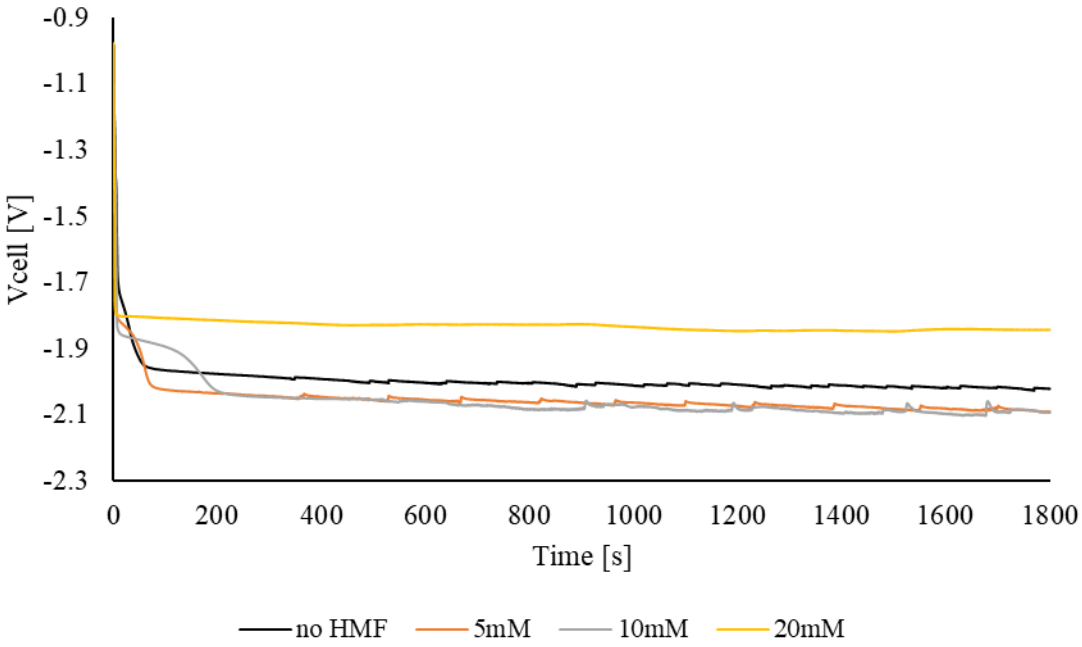

Figure A21 Combined chronopotentiometry at 5 mA with no HMF (black), 5 mM HMF (orange), 10 mM HMF (grey) and 20 mM HMF (yellow).

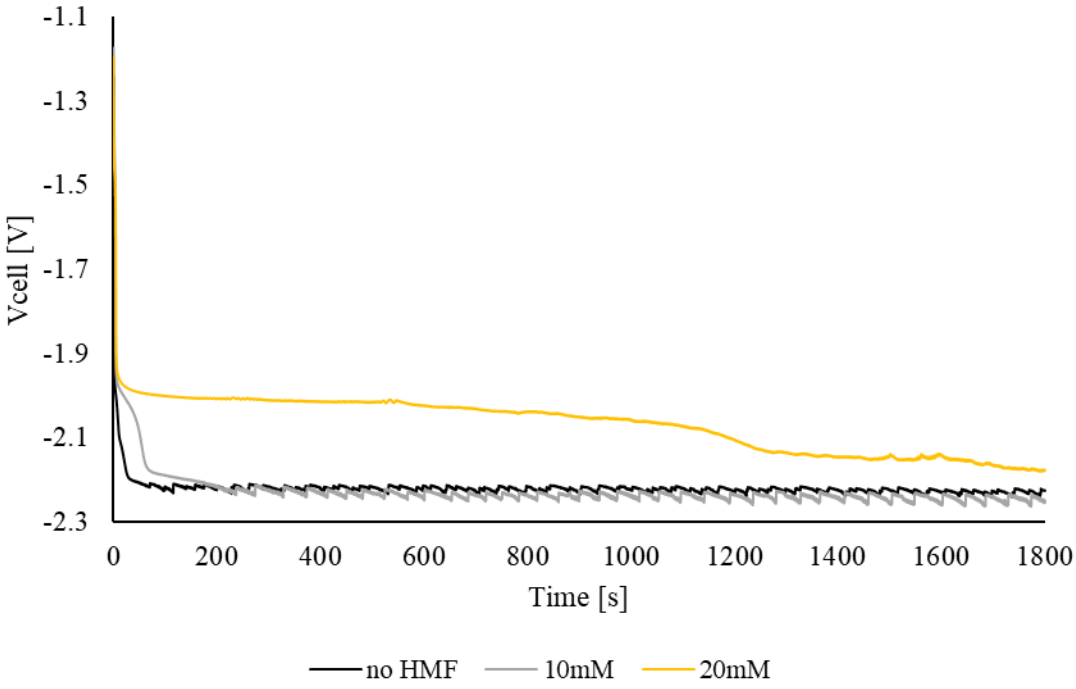

Figure A22 Combined chronopotentiometry at 10 mA with no HMF (black), 10 mM HMF (grey), and 20 mM HMF (yellow).

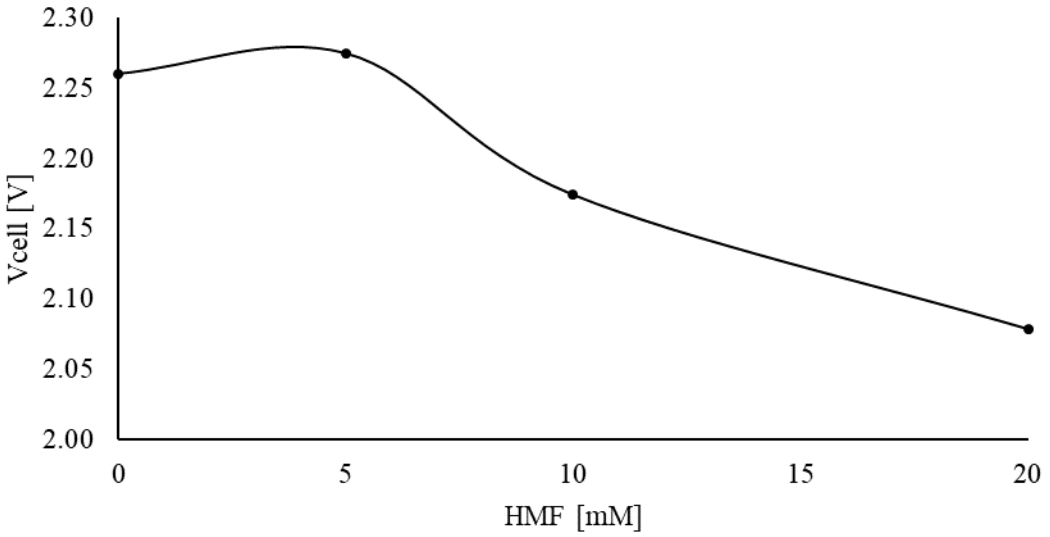

Figure A23 Applied full cell potential at 10 mA for different HMF concentrations: no HMF, 5 mM, 10 mM and 20 mM of HMF.

1.5. Product Analysis

The CO_2RR can yield both gaseous and liquids products, whereas the HMFOR is only carried out in liquid phase, the product analyzing tools therefore include gas chromatography (GC) and high-performance liquid chromatography (HPLC), as well as NMR analysis.

1.5.1. Gas Chromatography

Gas chromatography, or GC, is used for gaseous product detection and quantification. It is a common type of chromatography for separating and analyzing non-decomposing compounds which can be vaporized. GC is typically used for testing the purity of a given sample or separating various components in that sample with the ability to also quantify them. It could be used to identify a compound given a standard reference chromatogram.

The GC is an Agilent 6890. Sample collecting and use of GC are guided by the standard operating procedure (SOP) developed in the laboratory. An illustration of GC readings is shown in Figure A24.

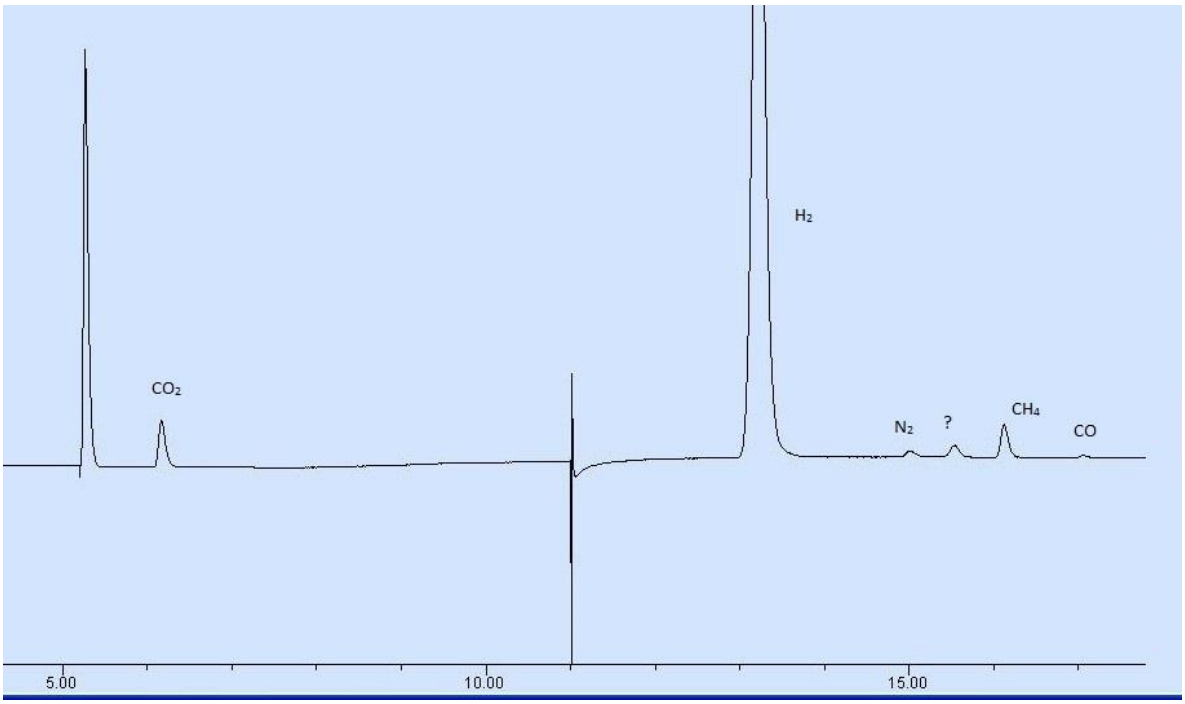

Figure A24 Reference sample of gas mixture detected by GC. The peak between nitrogen gas (N_2) and methane (CH_4) is an artifact in the results.

1.5.2. High-Performance Liquid Chromatography

High-performance liquid chromatography (HPLC) is a common technique in analytical chemistry used to separate, identify and quantify each component in a mixture. It utilizes pumps

to pass a pressurized liquid solvent that carries the sample mixture through a column filled with solid adsorbent materials. Each component in the sample interacts differently with the adsorbent materials and thus has different flow rates leading to different residence time in the column. The exit of the column is directed to detectors such as ultraviolet-visible spectroscopy detector, or UV-vis, and reflective index detector, or RI, making it possible for quantitative analysis. UV-vis (Figure A25) can be used to detect organic acids such as formic acids, acetic acid, HMFCA and FDCA as well as aldehydes like HMF and DFF. RI is only used to detect alcohols such as methanol, ethanol and 1-propanol.

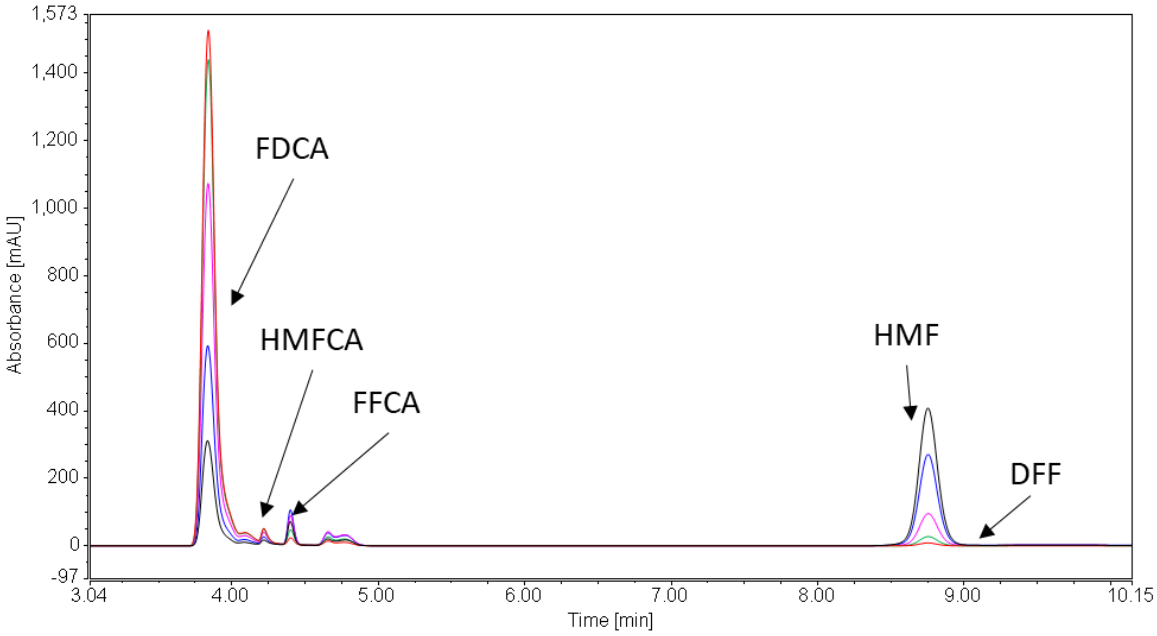

Figure A25 HPLC result on HMFOR with product detection over time.

1.5.3. Nuclear Magnetic Resonance

Nuclear magnetic resonance, or NMR, is another liquid sample analyzing technique. It is commonly used as a physical observation technique to find the quantity and location of a designated type of atoms. The most common NMR isotopes to analyze are ^{1}H and ^{13}C. For the liquid products from CO_2RR and biomass upgrading CA or CP experiments, the liquid sample is collected in an NMR tube at the end of the experiment and analyzed using a ^{1}H Varian Inova 500 MHz NMR Spectrometer (QANUC 500) to determine the product concentration in the electrolyte. The reference used is DMSO and the solvent is deuterium oxide (D_2O). Post-NMR data analysis is done in MestReNova® software (Figure A26).

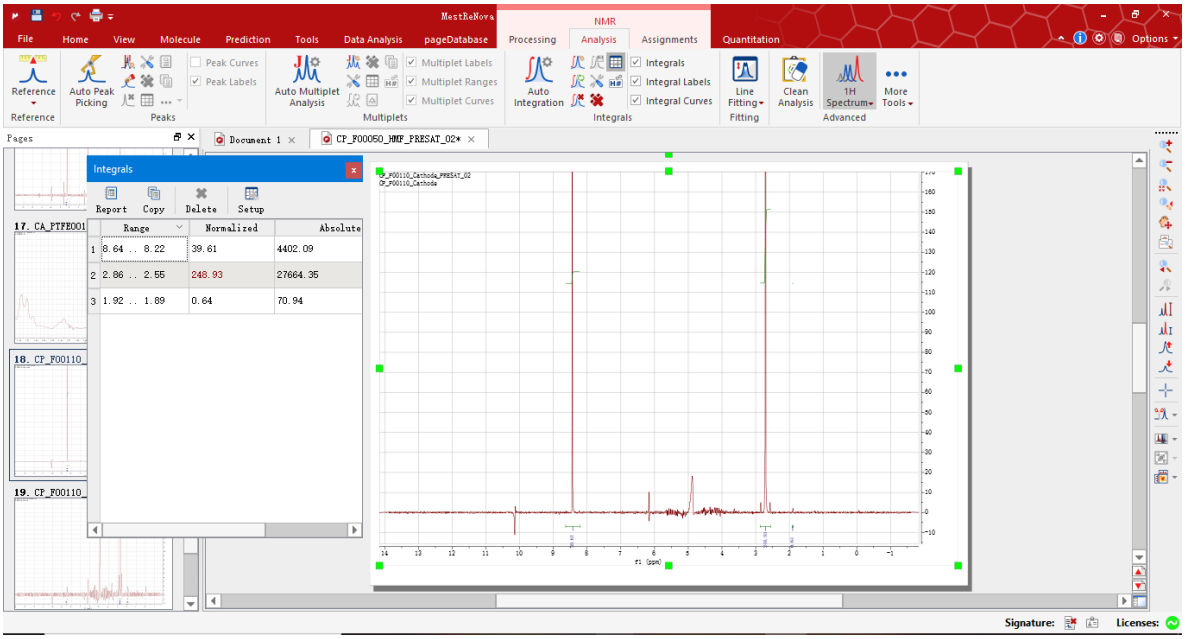

Figure A26 Software MestReNova® for post-NMR data analysis.

1.5.4. Faradaic Efficiency

After obtaining the final product concentration from GC, HPLC or NMR, the Faradaic efficiency of each product is calculated based on the applied current and experiment time:

$$FE_i = \frac{theoretical\ charge\ needed}{actual\ charge\ passed} \times 100\% = \frac{m_i nF}{It} \times 100\% \qquad \text{(S6)}$$

where m is the number of moles of the product in the electrolyte, n is the number of electrons transferred per molecule of product formed, F is the Faradaic constant (96485 C/mol electron), I is the fixed current and t is the time.

Previous work on CO_2RR and HMFOR combined system has shown high FE in formate in the cathode and considerable FE in FDCA in the anode. Most recent results using a 2-electrode setup (2E) are summarized in Figure A27.

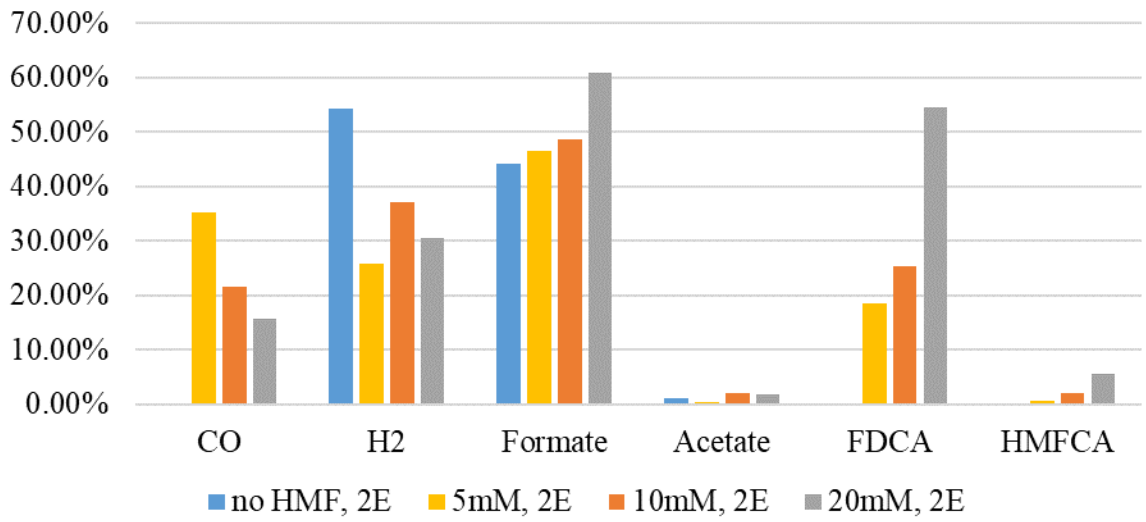

Figure A27 Preliminary FE summary for cathode products (CO, H_2, formate and acetate) and anode products (FDCA and HMFCA) in a CO_2RR+HMFOR combined electrolyzer (Cu/C cathode, NiOOH/NF anode) under a CP experiment at 10 mA applied in 2E mode.

1.5.5. Energy Efficiency

From the standard potentials and the applied voltage, voltage efficiency can be calculated:

$$VE = \frac{E^0_{OER} - E^0_{CO_2RR}}{V_{cell}} \times 100\% \quad \text{(S7)}$$

Once the Faradaic efficiency and the voltage efficiency are obtained, the energy efficiency of the electrolyzer can be calculated for each product:

$$EE_i = VE \times FE_i \times 100\% \quad \text{(S8)}$$

When CO_2RR is combined with HMFOR, another way to inspect the energy saving is by dividing the conventional CO_2RR-OER voltage by the improved cell voltage when HMF is added at the same current:

$$\eta_{cell} = \frac{\Delta E_{CO_2RR-OER}}{V_{cell}} \quad \text{(S9)}$$

This parameter effectively indicates the voltage saving index of the electrochemical cell, where a number higher than unity means better energy saving. A theoretical maximum value of the saving index for conventional OER occurs when the cathode and the anode have zero overpotential.

Table A1 List of catalyst and system efficiencies. Voltages are vs. RHE unless stated otherwise, without iR compensation. Variables followed by the prime symbol indicate the proposed combined system with Ni-P catalyst for HMFOR.

Reference	Product	Catholyte	n	J (mA/cm^2)	FE	E0 (V)	E0 used	Vcathode	Cathode Catalyst	Vanode	Anode Catalyst	Vanode'	Vcell	Vcell'	VEcat (%)	VEcell (%)	VEcell' (%)	EEcat (%)	EEcell (%)	EEcell' (%)	improv. %
This work	*Formate*	*1M KOH*	*2*	*100*	*75*	*-0.25*	*-0.25*	*-1.13*	*Sn/C*	*2.13*	*NiP/NiCF*	*1.87*	*3.16*	*2.92*	*64.9*	*46.8*	*50.7*	*48.7*	*35.1*	*38.0*	*8.22*
This work	*Formate*	*1M KOH*	*2*	*100*	*8.4*	*-0.25*	*-0.25*	*-1*	*Cu/C*	*2.11*	*NiP/NiCF*	*1.86*	*3.11*	*2.86*	*66.4*	*47.6*	*51.7*	*5.6*	*4.0*	*4.3*	*8.74*
This work	*Acetate*	*1M KOH*	*8*	*100*	*1*	*0.125*	*0.125*	*-1*	*Cu/C*	*2.11*	*NiP/NiCF*	*1.86*	*3.11*	*2.86*	*49.6*	*35.5*	*38.6*	*0.5*	*0.4*	*0.4*	*8.74*
This work	*CO*	*1M KOH*	*2*	*100*	*21*	*-0.106*	*-0.106*	*-1*	*Cu/C*	*2.11*	*NiP/NiCF*	*1.8*	*3.11*	*2.86*	*59.9*	*43.0*	*46.7*	*12.6*	*9.0*	*9.8*	*8.74*
This work	*Ethylene*	*1M KOH*	*12*	*100*	*31*	*0.064*	*0.064*	*-1*	*Cu/C*	*2.11*	*NiP/NiCF*	*1.86*	*3.11*	*2.86*	*52.3*	*37.5*	*40.8*	*16.2*	*11.6*	*12.6*	*8.74*
This work	*Ethanol*	*1M KOH*	*12*	*100*	*11*	*0.084*	*0.084*	*-1*	*Cu/C*	*2.11*	*NiP/NiCF*	*1.86*	*3.11*	*2.86*	*51.4*	*36.8*	*40.1*	*5.7*	*4.1*	*4.4*	*8.74*
This work	*1-Propanol*	*1M KOH*	*18*	*100*	*3.3*	0.095	0.095	*-1*	*Cu/C*	*2.11*	*NiP/NiCF*	*1.86*	*3.11*	*2.86*	*50.9*	*36.5*	*39.7*	*1.7*	*1.2*	*1.3*	*8.74*
This work	*CO*	*1M KOH*	*2*	*100*	*91*	*-0.106*	*-0.106*	*-1*	*Ag/C*	*2.11*	*NiP/NiCF*	*1.88*	*3.18*	*2.95*	*58.1*	*42.0*	*45.3*	*52.9*	*38.2*	*41.2*	*7.80*
W. Cheng et al., 2020	CO	1M KOH	2	14	99	-0.106	-0.106	-0.6	Ag	1.63	Ni	1.4	2.2	2.0	73.0	59.9	66.8	72.3	59.3	66.1	11.50
C. Gabardo et al., 2018	CO	7M KOH	2	90	86	-0.106	-0.106	-0.8	Ag-Naf (PTFE)	2	Ni	1.78	2.8	2.6	65.8	47.7	51.8	56.6	41.0	44.5	8.53
R. Xia et al., 2020	CO	1M KOH	2	100	95	-0.106	-0.106	-0.4	Ag-Naf (PTFE)		Graphite	1.9	2.5	2.3	82.0	52.8	58.1	77.9	50.2	55.2	10.00
B. Kumar et al., 2017	Formate	0.1M KHCO3	2	6	80.1	-0.25	-0.2	-0.8	SnO2 pNW		Pt	1.38	2.4	2.2	70.4	60.1	65.6	56.4	48.1	52.5	9.17
Y. Duan et al., 2020	Formate	0.1M KHCO3	2	2	98	-0.25	-0.225	-0.8	Bi/rGO		Pt	1.3	2.3	2.1	71.7	62.2	69.3	70.2	60.9	67.9	11.43
W. Guo et al., 2021	Methanol	[Bmim]BF4(25 mol%)aq	6	67	88.6	0.016	-0.89	-1	Sn/V-CuO	2.28	Pt	1.65	3.3	2.7	95.1	64.6	80.0	84.2	57.3	70.9	23.77
A. Sedighian et al., 2020	Methane	1.5M KHCO3	8	250	48	0.169	0.169	-0.98	sputtered Cu		Ni foam	2.55		3.5	48.0		30.1	23.0		14.4	
D. Zang et al., 2021	Acetate	saturated NaHCO3	8	110	48.68	0.125	0.125	-1.13	Mo_8@Cu/TNA		Pt net	1.88		3.0	46.8		36.7	22.8		17.9	
X. Wang et al., 2020	Ethanol	1M KOH	12	160	52	0.084	0.084	-0.68	N–C/Cu	2.99	Ni foam	2.2	3.7	2.9	60.0	31.2	39.8	31.2	16.2	20.7	27.43
C. Dinh et al., 2018	Ethylene	7M KOH	12	75	70	0.064	0.064	-0.54	Cu-Naf (PTFE)		NiFe	1.7		2.2	65.9		52.1	46.1		36.4	
R. Geioushy et al., 2017	1-Propanol	0.5 M NaHCO3	18	1	30	0.095	0.095	-0.41	GN/ZnO/Cu2O		Pt coil	1.32		1.7	69.4		65.7	20.8		19.7	
S. Lee et al., 2015	1-Propanol	0.1 M KCl	18	6	8.7	0.095	0.095	-1.60	biphasic Cu2O		Pt plate	1.4		3.0	40.1		37.8	3.5		3.3	

2. HMFOR Manuscript

2.1. Contribution of Authors

The first author, Roger Lin, was responsible for conceptualizing, performing experimental work, data analysis and writing of the manuscript. The second author Mahdi Salehi performed some physical characterizations including SEM, TEM, XAS, XPS. The third author Jiaxun Guo was helping in conceptualizing and providing feedback on the project. The corresponding author Prof. Ali supervised and revised the work while acquiring funding.

2.2. Manuscript

High Oxidation State Enabled by Plated Ni-P Achieves Superior Electrocatalytic Performance for 5-Hydroxymethylfurfural Oxidation Reaction

Roger Lin[a], *Mahdi Salehi*[a], *Jiaxun Guo*[a], *Ali Seifitokaldani*[a,*]

[a] Department of Chemical Engineering, McGill University,
3610 Rue University, Montréal, QC, H3A 0C5, Canada
* Corresponding author
E-mail address: ali.seifitokaldani@mcgill.ca (A. Seifitokaldani)

ABSTRACT

Electrochemical 5-hydroxymethylfurfural oxidation reaction (HMFOR) as a clean biorefinery process, promotes a circular economy with value-added products. In HMFOR, the intrinsic catalytic activity and charge transfer mechanisms are crucial. Herein, nickel co-deposited with phosphorus (Ni-P) attains superior electrocatalytic performance compared to Ni and its oxyhydroxides for the HMFOR. Such electrocatalytic activity of the Ni-P catalyst is attributed to the high oxidation state of surface Ni species, supported by the bulk Ni-P component. An unprecedented charge storing capacity enabled by the bulk Ni-P material maintains the spontaneous reaction between HMF and Ni^{3+} species to achieve a current density of 10 $mA.cm^{-2}$ normalized by the electrochemical active surface area at low potential of 1.42 V vs RHE, reaching a 97% Faradaic efficiency towards 2,5-furandicarboxylic acid. This work, for the first time, sheds light on the importance of the electrode bulk material by showcasing the HMFOR via Ni-P catalyst incorporating charge-holding bulk component.

Keywords:

Plated Ni-P; HMF oxidation reaction; FDCA production; Electrocatalysis; Charge Storing Capacity

1. Introduction

As one of the byproducts in biorefinery industry, 5-hydroxymethylfurfural (HMF) is a biomass-derived furanics chemical that is usually produced from dehydration of pentose or hexose sugars. It has become a promising bio-based chemical intermediate for its abundant source from biomass such as fructose and its conversion into valuable platform chemicals. [1] The market price of HMF was more than 500 USD/kg, with a market size of 56 million USD in 2019, and the expected compound annual growth rate (CAGR) of the HMF market is 1.45% before 2025. [2] Its oxidation product, 2,5-furandicarboxylic acid (FDCA), is considered an important platform chemical and precursor in various industrial syntheses for products including pharmaceutical, agricultural, and polymeric materials. [1, 3] The market size of FDCA is expected to be over 780 million USD in 2027, having a CAGR of 8.7% from 390 million USD in 2018. [4] One of the most desired products from FDCA is polyethylene furanoate (PEF), which possesses similar or superior thermal, mechanical and barrier properties and is more sustainable than the currently used petroleum-based polyethylene terephthalate (PET). [5] The prime objective would be to replace the PET plastic bottles with the better PEF, which has the potential to quickly reach a large-scale production. Depending on the first oxidation location on the molecule, the oxidation of HMF has two paths, one through the oxidation of the aldehyde group yielding an intermediate called 5-hydroxymethyl-2-furancarboxylic acid (HMFCA), another through the oxidation of the hydroxyl group via 2,5-diformylfuran (DFF), but both ways lead to the intermediate 5-formyl-2-furancarboxylic acid (FFCA) and the final product FDCA (Scheme 1). [6] By valorizing the biomass byproducts such as HMF via clean energy, a circular economy model can be established, which benefits both the biorefinery industry and the general public, rendering the electrochemical oxidation of HMF a highly researched topic. Another profound benefit of this technique is the potential to reduce CO2 emission due to the use of clean energy (e.g., renewable electricity) which can transform the conventional fossil-fuel-powered thermal treatment into a more sustainable biorefinery process. In fact, the number of publications regarding this electrocatalytic process has seen a growing increase since 2010 (Figure S1).

Early works on oxidation of HMF utilized precious metals such as Au and Pd, via an aerobic oxidation process which often used harsh conditions (high temperature, high O2 pressure, toxic chemical agents etc.). [6] However, single metal catalysts of Au, Pt and Pd were not particularly selective for the final product FDCA, and the focus was later shifted towards

transitional metal catalysts including Ni, Co, Fe, and Cu inspired by the water splitting process. [7-10] Meanwhile, there has been studies using 2,2,6,6-tetramethylpiperidine 1-oxyl (TEMPO) or its derivative as mediator and noble metals (Au, Ag, etc.) as working electrode for homogeneous HMF oxidation. [11] However, the homogeneous catalysis method still has feasibility challenges including material and separation costs. Among recent studies, various transition metal-based electrocatalysts were synthesized with p-block elements such as boron, carbon, nitrogen, oxygen, phosphorus, and sulfur. [12-19] Since then, some impressive results have been obtained in electrochemical performance metrics such as total current density (>200 mA cm^{-2} by Ni_2P NPA/NF and Ni_3S_2/NF) [15, 16] and Faradaic efficiency (98-99% by NiFe LDH and Ni_3N@C). [14, 17] Meanwhile, mechanic studies have also shown the active sites to be the transition metal with higher oxidation states including hydroxide, oxyhydroxide and their coordination species. [20-22] It is understood that for nickel-based catalysts, a higher oxidation state is required for complete HMF oxidation, which should be the main goal for catalyst design and synthesis. However, most of the works have focused on increasing the surface area to achieve a higher current, which can sometimes hinder the analysis on intrinsic catalytic activity of the material. Therefore, with respect to the catalyst activity towards HMF oxidation reaction (HMFOR), it is also important to compare the current density normalized by the electrochemical active surface area (ECSA), while taking account the selectivity of the product. In addition to surface modification or surface engineering of the catalyst, the bulk material of the catalyst also deserves attention. Recently, nickel-based core-shell type catalysts have been synthesized and shown superior performance in oxygen evolution reaction (OER) for water splitting. [23-25] For the HMFOR, since the oxidation state of Ni is key to the reactivity and selectivity, a catalyst with more Ni content available for oxidation can improve the reaction rate. This leads us to believe the role of bulk composition should also be considered for advanced catalyst design.

In this work, Ni-P catalyst is synthesized by cathodic Ni plating on thin Ni-deposited carbon paper substrate (NiP@Ni/C), and it is found that this catalyst is highly active for the HMFOR towards FDCA formation with an excellent oxidation charge storing capacity at low applied potential of 1.42V vs reversible hydrogen electrode (RHE), which is spontaneously reactive with HMF to form the final product FDCA at open circuit condition. The ECSA-normalized current density is superior to other Ni-based catalysts including thin (1-2 nm) and thick (200 nm) Ni-deposited carbon paper (NiC), surface oxidized Ni-deposited carbon paper

(NiOOH/Ni/C), and surface oxidized nickel foam (NiOOH/NF). NiP@Ni/C also has the highest Faradaic efficiency compared to the other catalysts, which reaches above 99% at the end of the conversion.

2. Experimental

2.1.Materials and chemicals

Electrochemical experiments were performed in a conventional H-type electrolytic cell (Corrtest). The membrane was Fumasep anion exchange membrane (Fumatech). The reference electrode (Corrtest) was Ag/AgCl electrode (3M KCl with saturated AgCl, Sigma Aldrich), and the counter electrode was Pt foil (Corrtest) in the three-electrode setup. The working electrodes substrates were nickel foam (Fuel Cell Store) and Freudenberg carbon paper (Fuel Cell Store) for deposition of Ni-based catalyst material. Chemical precursors NaH2PO2·H2O (Fisher Scientific) and Ni(NO3)2·6H2O (99%, Acros Organics) were used for Ni-based catalysts deposition. Electrode substrates were cleaned by ethanol, hydrochloric acid (Fischer Scientific) and RO water before catalyst deposition. RO water was used to clean the catalysts before an after each experiment. Electrolyte was 1M KOH (Sigma Aldrich) and H-cell was stored in 1M NaCl (Sigma Aldrich). Reaction chemicals for HPLC calibration included HMF (99%, Sigma Aldrich), FDCA (97%, Sigma Aldrich), HMFCA (98%, Cayman Chemicals), DFF (98%, TCI America) and FFCA (98%, TCI America). HPLC mobile phase was prepared from ammonium formate (99%) and methanol (Fisher Scientific).

2.2.Synthesis

NiOOH/NF was synthesized from commercial nickel foam via a pulse treatment of 30 cycles including 5 seconds of cathodic step (400 mA) and 15 seconds of anodic step (400 mA), finishing with a prolong anodic step of 300 seconds. The product shows a black colour on the nickel foam which consists of multilayer nickel oxyhydroxide structure.

The synthesis of NiP@NiC consists of a combination of physical vapor deposition, electroreduction and electroless nickel plating. First, Freudenberg carbon paper was deposited with a thin layer of Ni (1-2 nm) by electron-beam physical vapor deposition (Ni/C, thin). The Ni/C (thin) was rinsed with ethanol, 1 N hydrochloric acid solution and RO water before the backside of the carbon paper was masked by Kapton tape. Then the substrate was held by an electrode holder and submerged in a 100 ml of 0.5 M NaH2PO2 + 0.1 M Ni(NO3)2 solution. Subsequently, electroreduction was initiated by 15 LSV (0.3 V to -1 V vs. Ag/AgCl at 5 mV s^{-1}) in this solution

with a three-electrode setup (Ag/AgCl as reference electrode and Pt foil as counter electrode). Afterwards, the carbon paper was rested in the solution for < 0.5 h to allow continued electroless deposition of Ni P alloy.

Parameters that were controlled during the EN plating process include pH, solution composition, temperature, and bath loading. The deposition process was kept at room temperature. The bath loading was selected to be a lower end of the recommended level as 1 cm2 per 100 ml. The plating solution was discarded after 5-7 uses before big deviation occurred to the pH and concentration. NiOOH/NiC was synthesized through pulse treatment same as NiOOH/NF except that it was on thick NiC sample and the magnitude of the current in both cathodic and anodic steps was 100 mA.

2.3.Characterization

Ultra-high-resolution field emission scanning electron microscopy (Hitachi, Cold FE SU-8000 SEM) at 30 kV voltage was used to look at the morphology of the catalyst surface and subsequently energy-dispersive X-ray spectroscopy (EDX) was used to investigate the elemental composition of the catalysts. The as-prepared and post-experiment catalysts were inspected by X-ray photoelectron spectroscopy (Thermo-Scientific, K-Alpha XPS apparatus) with an Al Kα source for indication of oxidation state and bonding present on the catalyst surface. Bruker Discover D8 – 2D VANTEC 2000 X-ray diffractometer (XRD) with Co Kα source was utilized for crystal structure analysis. Transmission electron microscopy (TEM) was performed via Talos F200X G2 S/TEM. Soft X-ray Microcharacterization Beamline (Canadian Light Source, SXRMB) was used for X-ray adsorption spectroscopy (XAS) under room temperature on identification of atomic environment and oxidation states. Calibration on XAS was done with Ni foam as standard reference sample. Inductively coupled plasma optical emission spectroscopy (ICP-OES) was performed with Thermo Fisher iCAP 6000 series for Ni (231.6 nm) and P (213.6 nm) detection and quantification on deposited Ni-P catalysts.

2.4.Electrochemical Experiments

Linear sweep voltammetry (LSV) shows the potential window of the desired reaction. In this case, the potential window for the HMFOR is mainly between the surface oxidation of Ni^{2+} and the oxygen evolution reaction (OER). Chronoamperometry (CA) experiment is a standard method to investigate the electrochemical performance of the catalysts in reaction condition. Cyclic voltammetry (CV) was used to study the potential window, reaction reversibility and find

the electrochemical active surface area (ECSA) of a catalyst. ECSA was performed in 1 M KOH solution with scan rates from 1 to 50 mV s^{-1} with the range ± 50 mV around 1.036 V RHE. Electrochemical impedance spectroscopy (EIS) was measured by Autolab potentiostat and was used to find the system resistance (Rs) and charge transfer resistance (Rct) of the reactor setup with a catalyst. Open circuit potential (OCP) test was performed for monitoring spontaneous charge transfer from catalysts to HMF molecules in the anode.

To convert reference electrode to RHE potential, the following Equation 1 was used,

$$E(RHE) = E_{Ag/AgCl} + E^0_{Ag/AgCl} + 0.059 \times pH \quad (1)$$

2.5.Product Analysis

A Thermo Ultimate 3000 high performance liquid chromatography (HPLC) with a Thermo Acclaim 300 C18 column was used for liquid product detection and quantification for EC tests. Ammonium formate (5mM) and methanol at a volumetric ratio of 9:1 was used as the mobile phase. For liquid product examination from HMFOR tests, 1 ml of liquid sample was added to 9 ml of RO water and then further diluted with 40 ml of 0.1 M KOH. It was filtered using a syringe filter and filled in a 2 ml vial, then placed in the HPLC autosampler.

The calculations of FDCA yield, Faradaic efficiency and HMF conversion are given by the following Equation 2 – 4 respectively:

$$yield_{FDCA} = \frac{\Delta N_{FDCA}}{-\Delta N_{HMF}} \times 100\% \quad (2)$$

$$FE_{FDCA} = \frac{6F \times N_{FDCA}}{Q} \times 100\% \quad (3)$$

$$Conversion_{HMF} = \frac{\Delta N_{HMF}}{N_{HMF,initial}} \times 100\% \quad (4)$$

Where F is the Faraday number (96485 C mol-1), N is the number of moles, and Q is the charge.

3. Results & Discussions

3.1.Catalyst Characterization

Ni-P catalyst is synthesized by consecutive cathodic linear sweep voltammetry (LSV) scanning on a thin (< 2 nm) nickel-deposited carbon paper substrate (denoted as Ni/C (thin)) in an electroless plating solution. Previous studies have used similar potentiodynamic deposition method based on the electroless co-deposition of Ni and P. [26] The Ni/C (thin) is obtained by physical vapor deposition of Ni nanoparticles on carbon paper substrate. The as-prepared catalyst is denoted as NiP@Ni/C while the catalyst after cyclic voltammetry to oxidative potentials acquires an oxidized surface, becoming NiOOH/NiP@Ni/C (Figure 1a). NiOOH/Ni/C is

synthesized by a pulse treatment oxidation on the thick Ni/C substrate with 200 nm Ni deposition thickness. NiOOH/NF is also prepared by a pulse oxidation but on nickel foam.

The surface illustrations by scanning electron microscopy (SEM) of Ni/C (thin), NiP@Ni/C, NiOOH/NiP@Ni/C, Ni/C (thick) NiOOH/Ni/C and NiOOH/NF are shown in Figure 1d-i at various magnifications. It is clear that the Ni nanoparticles do not cover the carbon paper in Ni/C (thin), and after the deposition of Ni-P catalyst on top, a new layer of deposited material can be seen on both as-prepared and surface oxidized catalysts. For Ni/C thick and the surface oxidized one, they do not show any noticeable difference in morphology. The cracks on some catalyst surfaces are due to drying before taken for imaging. From energy dispersive X-ray analysis (EDX) on the catalyst surface and cross-section (Figure 1b,c), Ni, O and P are seen in the bulk with uniform distribution while Ni and O are rich on the surface layer after surface oxidation and HMFOR. The surface phosphorus content is decreased after HMFOR, likely being released to the electrolyte, while cross-sectional scan shows that P remains in the deeper layer and the bulk of the catalyst (Figure S2).

As-prepared NiP@Ni/C has a mostly amorphous coating layer of Ni-P as found in Figure 2 by X-ray diffraction (XRD) analysis when excluding the carbon substrate signals. Specifically, by comparing with Ni foam (PDF 00-004-0850) and carbon paper substrate, Ni-P catalyst did not show prominent nickel-related crystallinity in the mid 2θ range (Co Kα source) from 40° to 100° (Figure S3). From the entire samples of as-prepared and post-HMFOR Ni-P catalysts, signals in the lower diffraction angel indicate that a portion of the catalyst turned into nickel oxide/hydroxide (PDF 01-089-7111). The broad peak at 30° is the graphite-2H (PDF 04-020-4354) from the carbon substrate, while five other peaks between 40° and 100° are attributed to the substrate. Besides, when comparing as-prepared to post HMFOR Ni-P catalyst powders, slight differences appear at lower diffraction angles suggesting the potential formation of some nickel phosphorus oxide in the subsurface layer and the bulk, such as NiP4O11 (PDF 04-011-1683). This reveals that when oxidized in alkaline solution, the catalyst surface turns to nickel hydroxide and oxide species, while nickel phosphorus oxide species remain in the sub-layer and the bulk of the catalyst.

High resolution transmission electron microscopy (HR-TEM) is carried out to inspect the catalyst and Figure 3a, b shows that the as-deposited Ni-P is an amorphous coated layer on the carbon paper, which aligns with the XRD results. The same amorphous electrodeposited layer has been obtained by previous studies preparing Ni- or Co- and P-containing catalysts. [27, 28] High-

angle annular dark-field imaging (HAADF) in combination with EDX analysis in Figure 3c reveals the uniform distribution of Ni, P and O elements, which agrees with the SEM-EDX result. Post HMFOR catalyst sample, on the other hand, shows that Ni and O are more abundant on the catalyst surface while some P is depleted from the surface layer with the rest remaining in the bulk (Figure 3f). This supports the SEM analysis and confirms that the active surface component is oxidized Ni species.

The surface composition is verified by X-ray photoelectron spectroscopy (XPS) survey where Ni 2p, P 2p and O 1s signals are observed (Figure S5). As shown in deconvoluted high resolution XPS in Figure 4a, the as-prepared NiP@Ni/C catalyst has a clear Ni 2p3/2 peak at 853.5 eV, corresponding to nickel species in Ni-P solution, and also a Ni0 2p3/2 peak at 852.1 eV, representing a small amount of pure Ni in the catalyst. [18, 29] Two other 2p3/2 peaks of Ni^{2+} in Ni(OH)2 and Ni^{3+} in NiOOH formed by oxidation, are also clearly seen as peaks at 855.7 eV and 857.2 eV. [30] The 2p3/2 satellite peak and the 2p1/2 peaks are also identified at higher binding energies. Same peaks are present for surface oxidized NiOOH/NF, but Ni^{3+} is not found on nickel foam (Figure S6a, b), which verifies Ni^{3+} being the active site on Ni-P catalyst similar to NiOOH/NF. Figure 4b shows the P 2p region of the as-prepared Ni-P catalyst where a typical P 2p3/2 signal is located at 130.0 eV, along with a partially oxidized P 2p3/2 located at 133.3 eV. [29, 31] The Ni region XPS scans for Ni-P catalyst after CV and HMFOR are compared in Figure 4c, where the Ni 2p3/2 peak becomes negligible and the Ni^{2+} and Ni^{3+} 2p3/2 peaks are more prominent, signifying a surface oxidation of nickel species on the catalyst, which verifies the existence of nickel oxyhydroxide and nickel hydroxide on the surface. These results also correspond well to the SEM results mentioned previously. In Figure 4d, the P 2p regions show no obvious signal, meaning that the surface is phosphorus depleted, which indicates that the active sites are oxidized nickel species instead of the doped P species as the surface P has leached into the alkaline electrolyte. This agrees with previous literature that have shown a decrease of P content on the catalyst surface after either OER or HMFOR, where a metal oxide layer is formed. [19, 24, 25, 31, 32]

X-ray adsorption spectroscopy (XAS) gives additional information on composition and structure of the catalyst. From X-ray adsorption near edge spectra (XANES) shown in Figure 5a, the pre-edge feature of Ni is barely present before the Ni K edge for both as-prepared and surface oxidized Ni-P catalysts. This indicates that the change in oxidation states of Ni species in these

samples does not largely affect the coordination environment of central Ni atom. The lower intensity of the NiP@Ni/C at the rising edge is a result of higher symmetry, likely due to the deposited amorphous nickel phosphorus layer. [33] The rising edge at around 8345 eV (E0 from second derivative) demonstrates that the Ni species near the surface of the Ni-P catalyst is less oxidized than most of the other samples, while the surface Ni species in oxidized NiOOH/NiP@Ni/C obtains higher oxidation state. This wider oxidation window is believed to be a result of the various bonding orientations in the Ni layer that helps to contain an extended average Ni oxidation state at various applied potentials. [34] Figure 5b as a result from Fourier-transform extended X-ray absorption fine structure spectra (EXAFS) illustrates the similarity in bonding conditions among Ni catalysts without the presence of phosphorus, where Ni-Ni is the dominant bonding condition, with a first shell Ni-Ni peak at 2.49 Å (Figure S7). [35] The as-prepared and the oxidized Ni-P catalysts on the other hand reveal shorter bonds in the first and the second shells, but no significant long-range ordering, illustrating an amorphous structure with only short-range ordering within the first two shells of neighboring atoms. [36] As peak fittings shown in Figure 5c, the first peak at 2.06 Å is attributed to Ni-O bond, and slightly wider peak indicates the existence of different bonding conditions with oxygen atoms in the catalyst. [35] The peak near 3.11-3.26 Å is an evidence of Ni-Ni/Ni-P bonds. [37] Figure 5d-f illustrate the k space, real part of R space and the backward Fourier transform q space of the fitting, showing the Ni-O scattering frequency contributes to the first peak while the Ni-Ni and Ni-P scattering paths contribute to the second peak. Fitting details can be found in Table S2, supplementary information. Figure 5b also displays the shift to more contracted Ni-O peak in the case of NiOOH/NiP@Ni/C, while only first shell Ni-Ni peak intensity is slightly changed for NF after surface oxidation treatment. This agrees with the XPS result on the increase of Ni oxidation state, and it also reveals the creation of active Ni^{3+} in the sublayer structure of Ni-P catalyst after oxidation (Scheme 2), however, only surface modification with limited depth occurs on NiOOH/NF. This feature of Ni-P catalyst is a result of the activation of amorphous transition metal oxide doped with p-block materials and eventually leads to active catalysis supported by the bulk of the catalyst, similar to what has been observed for the OER. [38]

3.2.Ni Active Site and Mechanism

It is known from previous studies that the active site for the HMFOR is the nickel hydroxide-oxyhydroxide complex under applied anodic potential, where the Ni^{2+} species can be

oxidized to Ni^{3+}, allowing the spontaneous reaction between the higher oxidation state nickel and the organic molecule. [17, 34, 39] A series of electrochemical experiments verify that Ni^{3+} is the main active site of the plated Ni-P catalyst for the HMFOR. Although Ni^{3+} is present on the active catalyst surface, the mechanism for charge transfer is different when bulk composition varies. During the forward scan in the cyclic voltammetry (CV) in 1M KOH electrolyte without HMF, the ECSA-normalized current density increases rapidly after 1.36 V on NiP@Ni/C, which is attributed to the nickel oxidation from Ni^{2+} to Ni^{3+} (Figure 6a). [13, 40] This onset potential is slightly more positive on the Ni foam (1.38 V) and thick Ni/C (1.37V) (Figure 6c, e). The much larger Ni oxidation peak on NiP@Ni/C indicates a large amount of charge transferred to and stored not only on the surface but also in the bulk of the catalyst. In the presence of HMF, forward scan (into more anodic potentials) on all these catalysts shows the same onset potential as the Ni oxidation onset potential without HMF, while the rising current density shortly after onset follows the same positive slope as the Ni oxidation peak, meaning that the Ni oxidation takes place prior to the HMFOR and the latter relies on the former. This verifies that the oxidation reaction of HMF molecule requires the presence of Ni^{3+}, so it remains insignificant before that Ni^{3+} becomes dominant on the catalyst surface. By subtracting the forward scan of HMF absent CV from the HMF present one on NiP@Ni/C, the positive difference in current density begins to show after 1.45 V, while peaking around 1.68 V (Figure 6b). Once the potential becomes more anodic than 1.70 V vs RHE, the OER starts to outperform the HMFOR in this experimental condition. In the same plot, the difference of backward scans (also from HMF scan minus without HMF scan) shows two positive peaks around 1.38 V and 1.06 V. The presence of only positive peaks instead of negative ones indicates that there are charge transfer processes other than simple nickel redox of the electrode. The peak at higher applied potentials corresponds to oxidation of HMF on Ni^{3+}, which is at maximum around 1.38 V and then starts to decline when Ni^{3+} begins to be reduced on the catalyst surface. Moreover, the distinct peak at lower potential which corresponds to nickel reduction implies the partially reduced nickel in the presence of HMF. This confirms the spontaneous charge transfer from the oxidized nickel species to the electrolyte containing HMF proposed by Fleischmann et al., which we posit it is the main pathway for the HMFOR on NiP@Ni/C. [41] This indirect charge transfer via the Ni^{2+} and Ni^{3+} mediation agrees with previous studies on nickel catalysts for many types of alcohol oxidations. [42-46] In a recent study that demonstrates difference between the direct and indirect oxidation processes, it is reported that the

direct oxidation, or potential-dependent oxidation, only occurs at higher applied potential where a proposed hydride transfer is responsible for the organic molecule oxidation. [42] The same effect is of a much smaller extent in the case of NiOOH/NF (Figure 6d), where the first positive peak due to the direct (or potential-dependent) charge transfer on catalyst surface—happening at higher applied potentials—is the major charge transfer process. This direct charge transfer process is facilitated with stirring, since the nickel foam substrate has a 3D porous structure that allows electrolyte to pass through. Without stirring the electrolyte, the NiOOH/NF shows much more limited current, where the dominant reaction can be the indirect charge transfer for the HMFOR (Figure 6c). For thick Ni/C catalyst (Figure 6f), there is only one major peak in the backward scan difference at high potentials, which appears to be smaller than the forward difference peak. This indicates a less kinetically favoured direct charge transfer process with Ni^{3+} on this catalyst surface. Comparing the three CV tests and their differences in forward and backward scans, the potential window for the HMFOR on NiP@Ni/C is the widest. This is due to the electrochemically active bulk material that enables the catalytically active Ni^{3+} surface to selectively perform the HMF oxidation at both lower potentials (more negative Ni^{3+} reduction potential) and higher potentials (less selective for the OER). The broader window also means that once the active component of NiP@Ni/C is oxidized, the HMFOR can occur at a much lower potential (1.25~1.40 V). This understanding opens a new way of HMF conversion in alkaline electrolyte with lower applied potentials, hence reducing the operating costs.

A stepwise reaction scheme for the HMFOR is shown in Scheme 3. The first step involves the nickel species oxidation to NiOOH under alkaline environment (R1), meanwhile the HMF molecule from the electrolyte is adsorbed on the catalyst surface (R2) before spontaneous reaction with the Ni^{3+} species, producing oxidized biomass intermediate and the reduced active site as Ni^{2+} in Ni(OH)2 (R3). [42] Additionally, it is also possible to have direct oxidation of adsorbed HMF via Ni^{3+} under higher applied potentials (R4). [34] Although some studies report that Ni^{2+} could be active for oxidation of organic molecule (R5), it can be seen in the CV that the extent of such reaction pathway remains insignificant if any. [34] From the three CV results, it is noted that after oxidation peak of Ni, there is a plateau region where the HMFOR experiences mass transfer limitations. [42] Increasing the HMF concentration in 1M KOH electrolyte yields a higher current density at the plateau region, but the increase in current density before or near the onset of Ni^{2+} oxidation is minimal (Figure S8). This again proves that the catalysis mainly happens on Ni^{3+}

active site. In addition, it also reveals that the reaction is initially restricted by Ni oxidation (R1) which provides the necessary active surface for the oxidation of HMF after the onset of Ni^{2+} oxidation, but later the process is predominantly limited by Ni^{3+} reaction with HMF (R3) at higher applied potentials before the OER takes place. Bode phase plots from electrochemical impedance spectroscopy (EIS) shows the appearance of new peaks at a low frequency between the applied potential of 1.38 V and 1.48 V with HMF, signifying that the onset for the direct HMFOR is after 1.38 V where the nickel oxidation state is $^{3+}$ for both NiP@Ni/C and NiOOH/NF (Figure S9a, c). This agrees with previous studies showing that the oxidation of surface Ni^{2+} to Ni^{3+} is quick and the subsequent reaction between Ni^{3+} and the adsorbed organic component is the rate determining step. [42] When the anode surface is reduced by the spontaneous reaction with HMF molecules, EIS at the open circuit potential or smaller applied potential can show the kinetics of the reaction system since any remaining Ni active site accessible to the electrolyte can still cause the HMFOR and be reduced, so the catalyst partially remains active under a smaller applied potential. From the appearance of Ni oxidation in Bode plots at the open circuit potential (OCP, 1.30 V) on NiP@Ni/C with HMF (Figure S9b), it is deduced that the catalyst is still releasing positive charge to the electrolyte such that there remains electron transfer between the solid-liquid boundary. A similar but smaller peak is found with reduced NiOOH/NF at the OCP in HMF (Figure S9d). In the absence of HMF, partially reduced NiP@Ni/C again shows a peak that corresponds to nickel oxidation while there is no obvious peak under the OCP on NiOOH/NF without HMF. For NiP@Ni/C, 1.30 V is still above the Ni^{3+} reduction peak potential (~1.10 V), therefore it is evident that the bulk of the electrode remains mostly Ni^{3+}, which is active for spontaneous HMFOR. Meanwhile for NiOOH/NF, the OCP (0.93 V) is lower than the Ni^{3+} reduction peak potential (~1.31 V), therefore no obvious Faradaic process takes place, and both the surface and the bulk remain mostly reduced Ni. The amorphous nature of NiP@Ni/C widens the potential window for the existence of Ni^{3+} due to multi-facets and diverse bonding conditions, hence the catalytic activity at lower potentials.

3.3.Catalyst Performance

LSV from the OCP to the more anodic OER region (> 1.8 V) of the NiP@Ni/C in 1M KOH with 15 mM HMF is compared to LSV of thick NiC, NiOOH/Ni/C and NiOOH/NF (solid lines in Figure S10) using ECSA-normalized current density. To obtain the current-potential response of the OER background, the LSV of the same catalyst in 1M KOH without HMF is performed twice

consecutively, so that after the first scan the exposed Ni species is completely oxidized (dash lines in Figure S10). The onset potential of Ni-P catalyst for Ni oxidation and the HMFOR is shown to be smaller than the other catalysts from the LSV tests. Since LSV procedure measures the transient current response, stepwise chronoamperometry is carried out and polarization curves are plotted to verify the quasi-steady state current at each applied potential near the onset of Ni oxidation as shown in Figure 7c, which confirms the same observation from LSV results that the Ni-P catalyst has lower onset potential for the HMFOR. Tafel slopes extracted from the polarization curves confirm the higher activity for the HMFOR (33.4 mV dec-1) compared to the OER (67.2 mV dec-1) by Ni-P catalyst Figure 7d. It also shows that the other catalysts have similar Tafel slopes for the HMFOR and the OER, with lower exchange current density compared to Ni-P. This indicates that Ni-P has better selectivity for the HMFOR under competition against the OER and requires less applied potential to reach the same specific reaction activity.

Chronoamperometry test over the course of 30 minutes is conducted at 1.48V with 15 mM HMF to investigate the selectivity of the HMFOR. The results show that the Ni-P catalyst has the highest Faradaic efficiency of 90% towards FDCA (Figure 7a). The other catalysts without phosphorus content in the catalyst have more intermediates (HMFCA and FFCA) in comparison. The thin Ni/C catalyst with Ni nanoparticles does not generate a good amount of FDCA (< 37%) in 30 minutes, which is due to the low current density and lack of continuous charge transport to the active sites. On the contrary, given that the HMF to FDCA conversion is a six-electron transfer process, the high Faradaic efficiency towards the final product achieved by Ni-P catalyst with its high specific activity, demonstrates highly active surface and high specific charge transfer rate from the catalyst to the adsorbed HMF and intermediate molecules. Full conversion chronoamperometry test with 5 mM HMF at the same applied potential for Ni-P is performed (Figure 7b), and the electrolyte is processed by high performance liquid chromatography (HPLC) for product analysis (Figure S13). The results reveal the consistent high selectivity (>90%) towards FDCA over the whole conversion process, whereas the intermediates remain in the electrolyte are kept low. In fact, at short time experiments, Ni-P catalyst already achieved immediate high FE (above 80% in 5 minutes) towards FDCA, whereas the NiOOH/NF requires much longer time or more charge transferred (> 2 hours, or > 250 C) to reach a higher FE (Figure S15 and Figure S16). This indicates that Ni-P catalyst enables stable charge transfer to the adsorbed intermediates quickly enough so most of them become oxidized to the final FDCA before desorption from the

catalyst surface. The gradually decreasing total carbon balance is due to the degradation of HMF in alkaline environment into humin type products. [47, 48] Combining the 30-minute chronoamperometry with the previously mentioned stepwise chronoamperometry results in Figure 7c, the performance of NiP@Ni/C is superior to the other Ni catalysts, in both FDCA selectivity and specific activity, demonstrated by Faradaic efficiency and normalized current density, respectively, as plotted in Figure 7e. Stability tests repeated in one hour interval for 10 cycles (Figure 7g) show that the Ni-P catalyst can consistently perform HMFOR with high FE towards FDCA (> 90%). In each cycle, the initial anodic current density is evidence of Ni species oxidation in the electrode, whereas the later smooth current indicates a continuous oxidation of HMF molecules. The decrease of current density is due to the decrease of HMF concentration in the H-cell. Longer time range test also shows repeatable initial current density and the trend over the course of 20 hours (Figure S17). Ni^{2+}/Ni^{3+} redox couple is also shown to be recoverable from CV tests on NiP@Ni/C with and without the presence of HMF (Figure S18). These stability tests show consistency and durability of the synthesized Ni-P catalyst. The intrinsically faster kinetics regardless of the actual surface area is considered to be a result from the high charge storage ability of the bulk material. There is also evidence of faster kinetics on charge transfer shown by the EIS. By fitting the EIS Nyquist plot, the charge transfer resistance of the HMFOR on NiP@Ni/C is 13.0 Ω at 1.38V (Figure 7f), which is the lowest among the other catalysts (Table S3). The other two samples that have nickel deposited on carbon paper (Ni/C or NiOOH/Ni/C) demonstrate much higher charge transfer resistances of the HMFOR (45.4 Ω and 51.7 Ω). Since the active sites are nickel oxyhydroxide and their morphology is similar, the difference in electrochemical impedance is attributed to the lack of an oxidized Ni sublayer that supports the oxidation of HMF on the surface. The unique 3D structure of surface oxidized NiOOH/NF also facilitates the charge transfer on the active surface; thus, it yields a small charge transfer resistance for the HMFOR as well (14.1 Ω), but the porous nature of the foam material leads to a higher internal resistance.

3.4.Charge Storing in Ni-P Bulk

To investigate further the charge transfer phenomenon on NiP@Ni/C and other control catalysts, spontaneous HMF conversion test under open circuit condition is performed. The anode is first charged at 1.42 V vs RHE in 1M KOH for 10 minutes which is above the oxidation potential for Ni^{2+} but before the OER appears. This renders the surface of catalyst Ni^{3+} enriched, then 5 mM of HMF is added to the anolyte where Ni^{3+} spontaneously discharge into the electrolyte leading to

HMF conversion while the drop in the OCP is monitored for 1500 seconds. A trend is shown in Figure 8a on phosphorus-free samples, where thicker Ni layer leads to lower specific charge (50 nm and 200 nm NiOOH/Ni/C with 1.3 C mg^{-1} and 0.3 C mg^{-1} respectively, NiOOH/NF with only 0.01 C mg^{-1}), while Ni-P derived catalysts demonstrate higher values (> 1.7 C mg^{-1}). This supports the hypothesis that only some surface Ni layers get oxidized under Ni^{2+} oxidation potential instead of the whole bulk electrode when there are no other elements or types of bonds present within the bulk. The specific charge storage ability for catalysts that contain the phosphorus, is higher than the assumed 1 electron transfer for turning Ni^{2+} to Ni^{3+}. This means that the entirety of Ni-P catalyst is capable of accepting and storing more charge than the amount needed to raise all Ni atoms to one higher oxidation state. The composition analysis on the catalyst by inductively coupled plasma optical emission spectroscopy (ICP-OES) is used to obtain the phosphorus and nickel amount. During the OCP test on Ni^{3+} surface with HMF, the potential reading on the anode for the oxidized Ni-P catalyst is maintained at 1.30 V until the end of the discharge process (Figure 8b), indicating a sustained high oxidation state for surface Ni species. On the contrary, for other catalysts, despite the support material (carbon paper or nickel foam) and thickness of Ni layer, the OCP quickly drops to around 0.90 V which is the Ni^{2+} equilibrium potential, meaning that the surface layer of Ni^{3+} is not maintained for long. Consequently, the electrolyte sampled at the end of 1500 s of the OCP test, shows the most FDCA selectivity (76%) on the oxidized NiP@Ni/C while for the other catalysts, the amount of HMF conversion to FDCA is greatly limited by the amount of charge being transferred (Figure 8c). As a result of the higher oxidation states of nickel species in the bulk of the Ni-P catalyst, a higher degree of conversion of HMF molecules adsorbed on the surface of the catalyst is achieved. The lack of continuous charge transfer from the deeper layer of the catalyst lowers the possibility for this full 6-electron conversion. At stable OCP, the NiOOH/NF only reaches ~50% charge efficiency but Ni-P passes up to 84% of the stored charge towards FDCA formation (Figure S11). High resolution etching XPS profiles on as-prepared and used NiP@Ni/C reveal that there are more bonding between nickel and phosphorus, as the signal intensities on both Ni2p and P2p spectra increase with etching levels (Figure 9). Therefore, the good conductivity of Ni-P catalyst and its charge storing ability enable the continuous facile conversion of alcohol and aldehyde groups on the HMF molecules. This resembles the core-shell effect on some transition metal catalysts with enhanced electrochemical performance that were previously studied. [24, 49, 50] Additionally, the uniformity of Ni-P in the bulk also enhances the

possibility for easy charge distribution, that results in effective HMFOR on the surface, and might introduce some core-shell synergistic effect between NiOOH/oxidized Ni surface and the bulk layer. [21]

4. Conclusion

In summary, the Ni-P catalyst is successfully synthesized via a cathodic Ni plating on Ni-deposited carbon paper substrate (NiP@Ni/C) without binder materials. Experiments show that the NiP@Ni/C catalyst possesses an excellent oxidation charge storing capacity, where the deposited Ni species remains electrochemically active even in the bulk layer of the electrode, in addition to conventional surface redox reaction on Ni^{3+} active sites. This functional core structure of the Ni-P catalyst continuously supports spontaneous HMF conversion into FDCA at low applied potential and under open circuit condition before the OER takes place. Moreover, the specific activity is superior compared to other Ni-based catalysts mainly because of the electrochemically active Ni-containing core. The facile charge transfer for both electrode bulk and surface oxidation enables the NiP@Ni/C to give a high FDCA Faradaic efficiency throughout the chronoamperometry test where it reaches 97% at the end of the conversion, while achieving a stable FDCA production of 10 repeated cycles. This work sheds light on the role of bulk material in the HMFOR and brings consideration on electrode design for charge storage assisting surface catalysis.

Author Contributions

Roger Lin: The first author who did most of the experiments and wrote the draft of this paper.

Mahdi Salehi: The second author who synthesized catalysts and performed physical characterizations.

Jiaxun Guo: The third author who helped conceptualize and investigated the work.

Ali Seifitokaldani: The corresponding author who supervised, reviewed the work and acquired funding.

Funding Sources

This work was supported by Fonds de recherche du Québec – Nature et technologies (FRQNT) Master Scholarship, FRQNT New Researchers Fund (2021-NC-283234), NSERC Discovery Grant (RGPIN-2020-04960), and Canada Research Chair (950-23288).

ACKNOWLEDGEMENT

The synchrotron XAS was done at the Canadian Light Source (CLS) in Saskatchewan, Canada. Authors acknowledge Mohsen Shakouri, Qunfeng Xiao, and Alisa Paterson at CLS for their help during the XAS measurements. We thank Dr. Xue-Dong Liu at the Facility for Electron Microscopy Research of McGill University for help in microscope operation and data collection.

Conflict of Interest

The authors declare no conflict of interest.

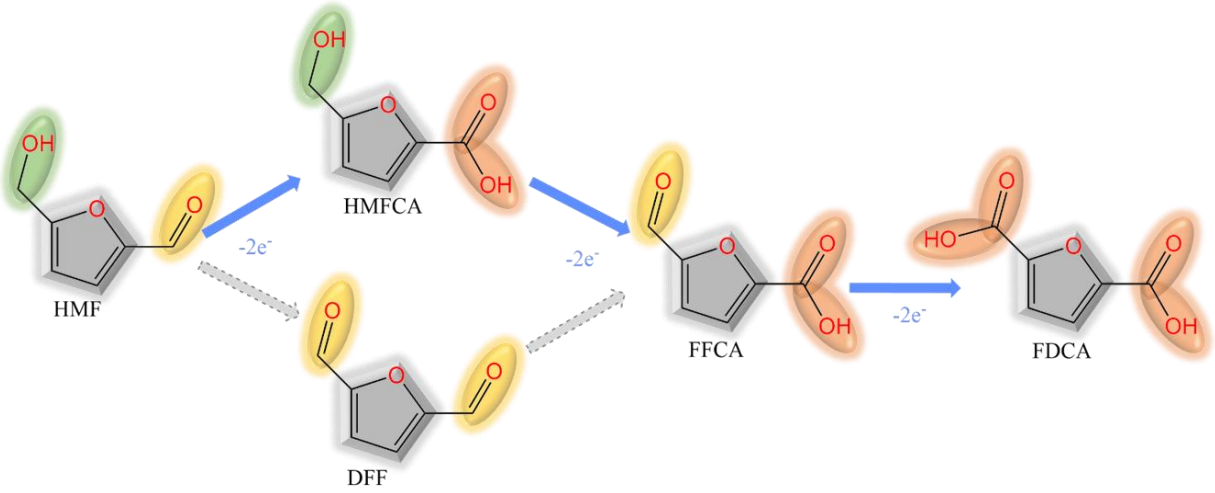

Scheme 1. HMF oxidation reaction route and intermediates towards FDCA as the final product

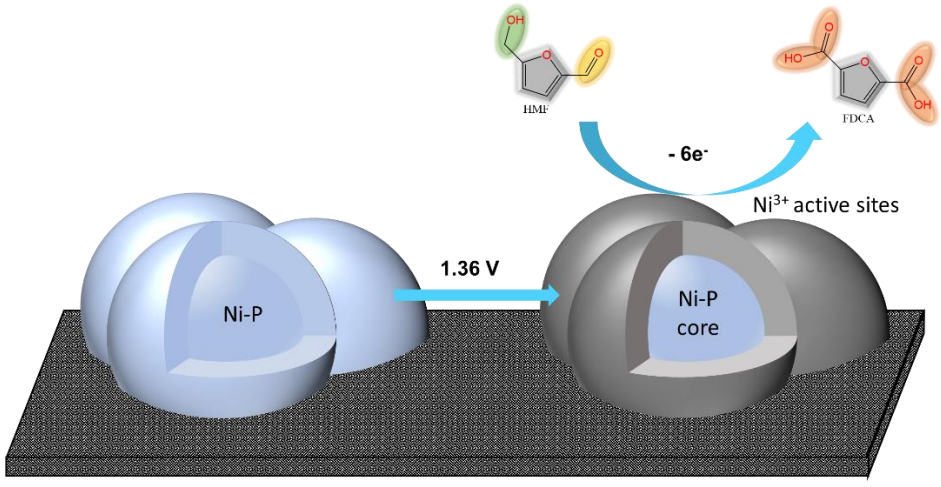

Scheme 2. HMF oxidation reaction on surface oxidized NiP@Ni/C catalyst

$$OH^- + Ni(OH)_2 \xrightarrow{-e^-} NiOOH + H_2O \quad \text{(R1)}$$

$$HMF_{bulk} \longrightarrow HMF_{ads} \quad \text{(R2)}$$

$$HMF_{ads} + NiOOH \xrightarrow{RDS} Ni(OH)_2 + intermediates \quad \text{(R3)}$$

$$HMF_{ads} + OH^- \xrightarrow{-e^-,\ NiOOH} intermediates \quad \text{(R4)}$$

$$HMF_{ads} + OH^- \xrightarrow[minimal]{-e^-,\ Ni(OH)_2} intermediates \quad \text{(R5)}$$

Scheme 3. HMF reaction steps on Ni(OH)2/NiOOH catalyst in aqueous alkaline condition

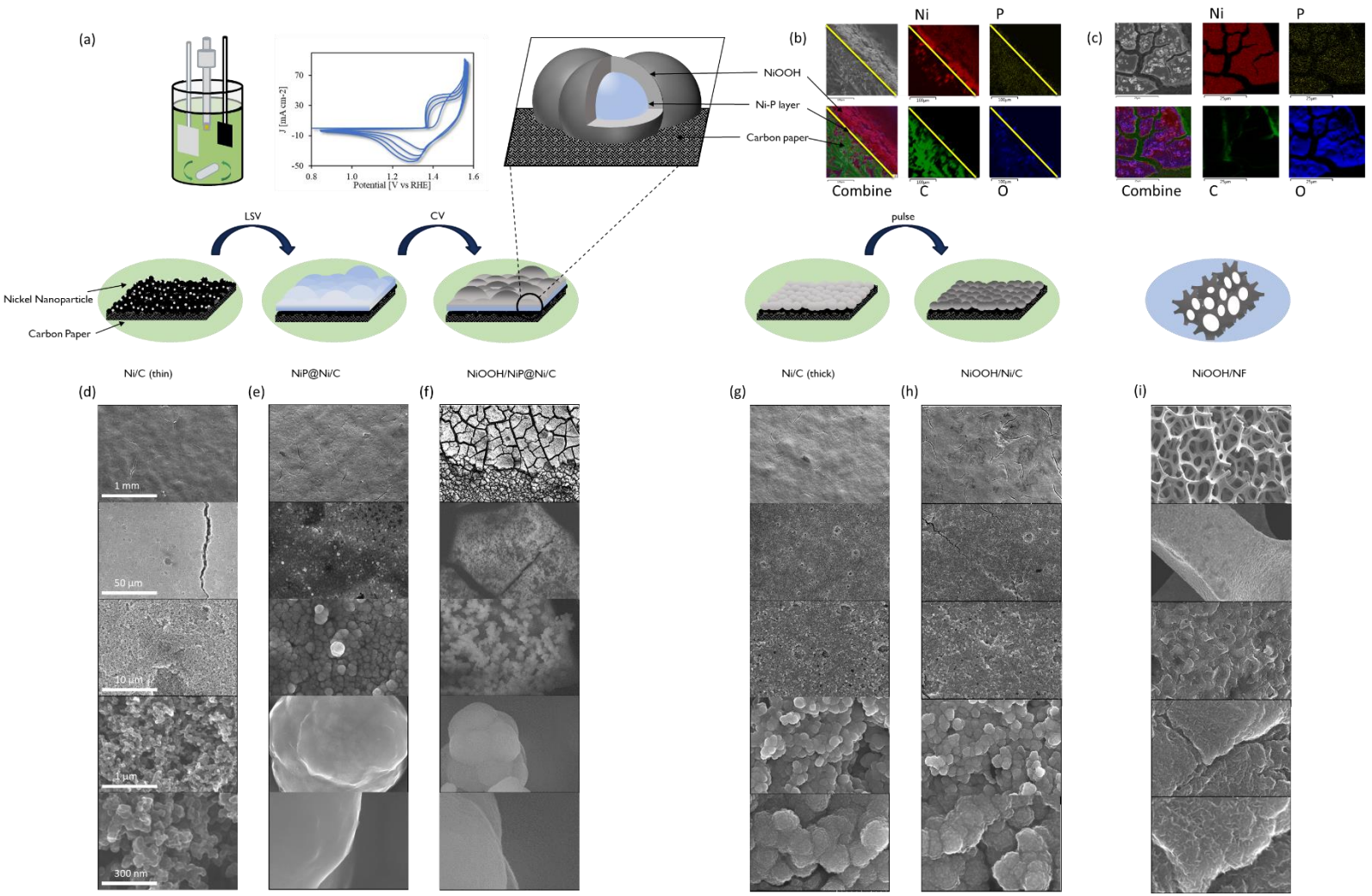

Figure 1. a) Catalyst preparation, illustration and scanning electron microscopy (SEM) of surface oxidized Ni-P catalyst with energy dispersive X-ray spectroscopy (EDX) for elemental mapping on b) cross section and c) top view. Following SEM images showcase d) carbon paper with nano-layer nickel as substrate (Ni/C thin); e) NiP@Ni/C as-prepared; f) surface oxidized NiOOH/NiP@Ni/C; g) thick nickel layer on carbon paper (Ni/C); h) surface oxidized NiOOH/Ni/C; i) surface oxidized nickel foam (NiOOH/NF).

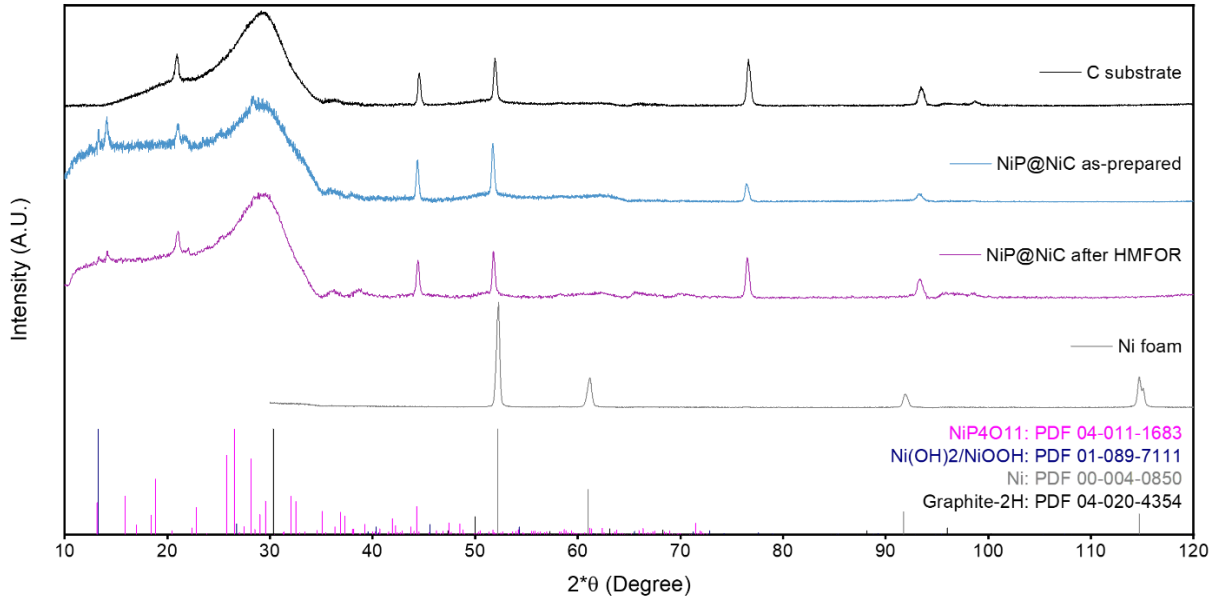

Figure 2. X-ray diffraction analysis on carbon paper substrate, Ni foam, and powders from as-prepared NiP@Ni/C and post HMFOR NiP@Ni/C.

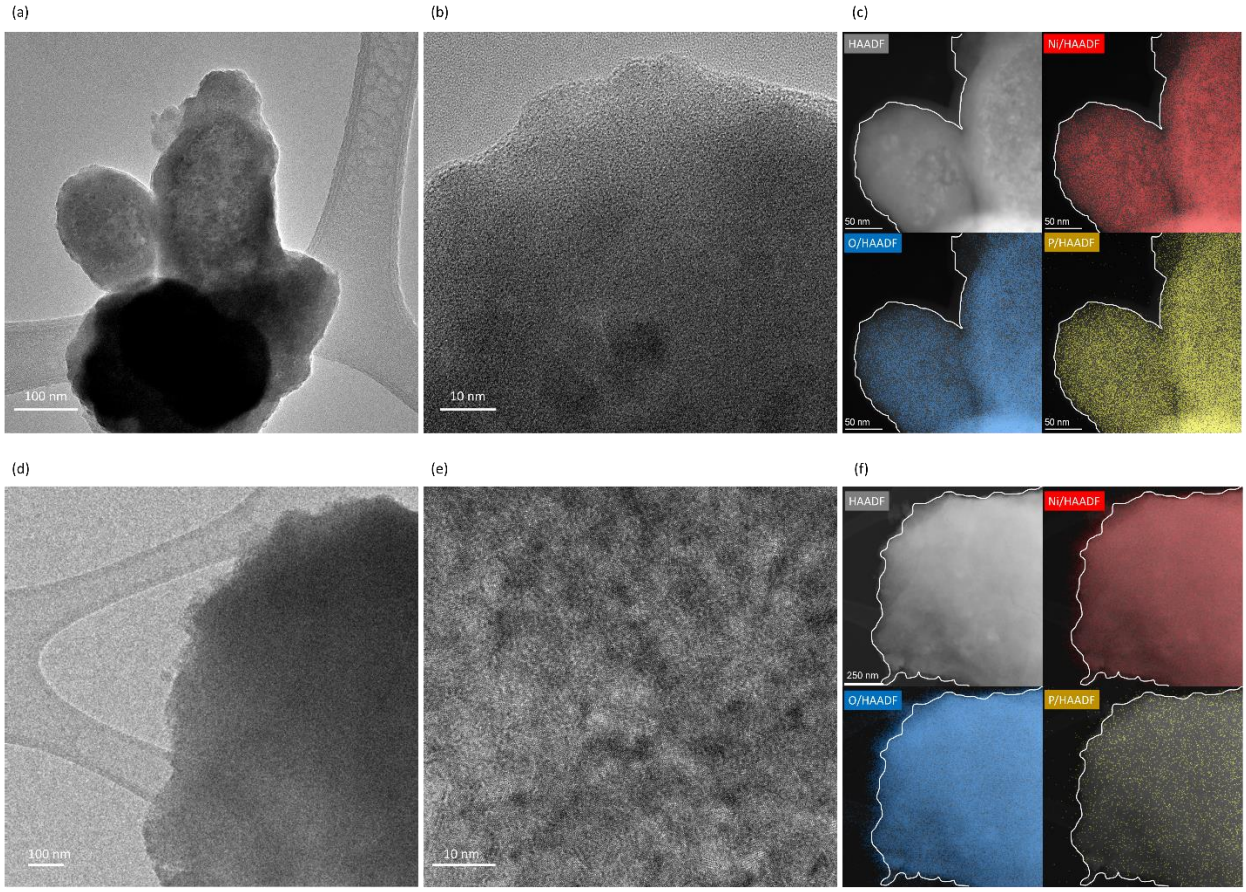

Figure 3. a-b) High resolution transmission electron microscopy (HR-TEM), c) High-angle annular dark-field imaging (HAADF) and energy-dispersive X-ray spectroscopy (EDX) on scrapped as-prepared Ni-P catalyst; d-e) HR-TEM, f) HAADF and EDX on scrapped catalyst after HMFOR.

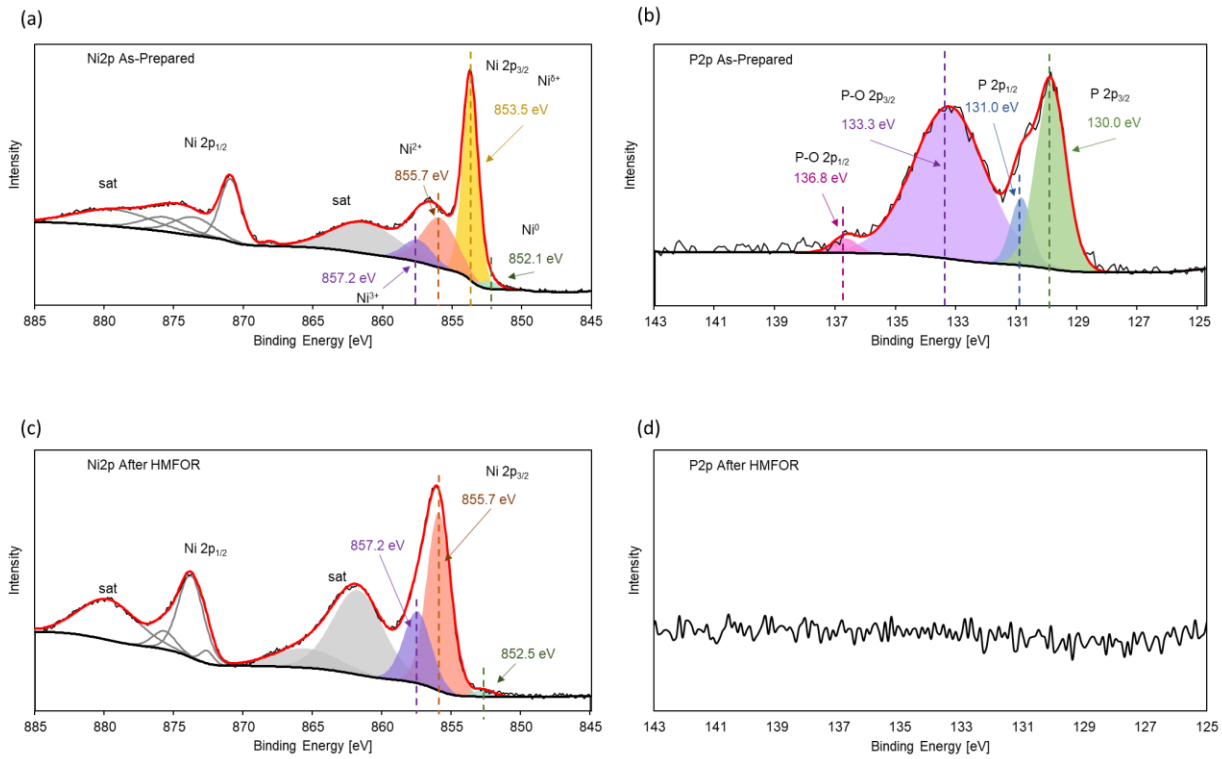

Figure 4. High resolution X-ray photoelectron spectroscopy of as-prepared NiP@Ni/C on a) Ni 2p spectra; b) P 2p spectra; XPS of NiP@Ni/C after HMFOR on c) Ni 2p spectra; d) P 2p spectra.

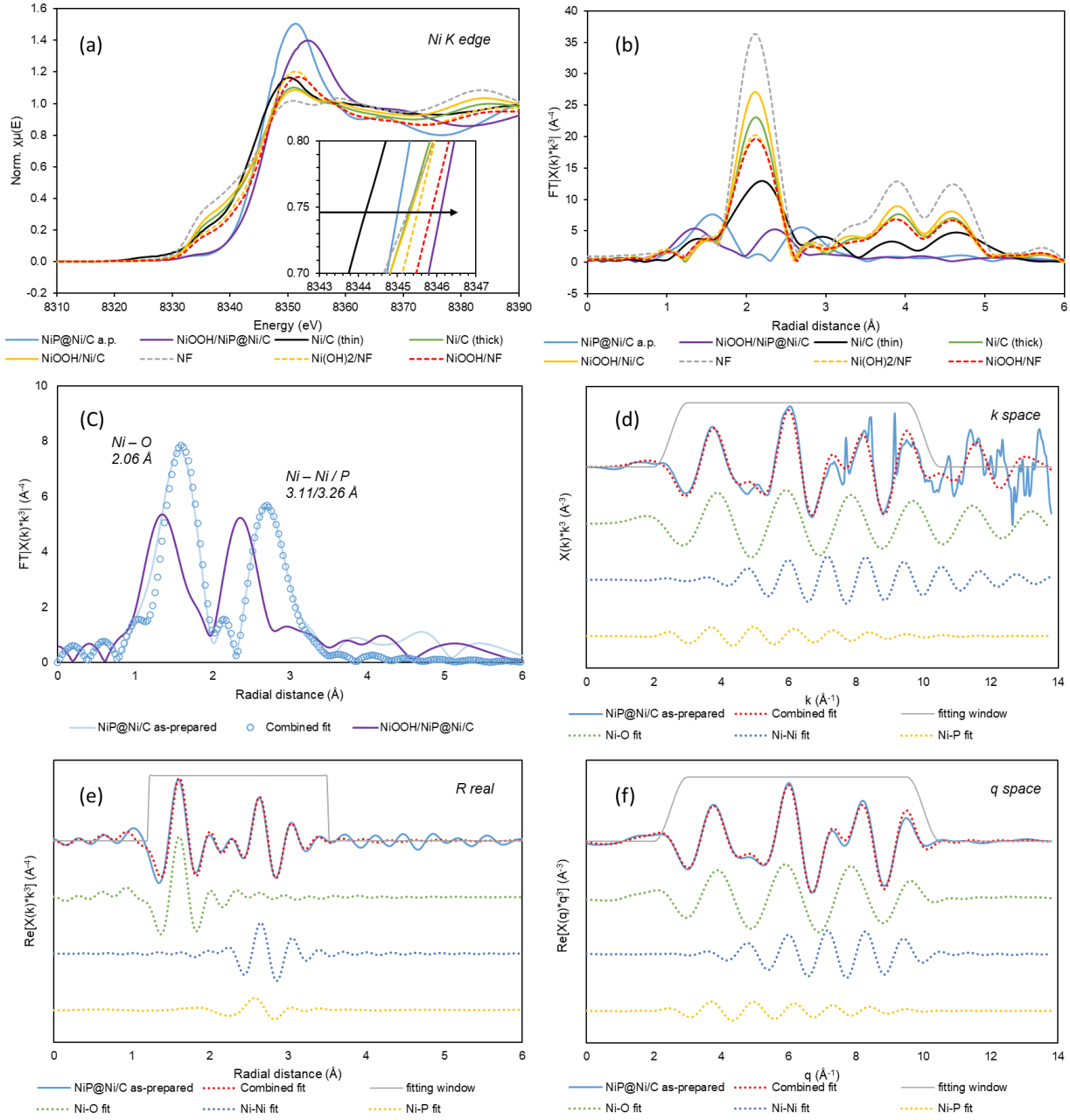

Figure 5. X-ray adsorption spectroscopy a) normalized XANES spectra at Ni K edge and b) Fourier transformed k3-weighted EXAFS spectra in Ni R space on the catalysts; c) Ni-O, Ni-Ni and Ni-P combined fitting on Ni-P catalyst, compared to surface oxidized NiOOH/NiP@Ni/C; Ni-P catalyst fitting d) in k space; e) in R space with real components; and f) in q space by backward Fourier transform.

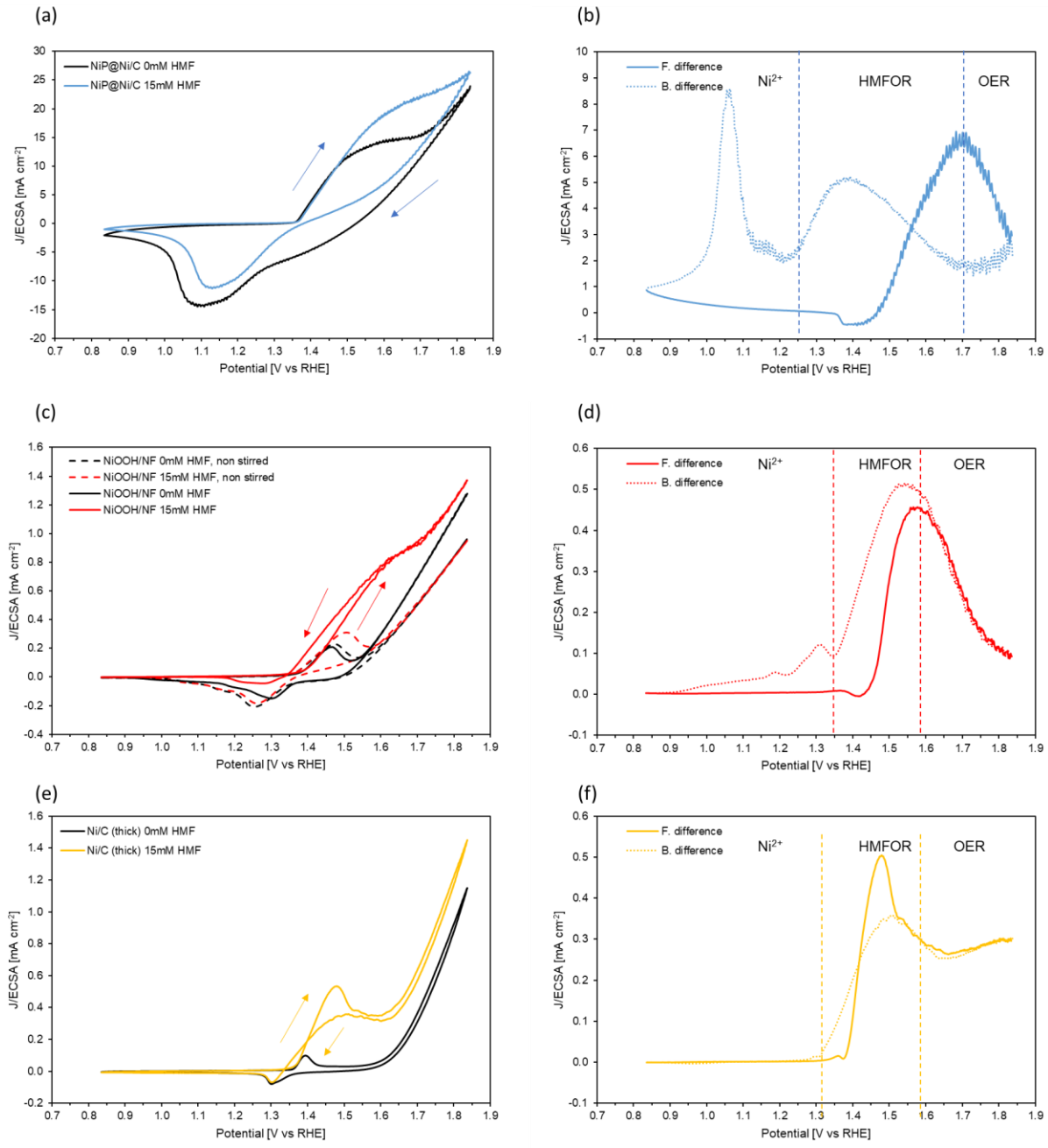

Figure 6. Cyclic voltammetry at 10 mV s^{-1} on a) NiP@NiC; b) the difference in current density on forward scan (blue solid line) and backward scan (black dotted line); CV on c) NiOOH/NF; d) differences in current density; CV on e) NiC; f) differences in current density. Dash lines differentiate dominant surface conditions and reactions. Differences on both forward and backward scans are the scan with 15 mM HMF subtracted by no HMF in 1 M KOH (ECSA-normalized current, without IR correction).

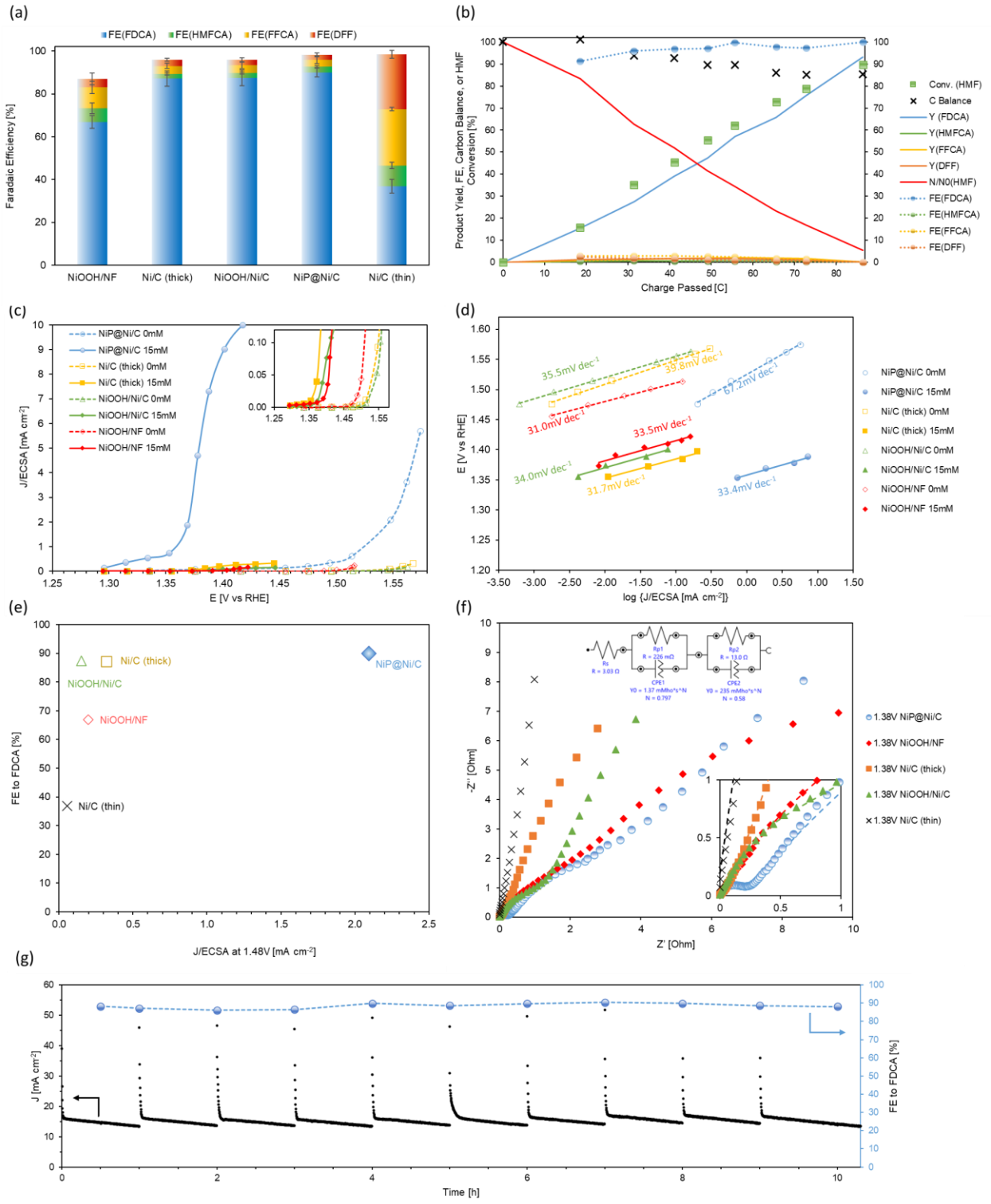

Figure 7. Electrochemical performance of catalysts. a) Faradaic efficiency of HMFOR intermediates and products after constant applied potential at 1.48 V RHE for 30 minutes; b) product yield, faradaic efficiency, and HMF conversion on NiP@Ni/C during constant applied

potential conversion; c) polarization curves in 1 M KOH with and without HMF (iR-corrected); d) Tafel plot in 1 M KOH with and without HMF (iR-corrected); e) comparison among catalysts on applied potential and ECSA-normalized current density; f) electrochemical impedance spectroscopy (EIS) in 1 M KOH with 15 mM HMF; g) chronoamperometry stability test in 1 M KOH with 15 mM HMF.

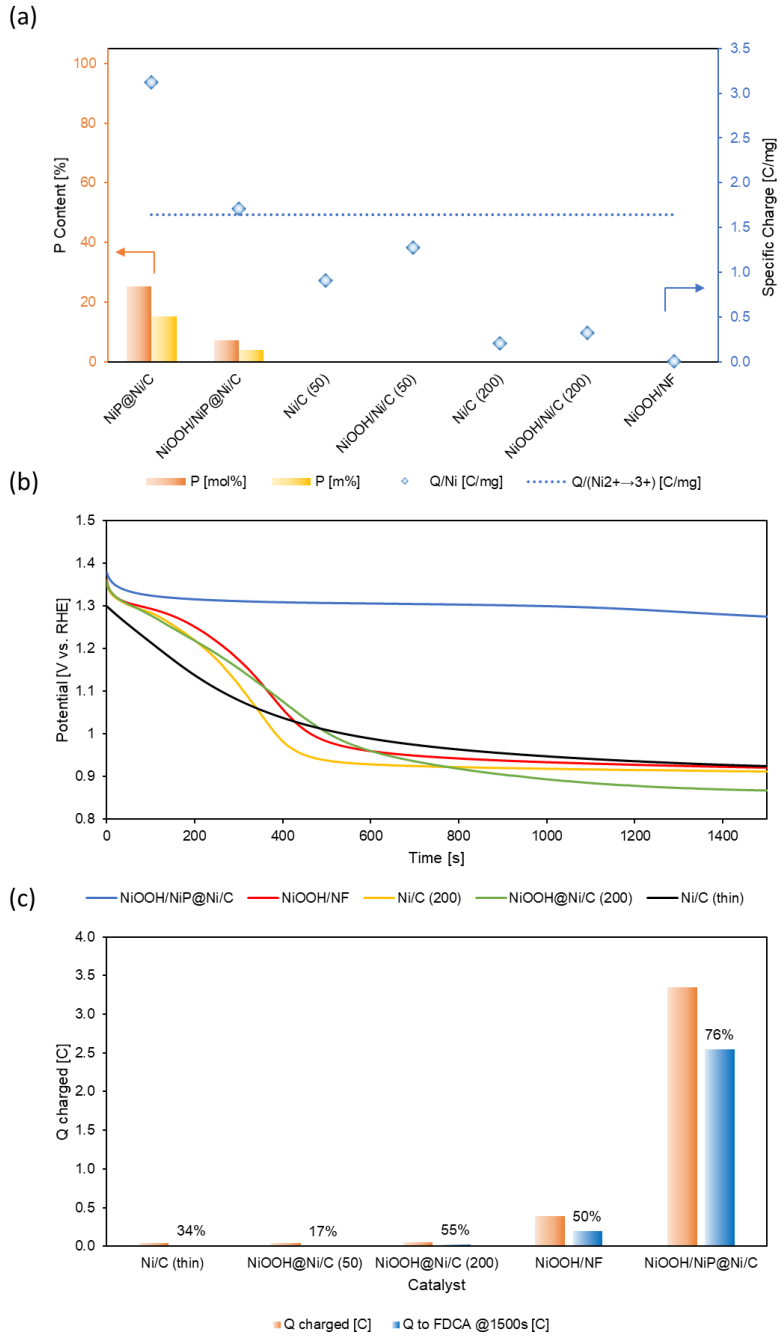

Figure 8. a) Specific charge taken by Ni/C or NiP-derived catalysts with different phosphorus content; b) open circuit potential (OCP) test on different catalysts showing high capacity for maintaining Ni^{3+} on NiP-derived catalysts. C) Charge attained by catalysts during charging stage

and charge responsible for FDCA production during discharging stage in OCP test with efficiency.

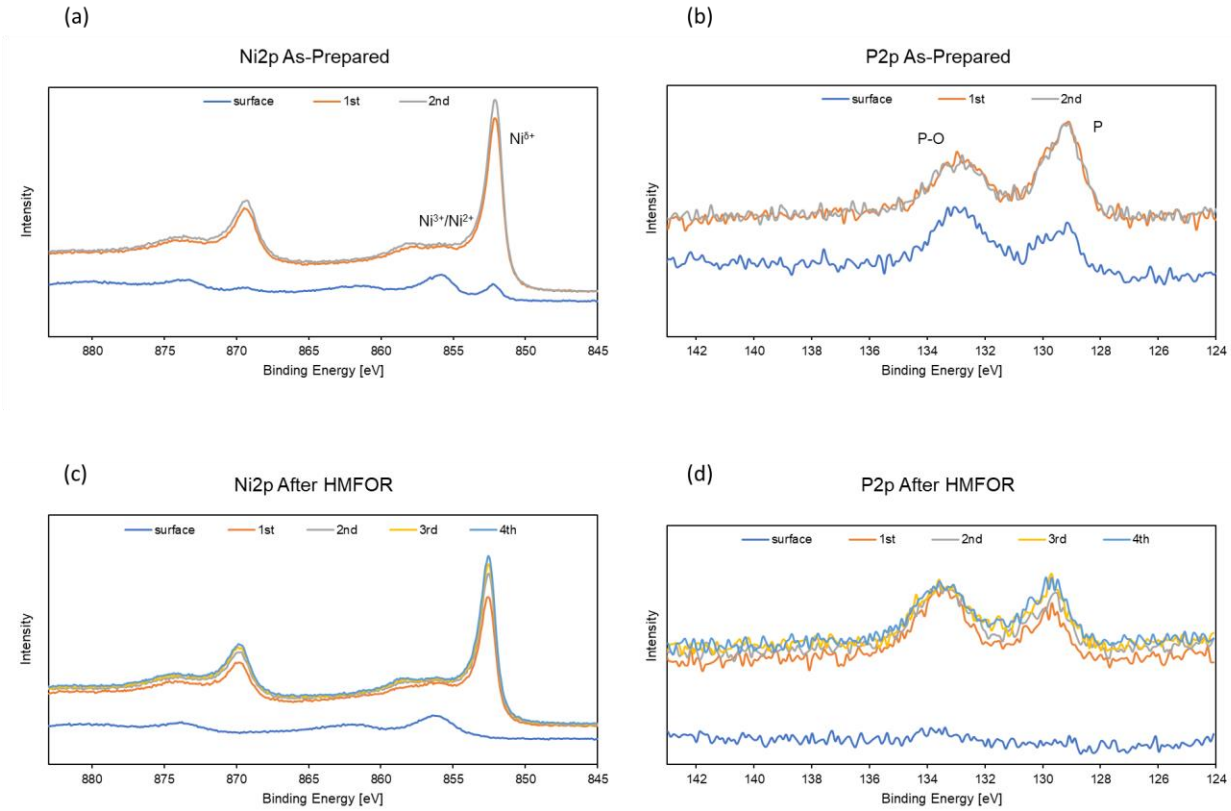

Figure 9. High resolution etching XPS profile on as-prepared NiP@Ni/C on a) Ni 2p spectra; b) P 2p spectra; NiP@Ni/C after HMFOR on c) Ni 2p spectra; d) P 2p spectra.

References

[1] D.A. Giannakoudakis, J.C. Colmenares, D. Tsiplakides, K.S. Triantafyllidis, Nanoengineered Electrodes for Biomass-Derived 5-Hydroxymethylfurfural Electrocatalytic Oxidation to 2,5-Furandicarboxylic Acid, ACS Sustainable Chemistry & Engineering, 9 (2021) 1970-1993.

[2] Q.-S. Kong, X.-L. Li, H.-J. Xu, Y. Fu, Conversion of 5-hydroxymethylfurfural to chemicals: A review of catalytic routes and product applications, Fuel Processing Technology, 209 (2020).

[3] O. Simoska, Z. Rhodes, S. Weliwatte, J.R. Cabrera-Pardo, E.M. Gaffney, K. Lim, S.D. Minteer, Advances in Electrochemical Modification Strategies of 5-Hydroxymethylfurfural, ChemSusChem, 14 (2021) 1674-1686.

[4] 2,5-Furandicarboxylic Acid (FDCA) Market Size Worth USD 786.3 Million by 2027: Reports and Data, MarketWatch, 2021.

[5] A.J.J.E. Eerhart, A.P.C. Faaij, M.K. Patel, Replacing fossil based PET with biobased PEF; process analysis, energy and GHG balance, Energy & Environmental Science, 5 (2012).

[6] Y.-T. Liao, C. Nguyen Van, N. Ishiguro, A.P. Young, C.-K. Tsung, K.C.W. Wu, Engineering a homogeneous alloy-oxide interface derived from metal-organic frameworks for selective oxidation of 5-hydroxymethylfurfural to 2, 5-furandicarboxylic acid, Applied Catalysis B-Environmental, 270 (2020).

[7] D.-H. Nam, B.J. Taitt, K.-S. Choi, Copper-Based Catalytic Anodes To Produce 2,5-Furandicarboxylic Acid, a Biomass-Derived Alternative to Terephthalic Acid, ACS Catalysis, 8 (2018) 1197-1206.

[8] M. Zhang, Y. Liu, B. Liu, Z. Chen, H. Xu, K. Yan, Trimetallic NiCoFe-Layered Double Hydroxides Nanosheets Efficient for Oxygen Evolution and Highly Selective Oxidation of Biomass-Derived 5-Hydroxymethylfurfural, ACS Catalysis, 10 (2020) 5179-5189.

[9] X. Deng, M. Li, Y. Fan, L. Wang, X.-Z. Fu, J.-L. Luo, Constructing multifunctional 'Nanoplatelet-on-Nanoarray' electrocatalyst with unprecedented activity towards novel selective organic oxidation reactions to boost hydrogen production, Applied Catalysis B-Environmental, 278 (2020).

[10] Y. Song, Z. Li, K. Fan, Z. Ren, W. Xie, Y. Yang, M. Shao, M. Wei, Ultrathin layered double hydroxides nanosheets array towards efficient electrooxidation of 5-hydroxymethylfurfural coupled with hydrogen generation, Applied Catalysis B: Environmental, 299 (2021).

[11] X.H. Chadderdon, D.J. Chadderdon, T. Pfennig, B.H. Shanks, W. Li, Paired electrocatalytic hydrogenation and oxidation of 5-(hydroxymethyl)furfural for efficient production of biomass-derived monomers, Green Chemistry, 21 (2019) 6210-6219.

[12] M.J. Kang, H. Park, J. Jegal, S.Y. Hwang, Y.S. Kang, H.G. Cha, Electrocatalysis of 5-hydroxymethylfurfural at cobalt based spinel catalysts with filamentous nanoarchitecture in alkaline media, Applied Catalysis B: Environmental, 242 (2019) 85-91.

[13] S. Barwe, J. Weidner, S. Cychy, D.M. Morales, S. Dieckhöfer, D. Hiltrop, J. Masa, M. Muhler, W. Schuhmann, Electrocatalytic Oxidation of 5-(Hydroxymethyl)furfural Using High-Surface-Area Nickel Boride, Angewandte Chemie International Edition, 57 (2018) 11460-11464.

[14] W.-J. Liu, L. Dang, Z. Xu, H.-Q. Yu, S. Jin, G.W. Huber, Electrochemical Oxidation of 5-Hydroxymethylfurfural with NiFe Layered Double Hydroxide (LDH) Nanosheet Catalysts, ACS Catalysis, 8 (2018) 5533-5541.

[15] B. You, N. Jiang, X. Liu, Y. Sun, Simultaneous H2 Generation and Biomass Upgrading in Water by an Efficient Noble-Metal-Free Bifunctional Electrocatalyst, Angewandte Chemie International Edition, 55 (2016) 9913-9917.

[16] B. You, X. Liu, N. Jiang, Y. Sun, A General Strategy for Decoupled Hydrogen Production from Water Splitting by Integrating Oxidative Biomass Valorization, Journal of the American Chemical Society, 138 (2016) 13639-13646.

[17] N. Zhang, Y. Zou, L. Tao, W. Chen, L. Zhou, Z. Liu, B. Zhou, G. Huang, H. Lin, S. Wang, Electrochemical Oxidation of 5-Hydroxymethylfurfural on Nickel Nitride/Carbon Nanosheets: Reaction Pathway Determined by In Situ Sum Frequency Generation Vibrational Spectroscopy, Angewandte Chemie International Edition, 58 (2019) 15895-15903.

[18] H. Wang, C. Li, J. An, Y. Zhuang, S. Tao, Surface reconstruction of NiCoP for enhanced biomass upgrading, Journal of Materials Chemistry A, 9 (2021) 18421-18430.

[19] N. Jiang, B. You, R. Boonstra, I.M. Terrero Rodriguez, Y. Sun, Integrating Electrocatalytic 5-Hydroxymethylfurfural Oxidation and Hydrogen Production via Co–P-Derived Electrocatalysts, ACS Energy Letters, 1 (2016) 386-390.

[20] X. Deng, G.Y. Xu, Y.J. Zhang, L. Wang, J. Zhang, J.F. Li, X.Z. Fu, J.L. Luo, Understanding the Roles of Electrogenerated Co^{3+} and Co4+ in Selectivity-Tuned 5-Hydroxymethylfurfural Oxidation, Angew Chem Int Ed Engl, (2021).

[21] X. Deng, X. Kang, M. Li, K. Xiang, C. Wang, Z. Guo, J. Zhang, X.-Z. Fu, J.-L. Luo, Coupling efficient biomass upgrading with H-2 production via bifunctional CuxS@NiCo-LDH core-shell nanoarray electrocatalysts, Journal of Materials Chemistry A, 8 (2020) 1138-1146.

[22] B. You, X. Liu, X. Liu, Y. Sun, Efficient H2 Evolution Coupled with Oxidative Refining of Alcohols via A Hierarchically Porous Nickel Bifunctional Electrocatalyst, ACS Catalysis, 7 (2017) 4564-4570.

[23] J. Masa, I. Sinev, H. Mistry, E. Ventosa, M. de la Mata, J. Arbiol, M. Muhler, B. Roldan Cuenya, W. Schuhmann, Ultrathin High Surface Area Nickel Boride (NixB) Nanosheets as Highly Efficient Electrocatalyst for Oxygen Evolution, Advanced Energy Materials, 7 (2017).

[24] L.-A. Stern, L. Feng, F. Song, X. Hu, Ni2P as a Janus catalyst for water splitting: the oxygen evolution activity of Ni2P nanoparticles, Energy & Environmental Science, 8 (2015) 2347-2351.

[25] X.-Y. Yu, Y. Feng, B. Guan, X.W. Lou, U. Paik, Carbon coated porous nickel phosphides nanoplates for highly efficient oxygen evolution reaction, Energy & Environmental Science, 9 (2016) 1246-1250.

[26] C. Gao, L. Dai, W. Meng, Z. He, L. Wang, Electrochemically promoted electroless nickel-phosphorous plating on titanium substrate, Applied Surface Science, 392 (2017) 912-919.

[27] J. Lian, Y. Wu, H. Zhang, S. Gu, Z. Zeng, X. Ye, One-step synthesis of amorphous Ni–Fe–P alloy as bifunctional electrocatalyst for overall water splitting in alkaline medium, International Journal of Hydrogen Energy, 43 (2018) 12929-12938.

[28] F. Du, Y. Zhang, H. He, T. Li, G. Wen, Y. Zhou, Z. Zou, Electrodeposited amorphous cobalt phosphosulfide on Ni foams for highly efficient overall water splitting, Journal of Power Sources, 431 (2019) 182-188.

[29] Z. Li, X. Dou, Y. Zhao, C. Wu, Enhanced oxygen evolution reaction of metallic nickel phosphide nanosheets by surface modification, Inorganic Chemistry Frontiers, 3 (2016) 1021-1027.

[30] K. Wang, Y. Si, Z. Lv, T. Yu, X. Liu, G. Wang, G. Xie, L. Jiang, Efficient and stable Ni–Co–Fe–P nanosheet arrays on Ni foam for alkaline and neutral hydrogen evolution, International Journal of Hydrogen Energy, 45 (2020) 2504-2512.

[31] J. Masa, S. Barwe, C. Andronescu, I. Sinev, A. Ruff, K. Jayaramulu, K. Elumeeva, B. Konkena, B. Roldan Cuenya, W. Schuhmann, Low Overpotential Water Splitting Using Cobalt–Cobalt Phosphide Nanoparticles Supported on Nickel Foam, ACS Energy Letters, 1 (2016) 1192-1198.

[32] H. Liang, A.N. Gandi, D.H. Anjum, X. Wang, U. Schwingenschlogl, H.N. Alshareef, Plasma-Assisted Synthesis of NiCoP for Efficient Overall Water Splitting, Nano Lett, 16 (2016) 7718-7725.

[33] H.-R. Seo, K.-S. Cho, Y.-K. Lee, Formation mechanisms of Ni2P nanocrystals using XANES and EXAFS spectroscopy, Materials Science and Engineering: B, 176 (2011) 132-140.

[34] B.J. Taitt, D.-H. Nam, K.-S. Choi, A Comparative Study of Nickel, Cobalt, and Iron Oxyhydroxide Anodes for the Electrochemical Oxidation of 5-Hydroxymethylfurfural to 2,5-Furandicarboxylic Acid, ACS Catalysis, 9 (2018) 660-670.

[35] M. Liu, L. Yuan, G. Fan, L. Zheng, L. Yang, F. Li, NiCu Nanoparticles for Catalytic Hydrogenation of Biomass-Derived Carbonyl Compounds, ACS Applied Nano Materials, 3 (2020) 9226-9237.

[36] H. Li, H. Li, W.-L. Dai, W. Wang, Z. Fang, J.-F. Deng, XPS studies on surface electronic characteristics of Ni–B and Ni–P amorphous alloy and its correlation to their catalytic properties, Applied Surface Science, 152 (1999) 25-34.

[37] M.O. Abba, V.M. Gonzalez-DelaCruz, G. Colón, S. Sebti, A. Caballero, In situ XAS study of an improved natural phosphate catalyst for hydrogen production by reforming of methane, Applied Catalysis B: Environmental, 150-151 (2014) 459-465.

[38] D. Gonzalez-Flores, I. Sanchez, I. Zaharieva, K. Klingan, J. Heidkamp, P. Chernev, P.W. Menezes, M. Driess, H. Dau, M.L. Montero, Heterogeneous water oxidation: surface activity versus amorphization activation in cobalt phosphate catalysts, Angew Chem Int Ed Engl, 54 (2015) 2472-2476.

[39] X. Song, X. Liu, H. Wang, Y. Guo, Y. Wang, Improved Performance of Nickel Boride by Phosphorus Doping as an Efficient Electrocatalyst for the Oxidation of 5-Hydroxymethylfurfural to 2,5-Furandicarboxylic Acid, Industrial & Engineering Chemistry Research, 59 (2020) 17348-17356.

[40] M.S.E. Houache, K. Hughes, A. Ahmed, R. Safari, H. Liu, G.A. Botton, E.A. Baranova, Electrochemical Valorization of Glycerol on Ni-Rich Bimetallic NiPd Nanoparticles: Insight into Product Selectivity Using in Situ Polarization Modulation Infrared-Reflection Absorption Spectroscopy, ACS Sustainable Chemistry & Engineering, 7 (2019) 14425-14434.

[41] M. Fleischmann, K. Korinek, D. Pletcher, The oxidation of organic compounds at a nickel anode in alkaline solution, Journal of Electroanalytical Chemistry and Interfacial Electrochemistry, 31 (1971) 39-49.

[42] M.T. Bender, Y.C. Lam, S. Hammes-Schiffer, K.S. Choi, Unraveling Two Pathways for Electrochemical Alcohol and Aldehyde Oxidation on NiOOH, J Am Chem Soc, 142 (2020) 21538-21547.

[43] D. Fa, M. Zhou, H. Zhao, Y. Jiang, Y. Miao, 3D flower-like Ni–Co–S with high specific surface area for the electrocatalytic oxidation of methanol, Polyhedron, 144 (2018) 11-17.

[44] L. Xu, Z. Wang, X. Chen, Z. Qu, F. Li, W. Yang, Ultrathin layered double hydroxide nanosheets with Ni(III) active species obtained by exfoliation for highly efficient ethanol electrooxidation, Electrochimica Acta, 260 (2018) 898-904.

[45] M.T. Bender, X. Yuan, K.S. Choi, Alcohol oxidation as alternative anode reactions paired with (photo)electrochemical fuel production reactions, Nat Commun, 11 (2020) 4594.

[46] J. van Drunen, T.W. Napporn, B. Kokoh, G. Jerkiewicz, Electrochemical oxidation of isopropanol using a nickel foam electrode, Journal of Electroanalytical Chemistry, 716 (2014) 120-128.

[47] J. Weidner, S. Barwe, K. Sliozberg, S. Piontek, J. Masa, U.P. Apfel, W. Schuhmann, Cobalt-metalloid alloys for electrochemical oxidation of 5-hydroxymethylfurfural as an alternative anode reaction in lieu of oxygen evolution during water splitting, Beilstein J Org Chem, 14 (2018) 1436-1445.

[48] Z. Zhou, C. Chen, M. Gao, B. Xia, J. Zhang, In situ anchoring of a Co3O4 nanowire on nickel foam: an outstanding bifunctional catalyst for energy-saving simultaneous reactions, Green Chemistry, 21 (2019) 6699-6706.

[49] X. Liu, S. Shi, Q. Xiong, L. Li, Y. Zhang, H. Tang, C. Gu, X. Wang, J. Tu, Hierarchical NiCo2O4@NiCo2O4 core/shell nanoflake arrays as high-performance supercapacitor materials, ACS Appl Mater Interfaces, 5 (2013) 8790-8795.

[50] L. Gao, Z. Liu, J. Ma, L. Zhong, Z. Song, J. Xu, S. Gan, D. Han, L. Niu, NiSe@NiOx core-shell nanowires as a non-precious electrocatalyst for upgrading 5-hydroxymethylfurfural into 2,5-furandicarboxylic acid, Applied Catalysis B-Environmental, 261 (2020).

3. HMFOR SI

Supporting Information

High Oxidation State Enabled by Plated Ni-P Achieves Superior Electrocatalytic Performance for 5-Hydroxymethylfurfural Oxidation Reaction

Roger Lina, Mahdi Salehia, Jiaxun Guoa, Ali Seifitokaldania,*

a Department of Chemical Engineering, McGill University,
3610 Rue University, Montréal, QC, H3A 0C5, Canada
* Corresponding author
E-mail address: ali.seifitokaldani@mcgill.ca (A. Seifitokaldani)

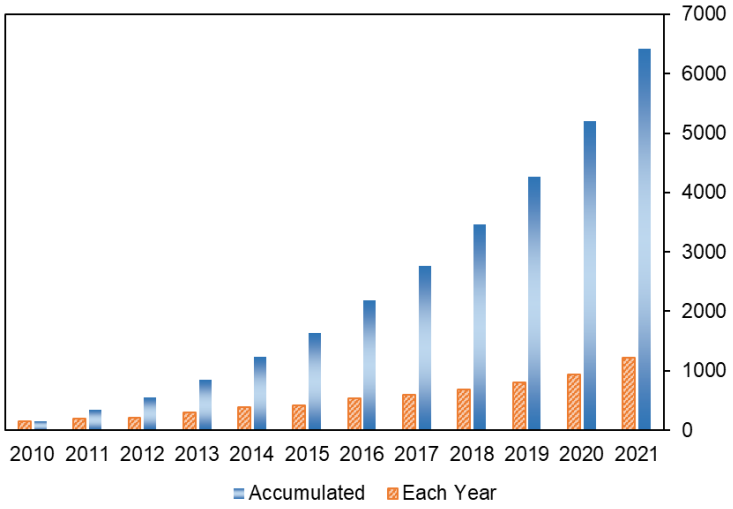

Figure S1. Number of publications search on Google Scholar by key words “HMF electrochemical oxidation” since the year of 2010 up to 2021.

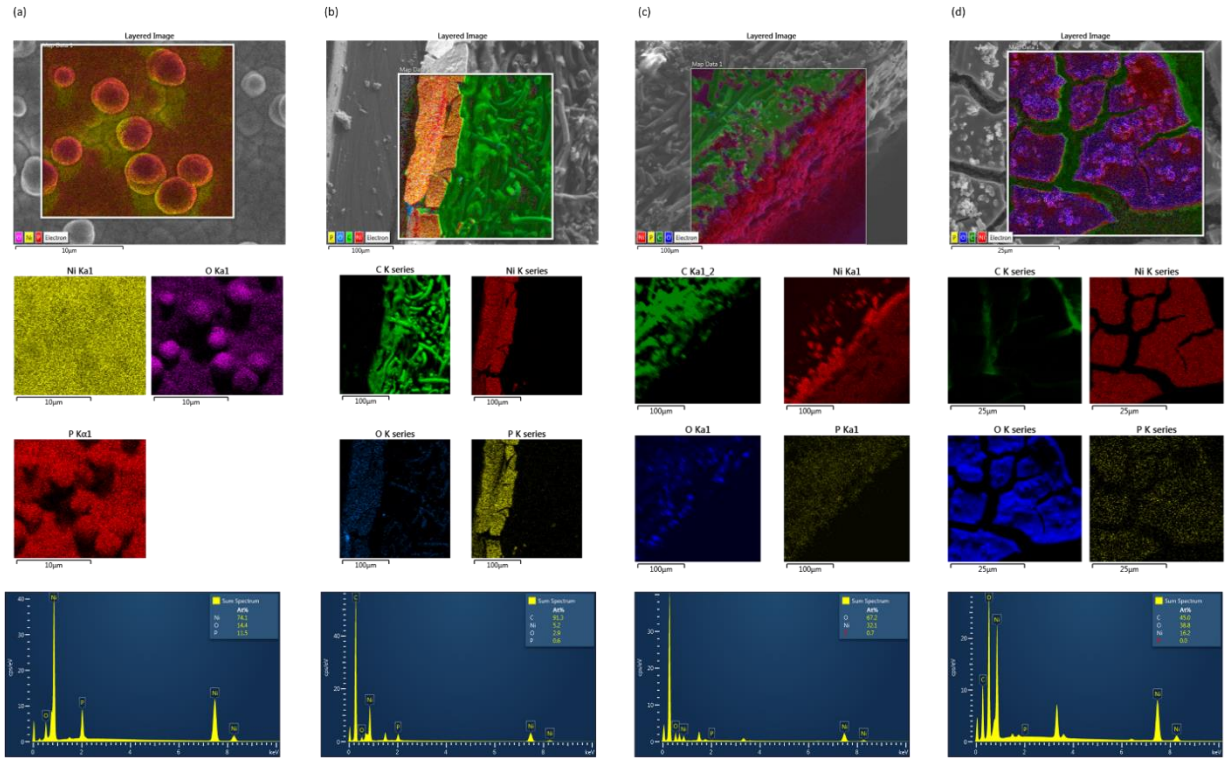

Figure S2. Scanning electron spectroscopy (SEM) with energy dispersive X-ray (EDX) analysis on as-prepared NiP@Ni/C a) on catalyst surface; b) from cross-section; and post-HMFOR c) on catalyst surface; and d) from cross-section.

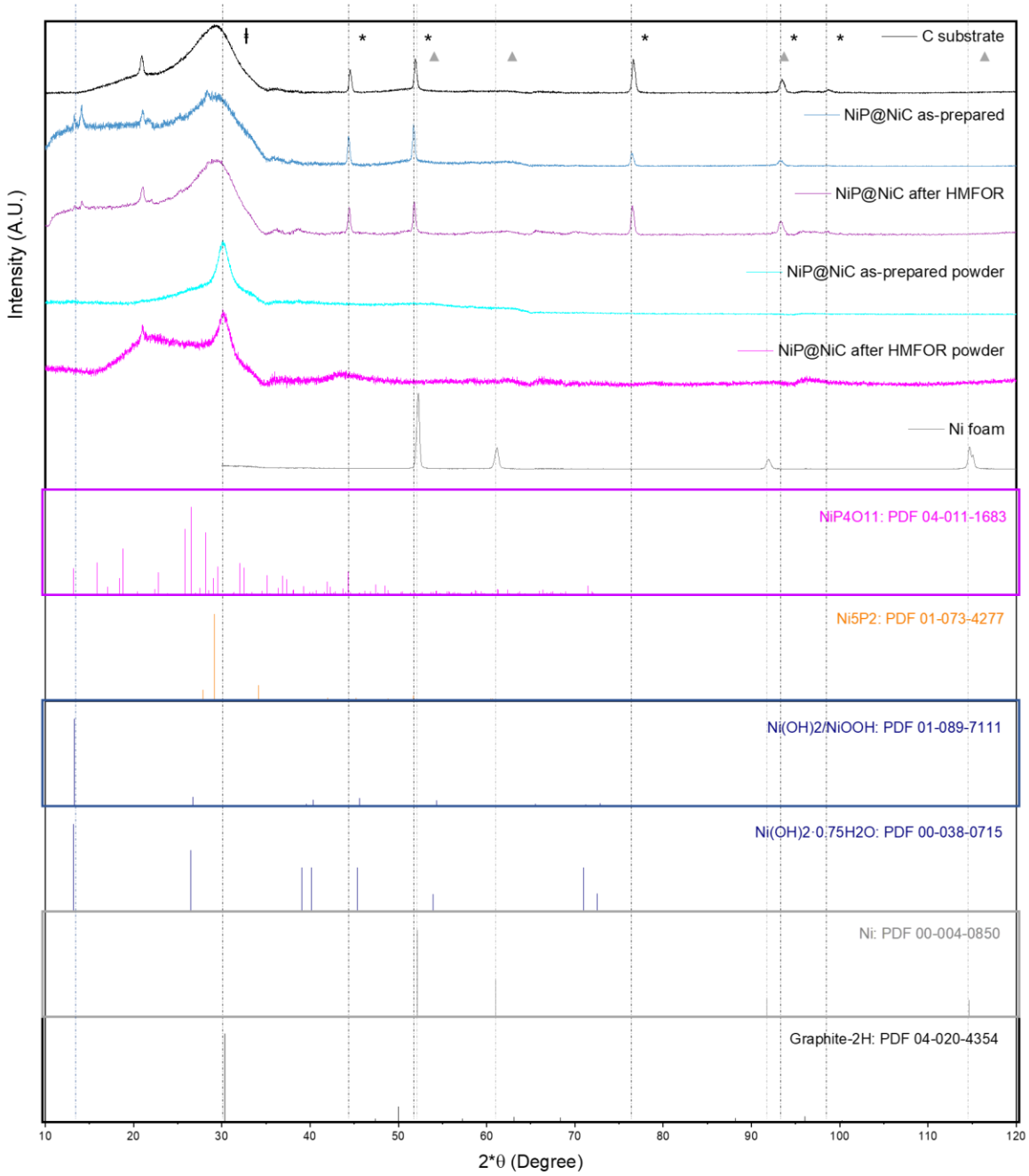

Figure S3. X-ray diffraction analysis on carbon substrate, as-prepared NiP@Ni/C, post HMFOR NiP@Ni/C, and powder form as-prepared HMFOR NiP@Ni/C and post HMFOR NiP@Ni/C, with respective references.

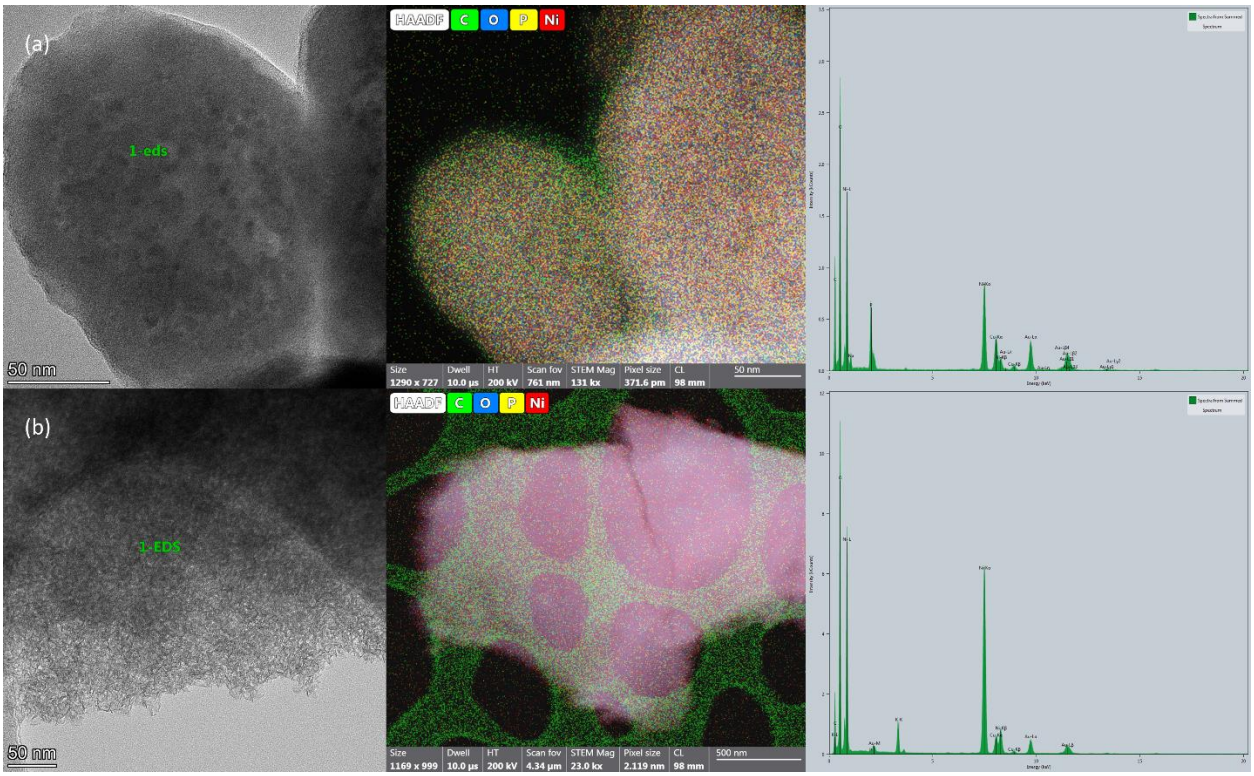

Figure S4. HR-TEM, HAADF and EDX of Ni-P catalyst a) as-prepared and b) post HMFOR.

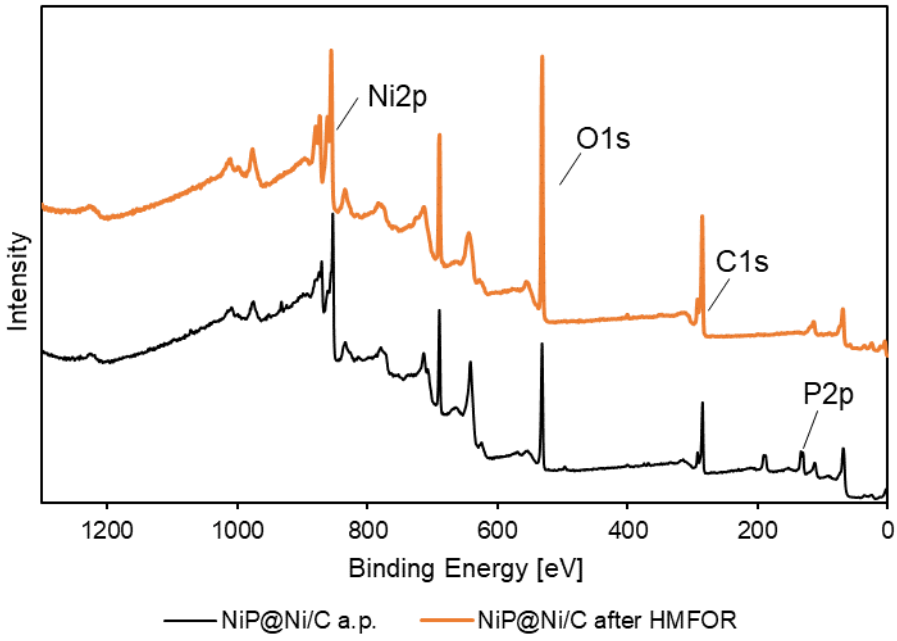

Figure S5. X-ray photoelectron spectroscopy survey on as-prepared and post HMFOR NiP@Ni/C catalysts.

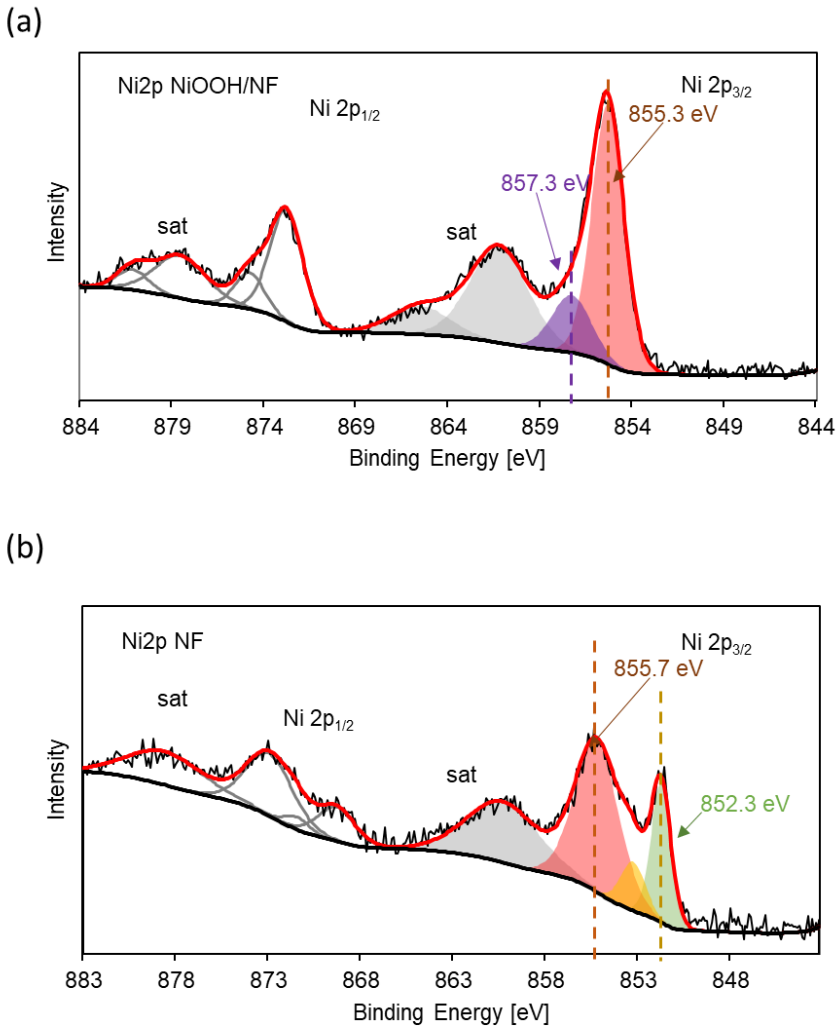

Figure S6. a) XPS of NiOOH/NF; b) XPS of Ni foam.

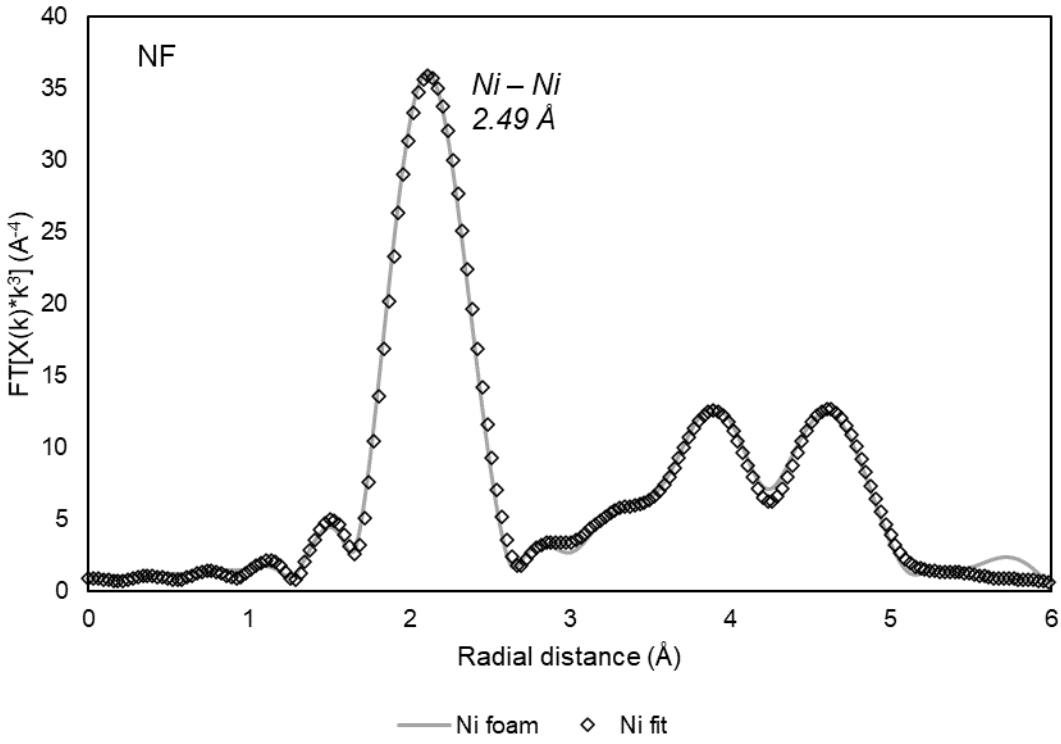

Figure S7. FT-EXAFS Ni ccp fitting of Ni foam.

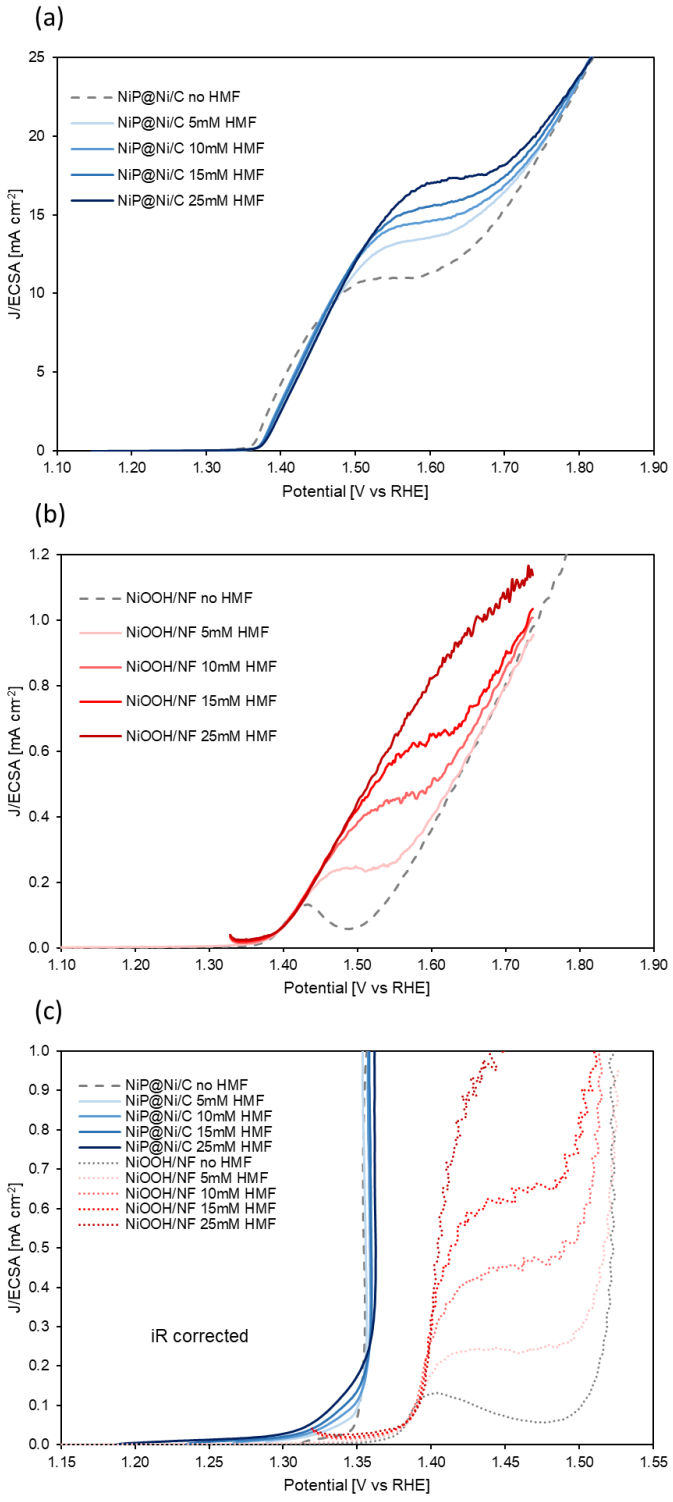

Figure S8. Linear sweep voltammetry at 5 mV s^{-1} on a) NiP@NiC and b) NiOOH/NF with various HMF concentrations in 1 M KOH normalized by ECSA; c) zoom-in on Ni oxidation onset region for the two catalysts with iR correction.

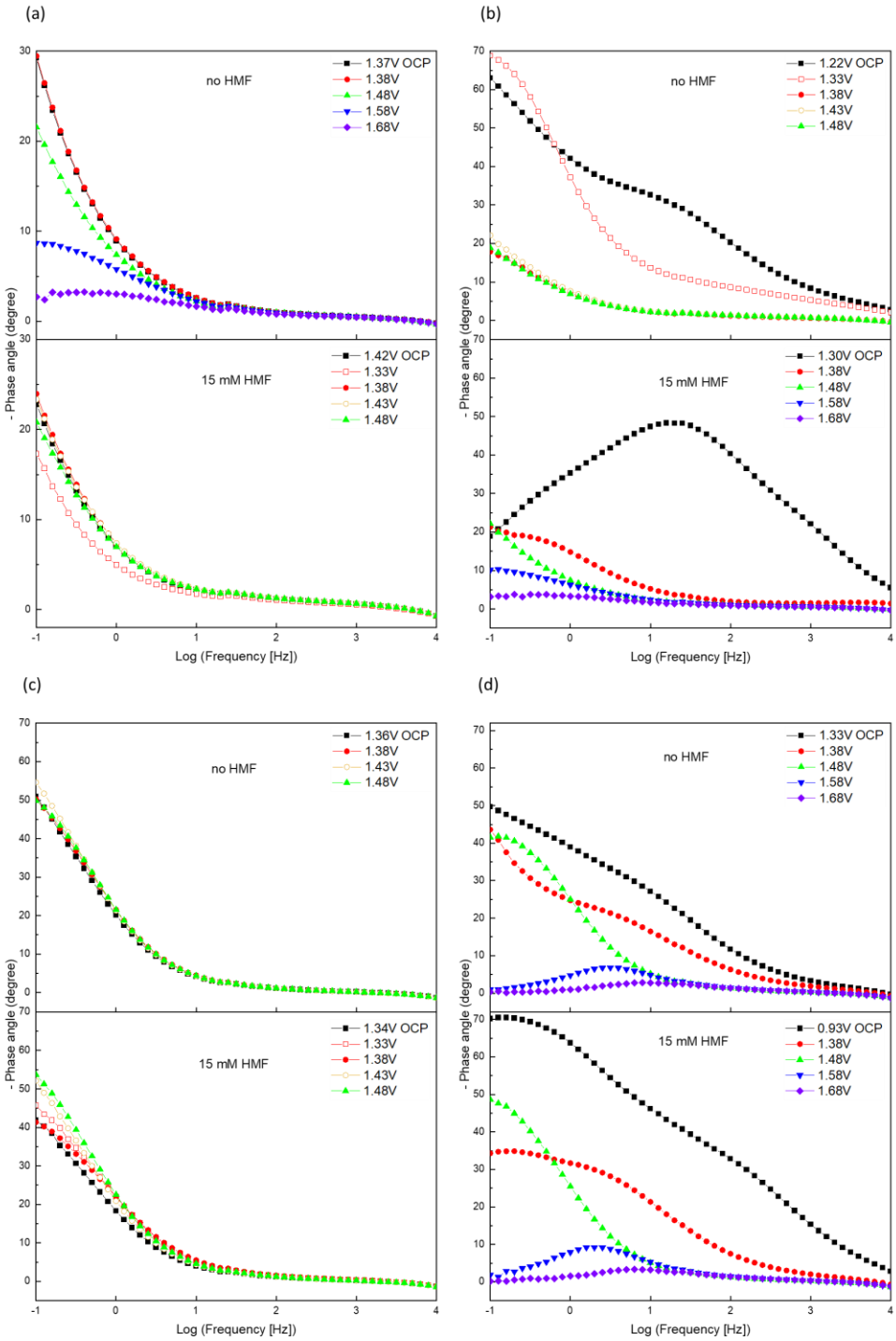

Figure S9. Bode phase plots of NiP@Ni/C starting with a) an oxidized surface with Ni^{3+} and b) a partially reduced surface; and NiOOH/NF starting with c) an oxidized surface with Ni^{3+} and d) a partially reduced surface, with and without HMF in 1 M KOH.

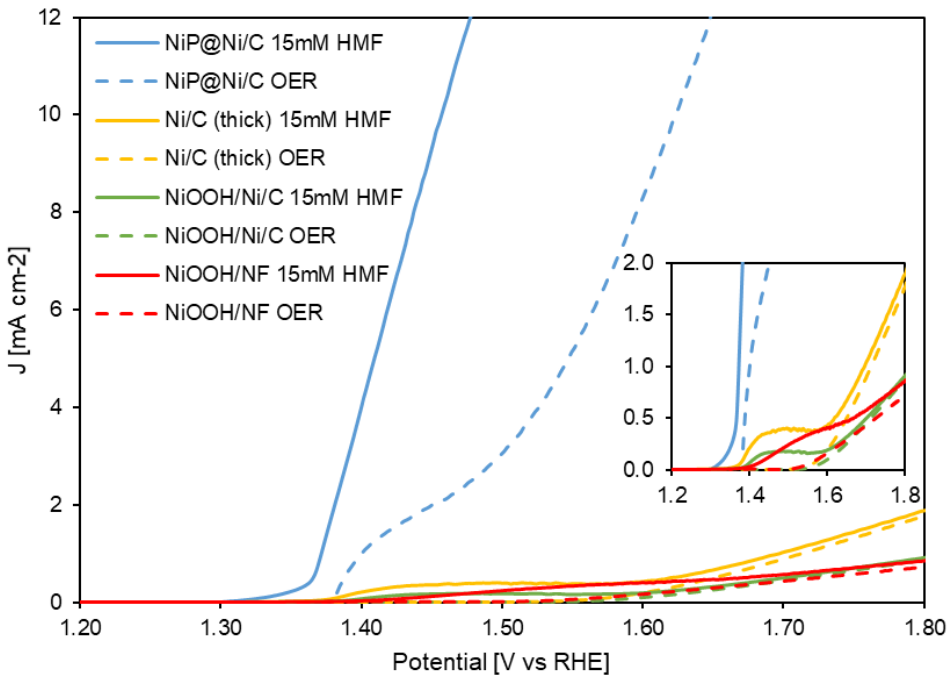

Figure S10. Linear sweep voltammetry, solid lines were taken at 5 mV s^{-1} with 15 mM HMF in 1 M KOH, dash lines were taken at 2 mV s^{-1} as a second scan with no HMF (just OER) on NiP@NiC (blue), thick NiC (yellow), NiOOH/NF (green), and NiOOH/NF (red) (ECSA-normalized current density, without IR correction). Inset shows a zoomed in view at lower current density.

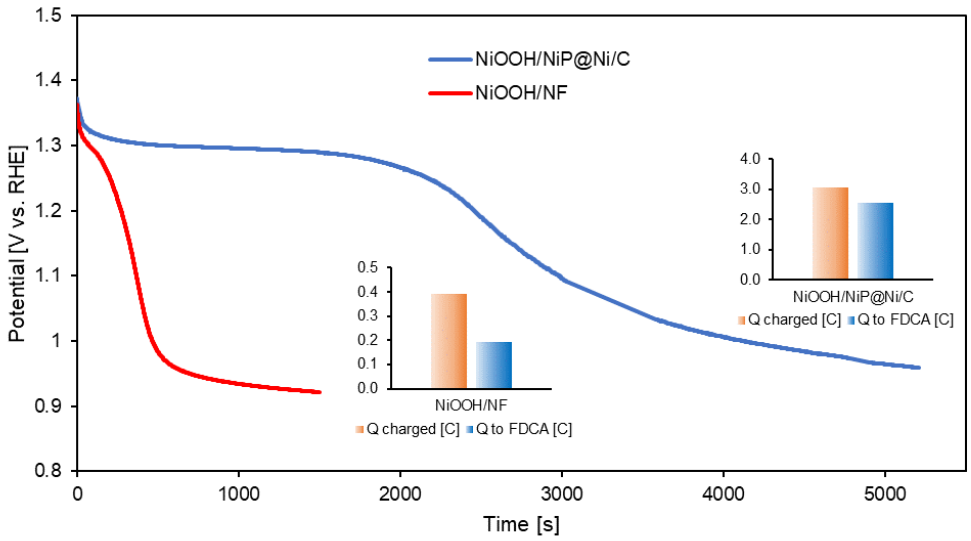

Figure S11. Comparison on OCP experiment on NiOOH/NiP@NiC and NiOOH/NF in 1 M KOH with 5mM HMF.

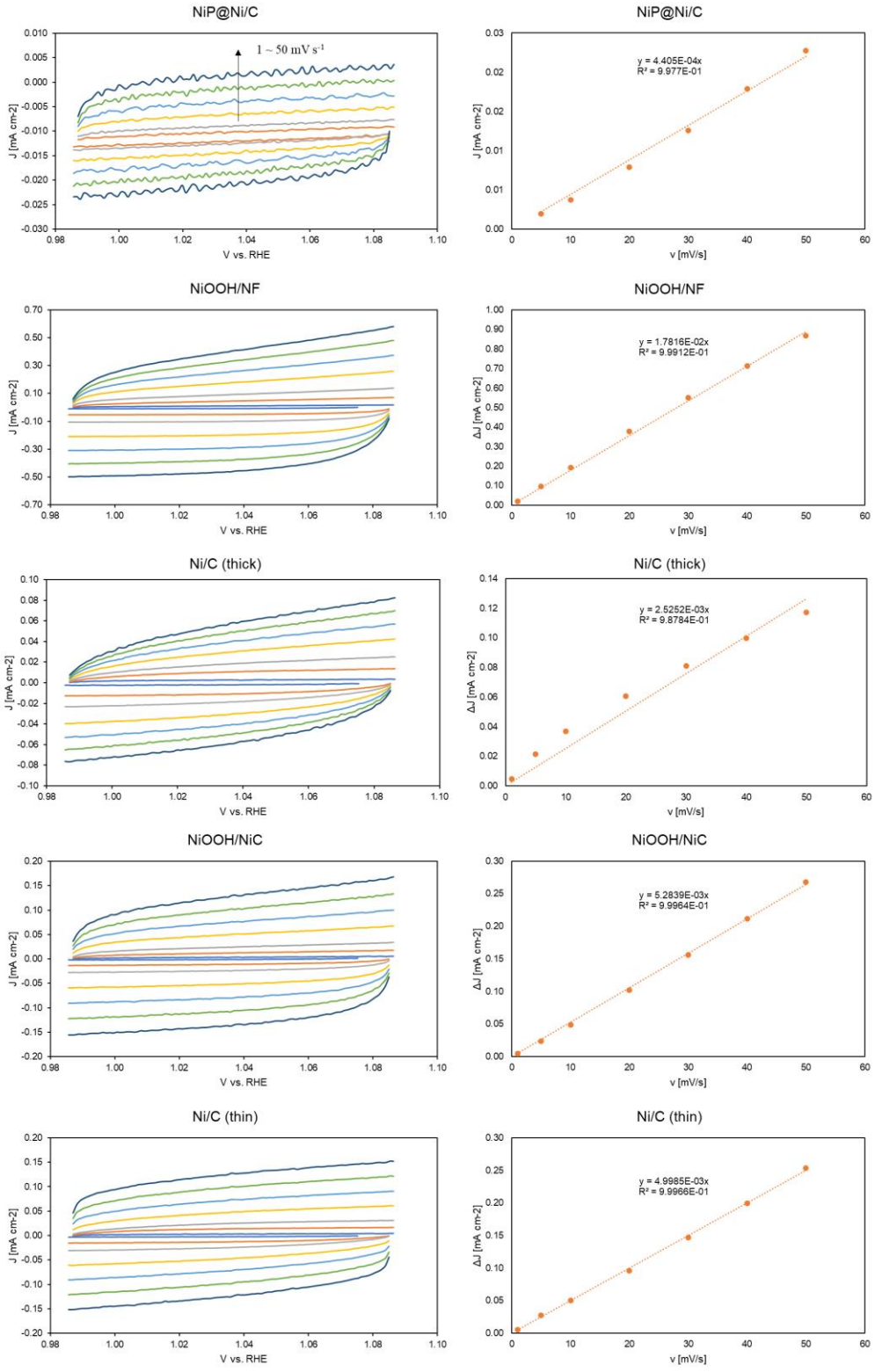

Figure S12. ECSA test by repeated LSV method on varies catalysts in 1 M KOH, scan rates range from 1 mV s^{-1} to 50 mV s^{-1}.

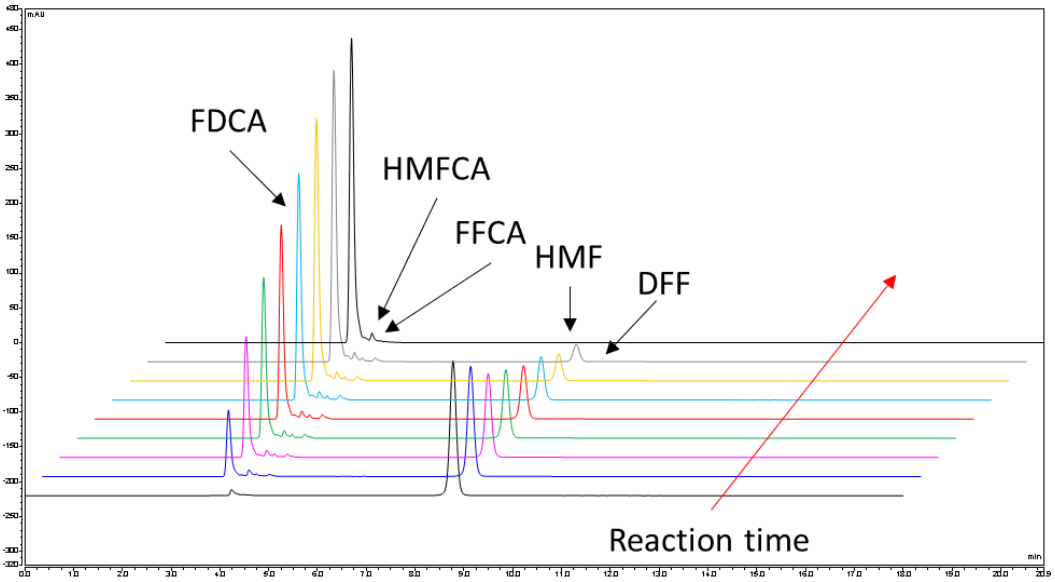

Figure S13. HPLC chromatogram during HMFOR full conversion test.

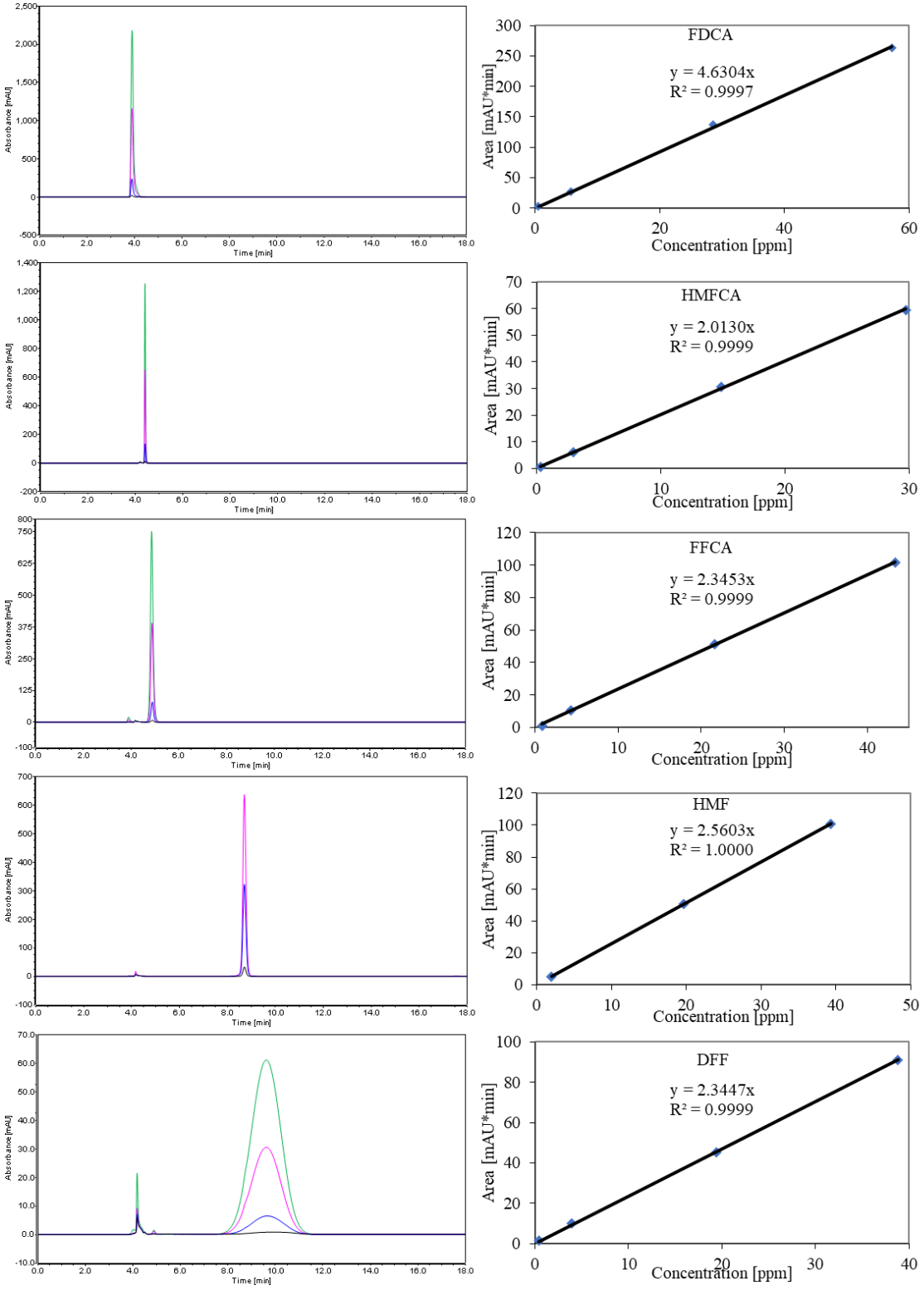

Figure S14. HPLC calibration curves for HMFOR reactant (HMF), intermediates (HMFCA, DFF, FFCA) and final product FDCA.

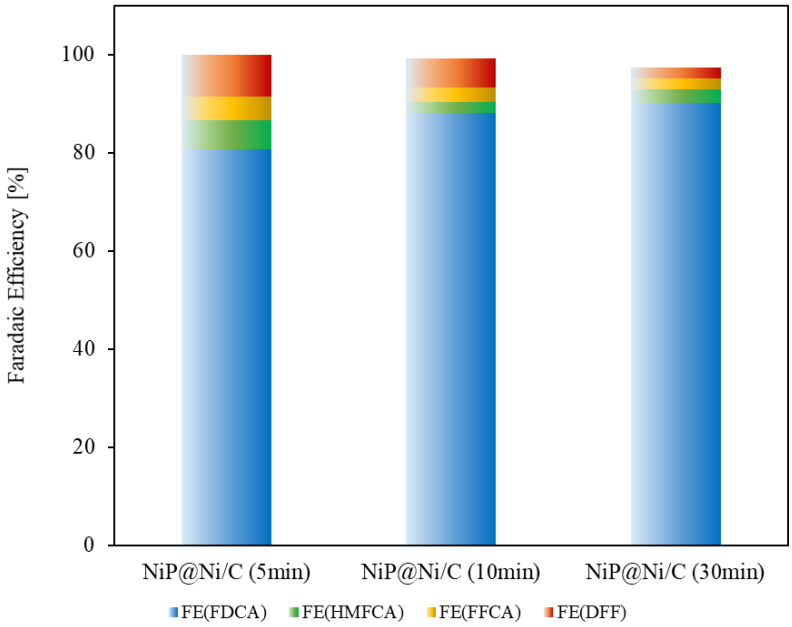

Figure S15. Faradaic efficiency of NiP@Ni/C for HMFOR in short experiments.

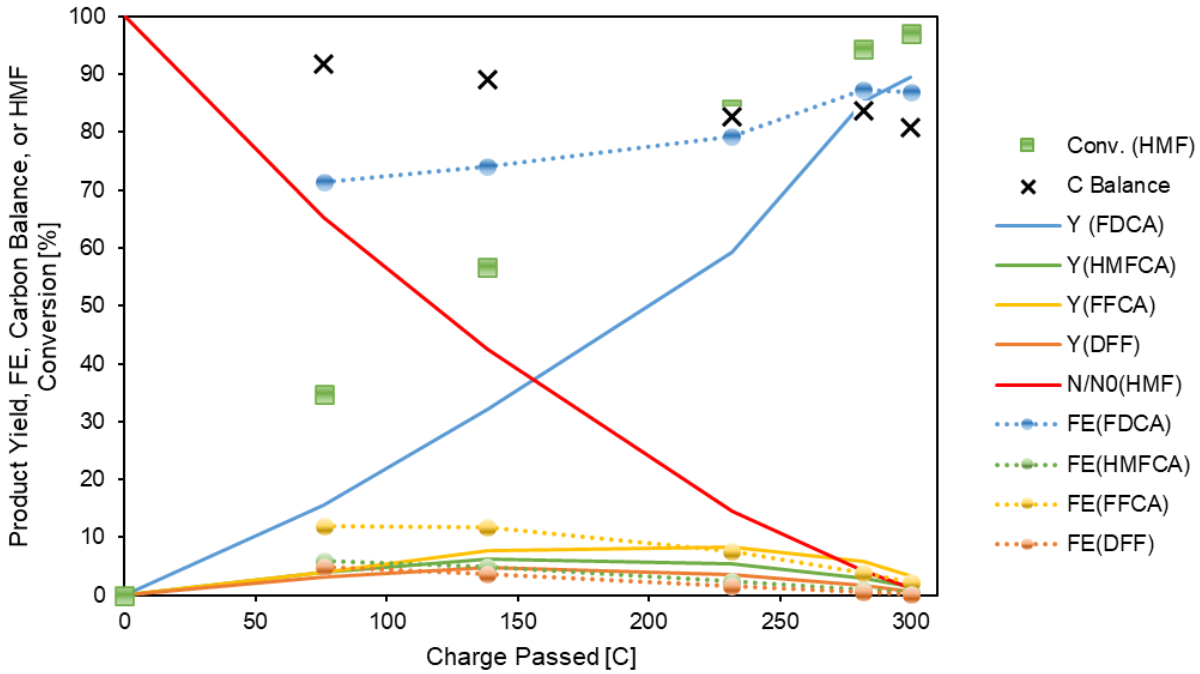

Figure S16. Product yield, faradaic efficiency, and HMF conversion on NiOOH/NF during constant applied potential conversion at 1.48 V with 15 mM HMF.

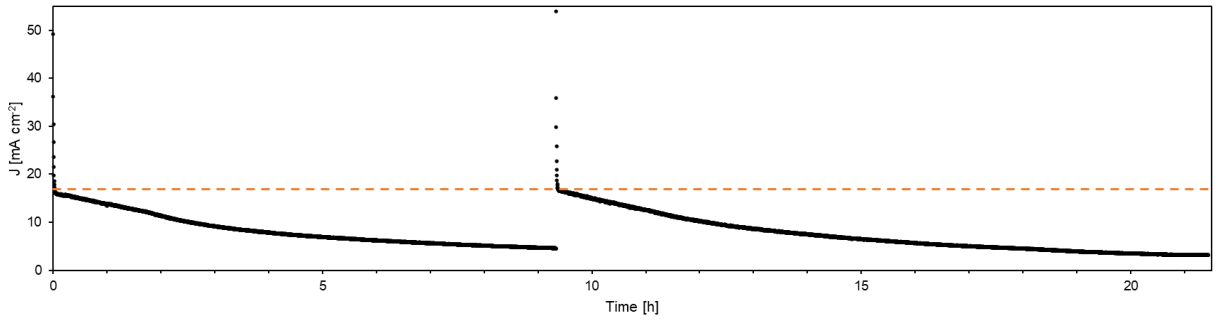

Figure S17. Stability test over 20 hours in 1M KOH with 15 mM HMF.

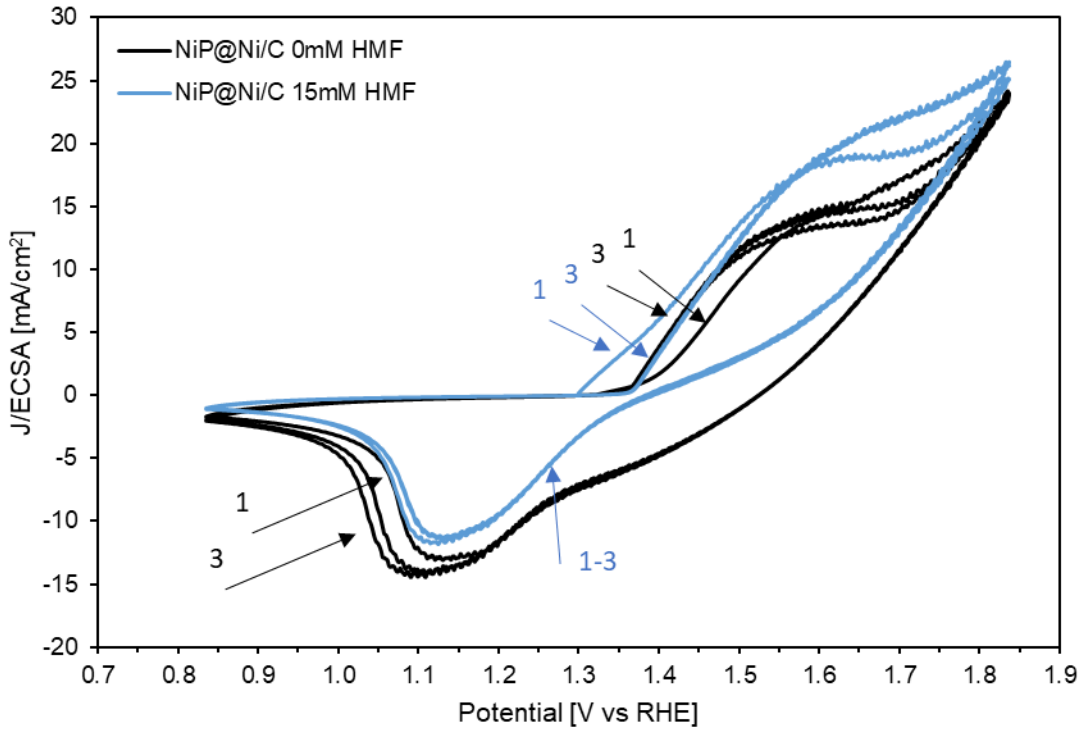

Figure S18. Recoverability of NiP@Ni/C by cyclic voltammetry, with scan numbers indicated.

Table S1. TEM-EDX elemental analysis results

As-prepared NiP@Ni/C							
Z	**Element**	**Family**	**Atomic Fraction (%)**	**Atomic Error (%)**	**Mass Fraction (%)**	**Mass Error (%)**	**Fit Error (%)**
6	C	K	34.2	5.41	19.88	1.78	1.93
8	O	K	47	11.96	36.38	7.95	0.77
15	P	K	7.18	1.77	10.76	2.25	0.45
28	Ni	K	11.62	2.39	32.98	5.26	0.33
Used NiP@Ni/C							
Z	**Element**	**Family**	**Atomic Fraction (%)**	**Atomic Error (%)**	**Mass Fraction (%)**	**Mass Error (%)**	**Fit Error (%)**
6	C	K	12.6	2.48	5.51	0.68	8.24
8	O	K	59.3	15.7	34.6	7.4	1.25
15	P	K	0.31	0.08	0.35	0.07	0.95
28	Ni	K	27.8	6.17	59.5	9.48	0.17

Table S2. FT-EXAFS fitting parameters

NiP@Ni/C as-prepared	**Shell**	**CN**	**ΔE0 (eV)**	**ΔR (Å)**	**σ2 (Å^2)**	**R (Å)**	**Amp**	**R factor (%)**
	Ni-O	4.725	-0.538	0.005	0.004	2.061	0.8	1.016
	Ni-Ni	4.398	-0.538	-0.062	0.009	3.110		
	Ni-P	5.154	-0.538	0.043	0.016	3.257		
Ni foam	**Shell[a)]**	**CN**	**ΔE0 (eV)**	**ΔR (Å)**	**σ2 (Å^2)**	**R (Å)**		**R factor (%)**
	Ni-Ni 1st	12	-5.734	-0.0005	0.005	2.491	0.8	1.285

Ni-Ni 2nd	6	-5.734	-0.0007	0.008	3.523
Ni-Ni 3rd	24	-5.734	-0.0008	0.008	4.315

[a)] Fitting was done with all shells available in Ni cubic close packed below R = 5 Å, using a Debye model; only first three single scattering paths are demonstrated in the table

Table S3. EIS fitting on HMFOR electrocatalysts

Catalyst	**V vs RHE**	**Rs [Ω]**	**Rct_1 [Ω]**	**CPE_1, Y_0**	**CPE_1, n**	**Rct_2 [Ω]**	**CPE_2, Y_0**	**CPE_2, n**	**χ^2**
NiOOH/NF	1.38	1.40	3.98	0.058	0.65	14.10	0.130	0.94	0.004
NiOOH/Ni/C	1.38	3.04	1.21	0.006	0.82	51.70	0.020	0.82	0.010
Ni/C (thick)	1.38	2.94	0.12	0.097	0.64	46.40	0.025	0.83	0.010
Ni/C (thin)	1.38	3.16	-	-	-	5530	0.000	0.91	0.104
NiP@NiC	1.38	3.03	0.23	0.001	0.80	13.00	0.235	0.58	0.007

Table S4. Electrochemical properties of investigated HMFOR electrocatalysts

Catalyst	**J/ESCA [mA cm^{-2}]**	**FE (FDCA) [%]**	**V@1mA cm^{-2} [vs. RHE]**	**Tafel slope in 15 mM HMF [mV dec^{-1}]**	**Rct @1.38V [Ω]**	**Cdl [mF cm^{-2}]**
NiOOH/NF	0.199	67	1.49	33.5	14.10	9.401
NiOOH/Ni/C	0.152	87	1.62	34.0	51.70	2.642
Ni/C (thick)	0.319	87	1.60	31.7	46.40	1.263
Ni/C (thin)	0.776	37	1.67	-	5530	2.499
NiP@Ni/C	2.093	90	1.36	33.4	13.00	0.220

Table S5. A comparison of the electrochemical performance of reported HMFOR electrocatalysts

Electrode Materials	**HMF [mM]**	**Potential [V RHE]**	**Current density [mA cm^{-2}]**	**ECSA-normalized current density [mA cm^{-2}]**	**Tafel slope [mV dec^{-1}]**	**FDCA yield [%]**	**FDCA FE [%]**	**Ref.**
$NiCo_2O_4$/NF	5	1.53	14.83	2.20	135.7	90.8	87.5	*[1]*
Ni_xB/NF	10	1.45	100	N/A	N/A	98.5	~100	*[2]*
NiFe LDH	10	1.33	36.9	0.080	75	98	98.6	*[3]*
Ni_2P NPA/NF	10	1.423	>200	N/A	N/A	100	98	*[4]*
Ni_3S_2/NF	10	1.423	>200	N/A	N/A	100	98	*[5]*
NiCoFe LDH	5	1.52	10	0.15	68	84.9	~90	*[6]*
hp-Ni	10	1.423	80	0.043	N/A	~100	98	*[7]*
Ni_3N@C	10	1.38	50	0.14	48.9	98	99	*[8]*
Co-P/CF	50	1.38	20	N/A	N/A	~90	~90	*[9]*
NiOOH	15	1.38	10	0.043	33.5	90	87	*This work*
Ni/C	15	1.39	10	0.32	31.7	-	87	*This work*
NiP@NiC	15	1.37	10	1.82	33.4	91	97	*This work*

References

[1] M.J. Kang, H. Park, J. Jegal, S.Y. Hwang, Y.S. Kang, H.G. Cha, Electrocatalysis of 5-hydroxymethylfurfural at cobalt based spinel catalysts with filamentous nanoarchitecture in alkaline media, Applied Catalysis B: Environmental, 242 (2019) 85-91.

[2] S. Barwe, J. Weidner, S. Cychy, D.M. Morales, S. Dieckhöfer, D. Hiltrop, J. Masa, M. Muhler, W. Schuhmann, Electrocatalytic Oxidation of 5-(Hydroxymethyl)furfural Using High-Surface-Area Nickel Boride, Angewandte Chemie International Edition, 57 (2018) 11460-11464.

[3] W.-J. Liu, L. Dang, Z. Xu, H.-Q. Yu, S. Jin, G.W. Huber, Electrochemical Oxidation of 5-Hydroxymethylfurfural with NiFe Layered Double Hydroxide (LDH) Nanosheet Catalysts, ACS Catalysis, 8 (2018) 5533-5541.

[4] B. You, N. Jiang, X. Liu, Y. Sun, Simultaneous H2 Generation and Biomass Upgrading in Water by an Efficient Noble-Metal-Free Bifunctional Electrocatalyst, Angewandte Chemie International Edition, 55 (2016) 9913-9917.

[5] B. You, X. Liu, N. Jiang, Y. Sun, A General Strategy for Decoupled Hydrogen Production from Water Splitting by Integrating Oxidative Biomass Valorization, Journal of the American Chemical Society, 138 (2016) 13639-13646.

[6] M. Zhang, Y. Liu, B. Liu, Z. Chen, H. Xu, K. Yan, Trimetallic NiCoFe-Layered Double Hydroxides Nanosheets Efficient for Oxygen Evolution and Highly Selective Oxidation of Biomass-Derived 5-Hydroxymethylfurfural, ACS Catalysis, 10 (2020) 5179-5189.

[7] B. You, X. Liu, X. Liu, Y. Sun, Efficient H2 Evolution Coupled with Oxidative Refining of Alcohols via A Hierarchically Porous Nickel Bifunctional Electrocatalyst, ACS Catalysis, 7 (2017) 4564-4570.

[8] N. Zhang, Y. Zou, L. Tao, W. Chen, L. Zhou, Z. Liu, B. Zhou, G. Huang, H. Lin, S. Wang, Electrochemical Oxidation of 5-Hydroxymethylfurfural on Nickel Nitride/Carbon Nanosheets: Reaction Pathway Determined by In Situ Sum Frequency Generation Vibrational Spectroscopy, Angewandte Chemie International Edition, 58 (2019) 15895-15903.

[9] N. Jiang, B. You, R. Boonstra, I.M. Terrero Rodriguez, Y. Sun, Integrating Electrocatalytic 5-Hydroxymethylfurfural Oxidation and Hydrogen Production via Co–P-Derived Electrocatalysts, ACS Energy Letters, 1 (2016) 386-390.